AIMS AND SCOPE

Scientific Mining Journal, which is published in open access electronic environment and in printed, is a periodical scientific journal of Union of Chambers of Turkish Engineers and Architects Chamber of Mining Engineers. The name of the journal was "Mining" until June 2016 and it has been changed to "Scientific Mining Journal" since September 2016 because it can be confused with popular journals with similar names and the ISSN number has been updated from 0024-9416 to 2564-7024.

Scientific Mining Journal, published four times a year (March-June-September-December), aims to disseminate original scientific studies which are conducted according to the scientific norms and publication ethics at national and international scale, to scientists, mining engineers, the public; and thus to share scientific knowledge with society. The journal is in English.

The journal covers theoretical, experimental, and applied research articles, which reflects the findings and results of an original research in the field of mining engineering; review articles, which assess, evaluates, and interprets the findings of a comprehensive review of sufficient number of scientific articles and summarize them at present information and technology level; technical notes, which may be defined as a short article that describes a novel methodology or technique; a case studies, which are based on the theoretical or real professional practice and involves systematic data collection and analysis.

The journal gives priority to works that will enable the advancement of current available information necessary to serve humanity with nonrenewable mineral resources with the perspective of sustainable mining principles. In this context, mine exploration, mineral resource modeling, surveying, mine economics and feasibility, geostatistics, rock mechanics and geotechnics, diggability studies, underground and surface mining, mine design, support design in underground mines and tunnels, rock penetration and rock fragmentation, mine production planning and pit optimization, mine health and safety management, mine ventilation, methane emission and drainage in underground coal mines, mineral processing and beneficiation, process mineralogy, analytical techniques, mineral comminution, mineral classification and separation, flotation/flocculation, solid/liquid separation, physical enrichment methods, hydro and biometallurgy, production metallurgy, modeling and simulation, instrumentation and process control, recycling and waste processing, mining law, environmental health and management, transportation, machinery and equipment selection and planning, coal gasification, marble technology, industrial minerals, space mining, submarine mining and mechanization are included in the journal content.

Submitted manuscripts are evaluated by the editorial board and expert referees independently in accordance with the best practices in academic publishing. The publishing rights of the manuscripts, approved for publication at the end of the evaluation process, are transferred to the Chamber of Mining Engineers by the authors.

Scientific Mining Journal

Publication Ethics

CONTENTS

BİLİMSEL MADENCİLİK DERGİSİ
SCIENTIFIC MINING JOURNAL

TMMOB Maden Mühendisleri Odası Yayını / The Publication of the Chamber of Mining Engineers of Turkey

Original Research

Investigation of Subsidence Induced by the Production of Sublevel Caving Method in Divrigi Ekinbaşı Underground Iron Mine

Bülent Erdem[a,*], Atilla Ceylanoğlu[a,**], Bahadır Şengün[a,***]

[a] Sivas Cumhuriyet Üniversitesi Mühendislik Fakültesi, SİVAS

A B S T R A C T

In this study, the subsidence induced by sublevel caving production method applied in the Divriği Ekinbaşı underground mine was investigated and evaluated. In this context, on-site observations and measurements were made in the underground mine. Two point cloud datasets with an approximately seven-month time difference were analyzed, and surface collapses, cracks, and fractures were plotted on the map for each periods, the fracture initiation and subsidence angles of hangingwall and footwall sides were determined. As a result of the analysis of first and second data sets, subsidence angle of the hangingwall side remained the same as 50.40°, in the footwall side 72.84° and 53.44° respectively. The areas of fracture and subsidence regions increased by 4.67 ha and 7.67 ha, respectively, over a period of around seven months.

Keywords: Sublevel caving method, Subsidence, Fracture initiation and subsidence angles.

Introduction

As is well known, the production methods commonly used in underground mining are classified into three main class as supported, non-supported, and caving methods. Ore geometry and shape (thickness, strike, inclination, depth, etc.), reserve and amount of production, grade and grade distribution, ore-wallrock contact condition, geologic and tectonic structure, strength of ore and wallrocks, groundwater condition, surface and economic conditions are all taken into account during the selection of underground mining method. With the acceptance of the surface subsidence, the caving methods can be selected and applied.

Sublevel caving has been widely used since its introduction in Sweden in the 1960s, particularly in metal mining, due to its advantages such as simple structure, flexibility, and high mechanization (Shuai et al., 2016). In sublevel caving method, the vein is divided into vertical slices that are quite close to each other, typically between 10-30 m (Figure 1). Production is carried out from top to bottom in the ore body, with sublevels prepared at regular intervals. Production galleries that have been driven perpendicular to or parallel to the orebody in the horizontal plane

systematically form sublevel. In thick orebodies, sublevel production galleries are started from the footwall drift and driven up to the hangingwall drift. Sublevel caving is commonly used in deep and steep (>60°) orebodies, but it can also be applied to very thick and massive deposits. The hangingwall can be weak to strong, but it must cave spontaneously or be blasted after the ore is produced. Since there is no filling, the hangingwall must have caved towards the chamber of produced ore. This caving result in serious collapse on the surface and subsidence pits may appear. In this respect, continuous caving is crucial to prevent voids in wallrock, which leads to a sudden collapse that can damage the surface installations.

In this study, the subsidence induced by the production of sublevel caving method in Ekinbaşı underground iron mine was investigated. This underground mine is located within the borders of Divriği district of Sivas province. First, observations and measurements were both performed on the surface and inside the mine, and the results of the study were evaluated in light of the relevant literature.

*bulent@cumhuriyet.edu.tr • https://orcid.org/0000-0002-1226-9248

**aceylan@cumhuriyet.edu.tr • https://orcid.org/0000-0002-1987-6622

***Corresponding author: bsengun@cumhuriyet.edu.tr • https://orcid.org/0000-0003-0413-1748
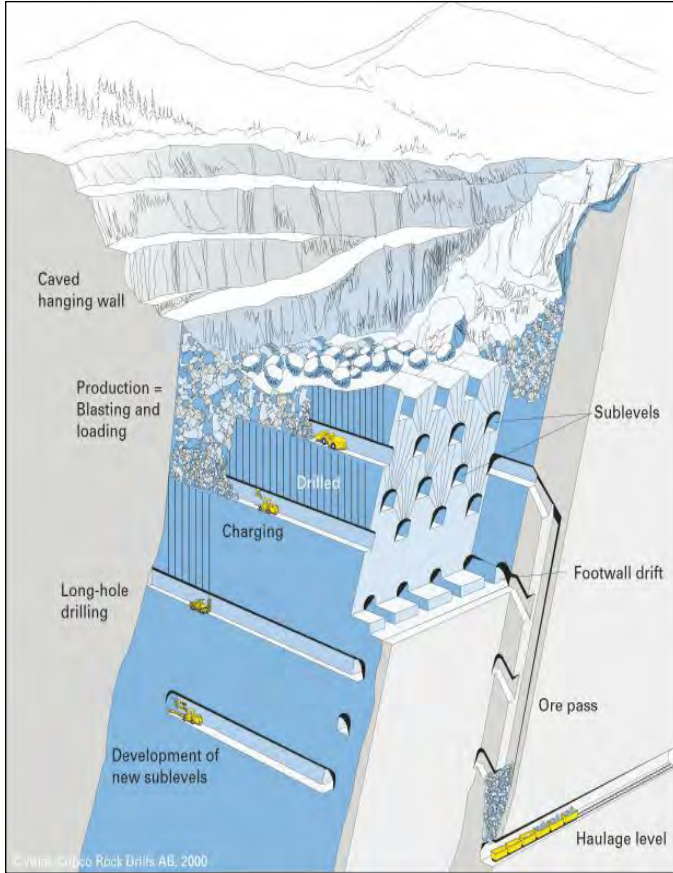
Figure 1. Sublevel caving mining (Hamrin, 2001)

1. Subsidence in sublevel caving method

Surface deformations induced by underground mining have distinct properties that vary depending on the mining method used. During sublevel caving mining, a large-scale subsidence occurs on the surface of the hangingwall side and a smaller subsidence occurs on the footwall side (Herdocia, 1991; Lupo, 1996). The hangingwall subsidence area is divided into three zones: the caved zone, the fracture zone and the continuous deformation zone. (Figure 2). The caved zone is formed by large-scale movement of the wallrock surface layer. The size of the area can range from millimeters to several meters and is typically composed of irregular blocks.

Sometimes natural shafts may also be observed on this area. After ore extraction, these shafts are formed by caved rocks moving downward in the direction of the flow. The fracture zone is defined by stress cracks close to the caved area, fractures, benches and irregularly formed sinks near the caved area. The displacements in this area develop with horizontal and vertical movements ranging from centimeters to meters. Lupo (1996) described the nature of the movement in this zone as a combination of shear and toppling mechanisms similar to those seen in surface rock slopes. The blocks formed in the fracture zone can mix with the rocks in the caved zone. This area is defined as unstable and unsafe for civilian structures. The continuous deformation zone is defined by deformation development ranging from millimeters to centimeters. The surface area of the subsidence zone is usually larger than the extracted area (Blodgett and Kuipers, 2002). The extension of this zone varies depending on the production method and rate, the depth and size of the orebody, the fracture and crack structure of the hangingwall and footwall rocks, their strength, swelling factors, geological discontinuities, surface topography and groundwater level.

Figure 2. Surface deformation zones at mines with sublevel caving mining method (Barba, 2008)

The angle of fracture, which is used to define the boundary of the fracture zone, is mostly determined using the equilibrium limit method. On the other hand, the expansion of the subsidence area is determined by analyzing the recorded data. The equilibrium limit method is based on assumptions similar to those used in rock slope stability analysis. This approach was utilized by Hall and Hult (1964) with the assumption that failure happened along a single plane between extraction and surface (Barba,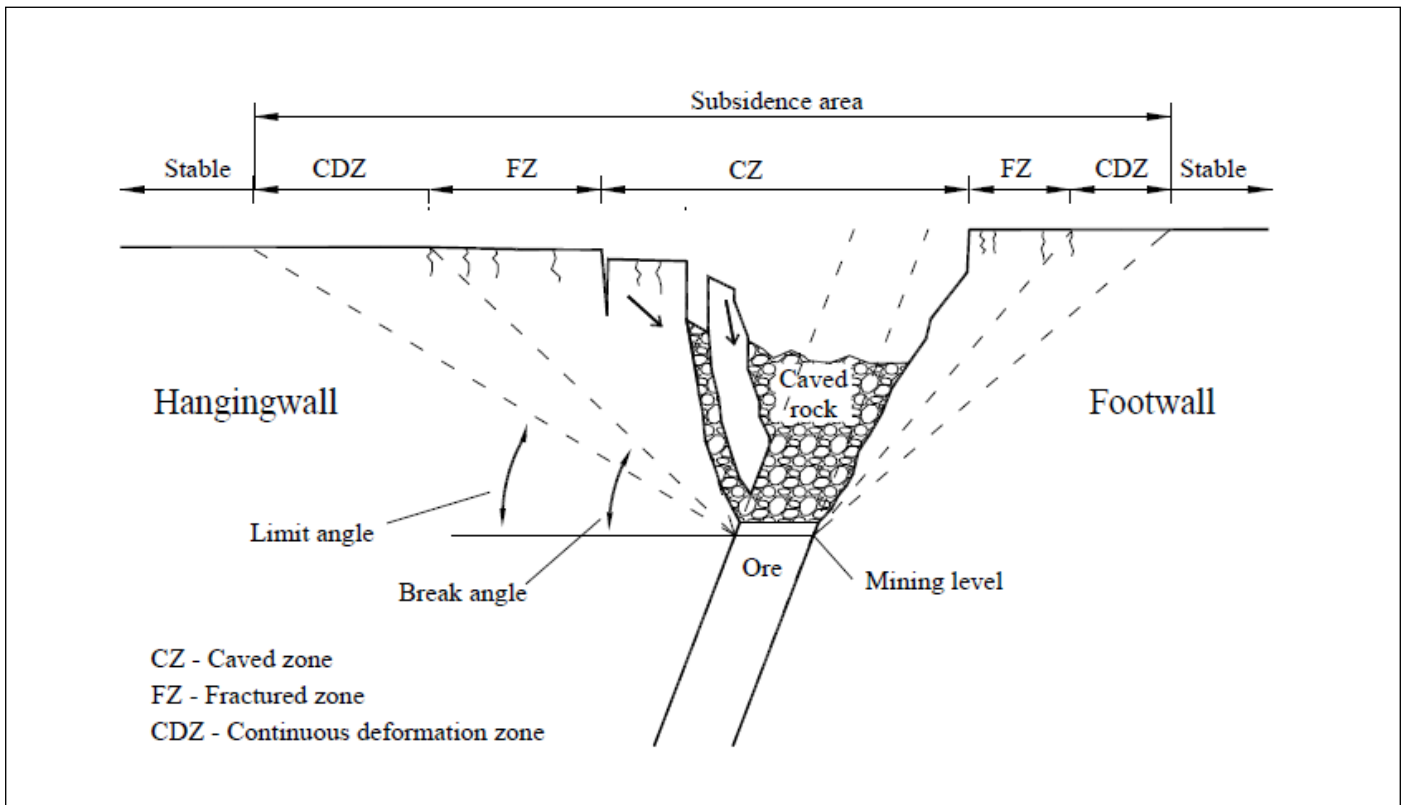 2008). Following this idea, Hoek (1974) developed an equilibrium limit approach to estimate the hangingwall failure for great extraction depths. Hangingwall was supposed to be a rock slope whose base was the bottom of the excavation. As the mining goes downwards, the extraction at the base gradually caves in the hangingwall. It was assumed that there would be a planar shear failure from the extraction bottom to the tension crack on the surface, adding the effect of collapsed rocks. This failure is assumed to occur under static conditions. Sensitivity analyses of the Grängesberg iron mine in Sweden, where the sublevel caving method was used, showed that the fracture angle is highly influenced by the rock mass properties and the depth of mining (Hoek, 1974). Subsidence had occurred in the Swedish-Kiirunavaara underground iron mine due to the using of sublevel caving method, affecting certain areas of Kiruna city, the railway, and the power station. (Villegas et al., 2011). Brown and Ferguson (1979) developed the equilibrium limit method, which takes into account the inclined ground surface and shear plane and the water pressure in the stress crack (Figure 3). Lupo (1996) improved Hoek's equilibrium limit method by accounting the tensile forces occured during ore extraction and the interaction between the hangingwall and the footwall. When the ore is extracted, the caved rocks create tensile forces that will increase the shear stresses on both sides.
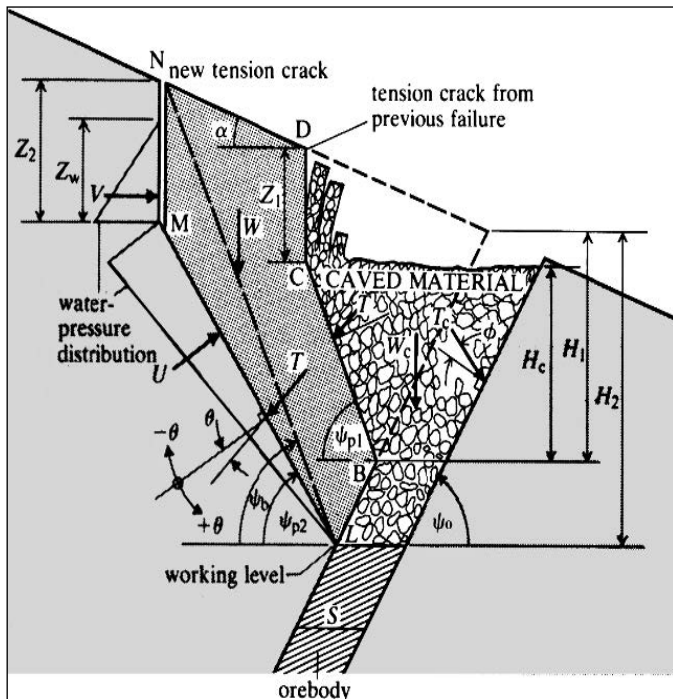

Figure 3. Idealized model used in limit equilibrium analysis of progressive hangingwall caving (Brown and Ferguson, 1979)

1.1. Some underground mines applied sublevel caving method

In the sublevel caving method applied in the Kiruna underground iron mine that is owned by the LKAB in Sweden, the hangingwall is continuously caving while the ore is drawn. This condition results in large-scale subsidence on the surface. The most serious condition in the Kiruna mine is that large-scale collapsing problems have begun on the surface side of the footwall. Ventilation shafts, ore passes, and parts of the haulage level and ramp located near the orebody have been subjected to substantial instability. (Sjoberg, 1996). The Malmberget iron mine, which has rather large orebody and uses the sublevel caving method, is also held by LKAB. Hangingwall collapses caused widespread surface subsidence, similar to the Kiirunavaara mine. Especially, the Kapten section of the orebody has caused extensive subsidence and thus the affected parts of Malmberget city had to be replaced. Kapten part of the orebody had been initially operated as an open pit mine. However, unlike the Kiirunavaara mine, no failures were observed at the footwall side here. (Sjoberg, 1996). Large-scale failures have also happened in other underground mines in Sweden that used sublevel caving, such as the Grängesberg mine. Similarly, an unpreventable large-scale failure occurred on the hangingwall side of the Långsele mine. The underground mine reached and merged with the surface as a result of the failure recorded in the form of crack and significant displacements which developed very quickly (Sjoberg, 1996). Woo et al. (2013) compiled subsidence data for some underground mines applied sublevel caving/shrinkage stoping/top slicing mining methods in the world. (Table 1).

2. Evaluation of subsidence

2.1. Ekinbaşı underground iron mine

Investigations and measurements were conducted on the surface of the Ekinbaşı underground iron mine (Figure 4), as well as in sublevels, footwall drifts and haulage level, as part of this study (Erdem et al., 2019). Sublevels of Ekinbaşı underground iron mine were opened with the advancement of ore connected footwall drifts. The orebody properties taken into account during evaluation of applied mining method are given in Table 2. These galleries with a cross-sectional area of 22.5 m², were opened in the footwall which were parallel to the ore boundary and advanced to the point where the mineralization ends. Then, the galleries with 10 m intervals, in the same size as the footwall drift were continued until the boundary of the ore. Ore boundaries were determined by vertical or inclined drilling to the drift face or side walls and taking into account the traces of ore in the sublevel maps (Ceylanoğlu et al., 2022).

The ore production operations initiated from 1260 level in Ekinbaşı underground mine were advanced down with 12 m level intervals. The produced ore was transported to the ore well, which has a total length of 121 m, and then to the underground crusher, which has a capacity of 700 t/h and is located in the 1108 level. The underground crusher crushed the ore to -170 mm, which was then moved to the conveyor in the main haulage gallery and delivered to the processing plant. Ore production in the Ekinbaşı underground mine was started from 1260 level, it was advanced with a distance of 18 m intervals until the 1170 level, and after this level, it was extended to the 1134 level with 12 m intervals (Figure 5). Thus, 126 m part of ore was produced, from top to bottom.

Table 1. Subsidence data for some underground mines applied sublevel caving/shrinkage stoping/top slicing mining methods (Woo et al., 2013)

Mine	Orebody	Period Reported	Undercut Depth (m)	Caving Angle (°)	Fracture Initiation Angle (°)	Angle of Subsidence (°)	Data Confidence/Comments
Copper Mountain (B.C., Canada)	Contact block	1937-1949	350	79-90	69-74	65	Good (cross-section with scale bar).
	122-East Block	1941-1949	210	82-90	67-74	-	Good (cross-section with scale bar). Lower angle in range aligns with dipping fault.
Copper Queen – Queen Hill (Arizona, USA	Queen Hill Block	1913-1933	100	78	78	78	Marginal (cross-section without scale bar but with mine levels and depths; assumed to be drawn to scale). Caved block is bound on all sides by faults, along which the block drops and across which subsidence is limited.
Kiirunavaara/ Kiruna (Sweden)	700 Level	1965-1995	465	60-94	53-74	40-60	Marginal (subsidence map but without indication of the sublevel depth; sublevel depth estimated from other sources).
Kiirunavaara/ Kiruna (Sweden)	785 Level	1965-2000	500	50-82	50-60	40-50	Marginal. Angles on the footwall side are shown to coincide with one another at 50°.
Gath's (Rhodesia/ Zimbabwe)	99 Level	1971-1976	60	50-75	50-75	-	Good (cross-section with caving angles reported). Lower angles correspond with dip of orebody; steeper angles correspond to caving in dipping hangingwall.
	158 Level		120	50-65	50-65	-	
	183 Level		145	50-56	50-56	-	
Havelock (Swaziland)	Level 1	1952-1972	135	52-82	52-78	-	Good (cross-section with scale bar). Lower angles in range controlled by dip of bedding in footwall. Deformation in hangingwall develops through flexural toppling and shearing along bedding.
	Level 2	1963-1972	180	52-90	52-64	-	
	Level 3	1966-1972	225	52-90	52-60	-	
Miami (Arizona ,USA)	Main orebody	1910-1925	180	60-84	60-68	-	Good (cross-section with scale bar). Mostly mined by top slicing and sublevel caving. Caving limits controlled by vertical boundary drifts. Lower angles are subparallel to foliation of schist.
Mt. Lyell (Tasmania)	Cape Horn (#5 Stope)	1972-1980	160	70-86	70-72	-	Marginal (cross-section without scale bar but with sublevel depths; assumed to be drawn to scale). Lower angles coincide with dip of footwall (70°).
Perseverance (Australia)	10030 Level	1996-1997	490	66-87	63-90	-	Marginal (subsidence map without scale bar; depths determined from secondary information and used to calculate angles; assumed to be drawn to scale). Sublevel caving beneath large open pit. Lower caving and fracture initiation angles extend beyond pit limits on hangingwall side of orebody.
	9920 Level	1997-1998	600	73-81	63-81	-	
	9870 Level	1998-1999	650	74-80	63-80	-	
	9860 Level	1999-2000	660	70-80	62-80	-	
	9850 Level	2000-2001	670	70-83	62-83	-	
	9815 Level	2001-2002	705	73-85	65-85	-	
	9760 Level	2002-2003	760	72-84	66-83	-	
Rajpura Dariba (India)	South 465 Level	-	185	70-90	55-70	-	Poor (no data provided; angles cited in text). 70° angle coincides with dip of footwall.
San Giovanni (Italy)	Contatto Ovest	1985-1990	100	75-92	-	-	Marginal (subsidence map and cross-section without scale bar but with mining levels and depths; assumed to be drawn to scale).

Figure 4. Fractures formed on the surface of Ekinbaşı underground iron mine

Table 2. The parameters taken into account during the evaluation of actively applied mining method (Ceylanoğlu et al., 2022)

| Parameters	Ekinbaşı underground iron mine
Orebody thickness (m)	40-70
Orebody length (m)	410
Depth to orebody top (m)	140
Depth to orebody bottom (m)	300
Dip angle (°)	50-55
Grade (% Fe)	52-56
Type of deposition	Scarn
Contact condition of ore-wallrock	Medium undulation
Strength of orebody	Fair-good
Strength of hangingwall	Poor-fair
Strength of footwall	Poor-fair
Groundwater (L/min)	10
Total proven reserves (tonne)	5 080 000
Production rate (tonne/yr)	600 000
Remaining life of mine (yr)	< 10
Surface conditions for subsidence (Buildings, private property areas, power transmission lines, rivers etc.)	Suitable
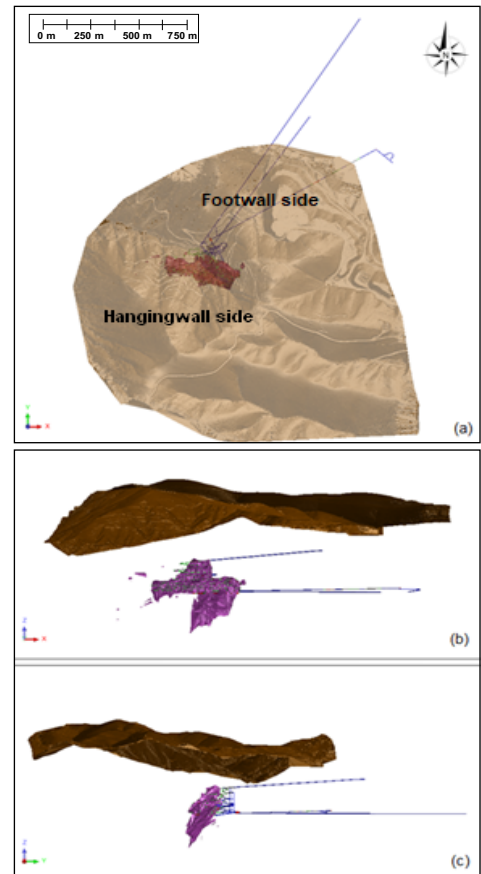
Figure 5. Ekinbaşı orebody, production levels and topography
(a) Plan view, (b) Section view (towards north),
(c) Section view (towards east)

2.2. Evaluation of subsidence

Similar to other underground mines around the world, the rooms created by ore production in Ekinbaşı underground mine were not filled with waste rock or other sorts of materials, but were left to cave. Due to the nature of the method, wall rock strata cave instead of produced ore. The caving of the wall rock strata activates the overburden layers towards the surface, resulting in large-scale surface subsidence.

Production activities in the mine were initiated from a certain roof level and continued towards the lower levels. As production progressed, the gap created by the obtained ore was filled by the immediate roof rock. Since the gap widens as it goes deeper, more wallrock yields and fills the rooms of the produced ore. Since the caving mechanism usually reaches the earth, subsidence, initially shows itself as minor cracks on the surface, later transformed into wide open major cracks, fault type fractures, and ultimately dolin type collapses.

Light detection and ranging (LIDAR) systems are sampling tools that emit numerous pulses in a short amount of time. After collecting each individual reading, the LIDAR system processes them into point cloud data, which includes pulses of light. From another aspect, point clouds are collections of spatial (3D) data points. They can be used to create digital elevation models of ground surfaces in mining. At its most fundamental level, a point data consists of x, y, and z coordinates that represent a specific location on earth. Point clouds can store attribute information about intensity, color, and time. Therefore, they can be used to monitor changes on the ground over time. Two point cloud data sets with high accuracy and resolution that permitted the investigation of the surface topography at the Ekinbaşı mine were taken over a period of almost seven months (203 days). The data was analyzed using a geographic information system software application in accordance with the Cartesian coordinate system, utilizing the ED50 datum and the 6° slice middle meridian. Surface collapses, fractures, and cracks could be detected and plotted on the map due to the high resolution of the data sets (Figure 6 and Figure 7). The collapse zone (CZ), major cracks (FZ), minor cracks (CDZ), and orebody projection (Coordinates to be Y and X; Northwest corner: 418363, 4365506; Northeast corner: 418768, 4365409; Southeast corner: 418715, 4365307 and Southwest corner: 418364, 4365394) were all processed on both figures. In the discontinuous deformation zone, there are large-scale collapse zones corresponding to the mine's projection on the surface. In proportion to the projection of the ore on the surface, wide-opening fracture cracks develop in common centered and ellipted. These are surrounded by narrow-opening deformation cracks. It was seen that in the period of approximately seven months between the dates of the first and second point cloud data, the effects of subsidence intensified, the collapse zone began to mature and the major fracture area and the minor crack area spread.

The Surpac mine planning package (https://www.3ds.com/products-services/geovia/products/surpac/) was used to determine the angles that characterize the subsidence occured on the surface of the Ekinbaşı underground mine (Table 3). The angles of fracture initiation and subsidence can be regarded to be consistent with the literature. The angles, on the other hand, decreased from the first to the second measure (203 days), and the cone base expanded. As the collapse zone expands in the following periods, the fractures around it will widen and turn into benches.

They will also be able to develop both downwards and towards the collapse zone that serves as the subsidence's center. On the other hand, since the continuous deformation zone is likely to spread further, this region, which limits the subsidence effect, should be monitored with displacement measurements that are repeated at regular intervals taking seasonal conditions into account. The subsidence basin generated on the surface is still in the maturation phase due to the activities carried out in the Ekinbaşı underground mine.

In a period of about seven months, the areas of fracture and subsidence regions increased by 4.67 ha and 7.67 ha, respectively. The development of these areas should be monitored at regular intervals using surface and/or air equipment capable of providing high-accuracy coordinate data via measurement stations placed in certain characteristic points on the surface, and surface motion vectors should be revealed. Thus, detailed information can be obtained about the development of the subsidence basin and will be able to make future predictions.

Sjoberg (1996) stated that the effects of subsidence were seen on the surface of the footwall side of the Kiruna underground mine, which operates in Sweden and produces approximately 27 million tonnes per year, and the most serious situation in the Kiruna mine was the larger - scale instability problems in the mine's footwall. Due to the fact that ventilation wells, ore passes, and some parts of the main entrance ramp were located so close to the orebody, they had subjected to significant instability (Sjoberg, 1996).

All developments, including transportation and ventilation wells, spiral ramp, and access galleries, are made on the footwall side of the steeply dipping ore body, while the hangingwall side is left to cave, according to the sublevel caving method used in the Ekinbaşı underground iron mine. Thus, the surface subsidence begins on the hangingwall side, and the fracture starting and subsidence angles on this side are characterized by lower angles corresponding to a wider area. This can be seen from Table 3 for the Ekinbaşı mine. During the field studies, access galleries and spiral ramp were investigated and there was no deformation in the well-gallery system due to subsidence. As production continues deeper, similar effects may occur on the footwall side. Hence, transport and ventilation wells, spiral ramp, and galleries should be monitored for these effects.

Table 3. Fracture initiation and subsidence angles at hangingwall and footwall sides of Ekinbaşı underground iron mine

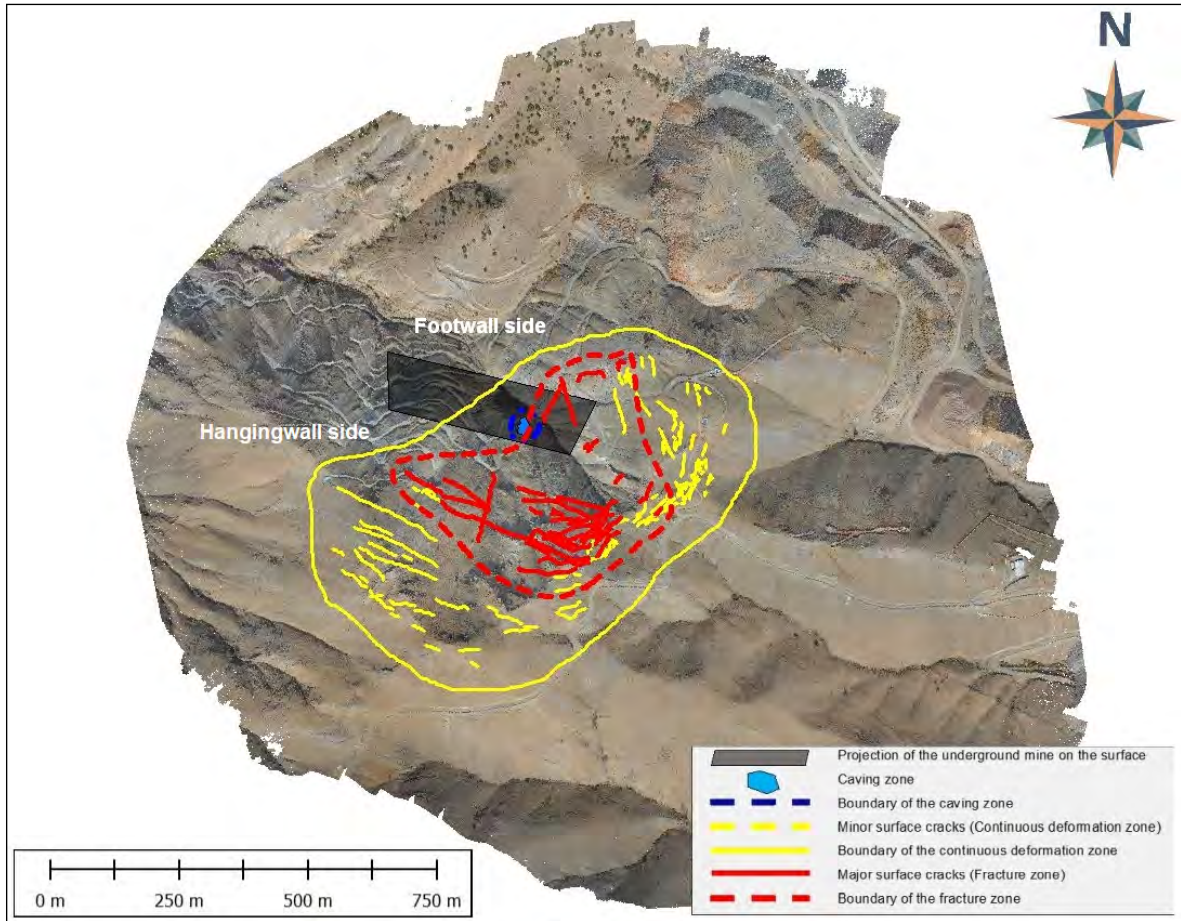| Region	First measurement		Second measurement	
	Fracture initiation angle (°)	Subsidence angle (°)	Fracture initiation angle (°)	Subsidence angle (°)
Hangingwall side	61.45	50.40	54.57	50.40
Footwall side	73.65	72.84	62.65	53.44
Fractured zone area (ha)	14.28		18.95	
Subsidence area (ha)	39.50		47.14	

Figure 6. Fractures formed on the surface of Ekinbaşı iron mine (Using cloud data of first point)
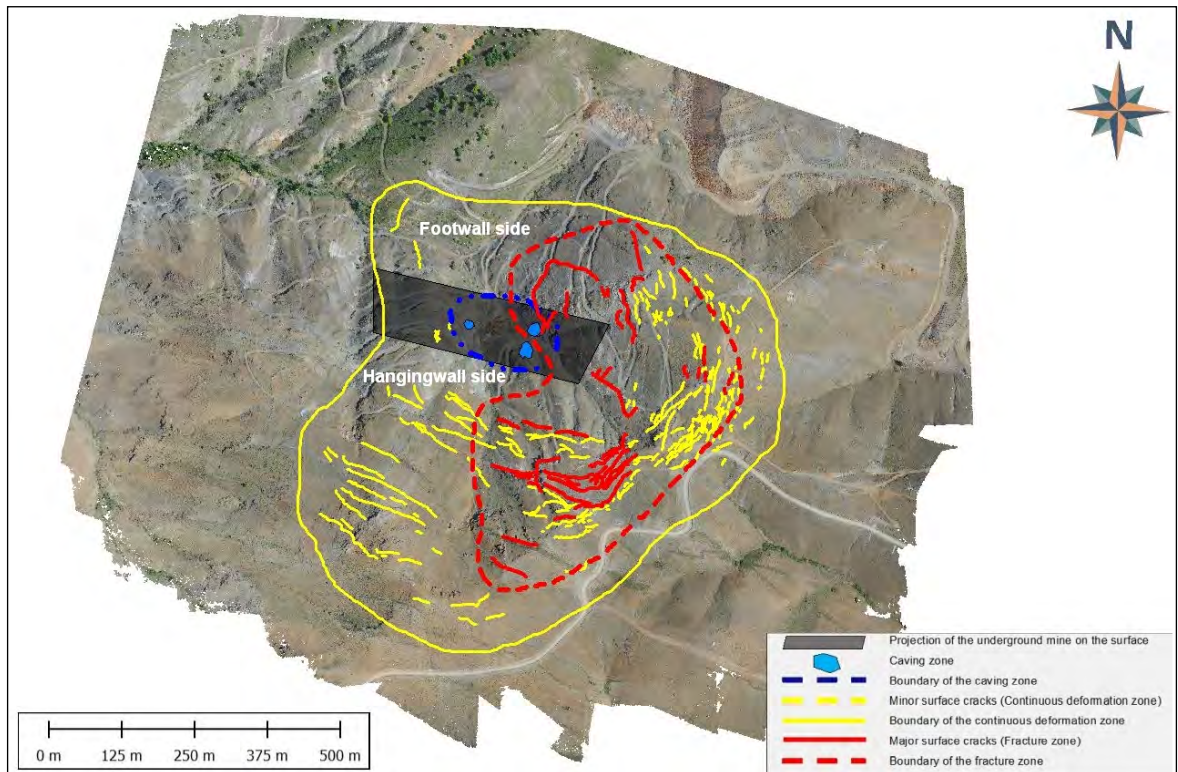

Figure 7. Fractures formed on the surface of Ekinbaşı iron mine (Using cloud data of second point)

3. Conclusions

In this study, the subsidence occured due to the sublevel caving mining method used in Ekinbaşı underground iron mine was investigated and evaluated. In accordance with the sublevel caving production method, since the rooms of produced ore were not filled with waste rock or other types of materials, but were left to cave. Due to the nature of the method, upper rock layers cave instead of the produced ore. The caving of the wall rock layers activates the upper layers towards the surface, causing a large-scale surface subsidence.

For Ekinbaşı underground mine, two point cloud datasets with a time difference of about seven months (203 days) were evaluated, and surface collapses, cracks, and fractures were shown on the map. By using the Surpac mine planning package, the fracture initiation and subsidence angles of hangingwall and footwall sides that characterize the subsidence occured on the surface of the Ekinbaşı underground mine were determined for each periods. The fracture initiation and subsidence angles of hangingwall side were determined as 61.45° and 50.40° and footwall side's were 73.65° and 72.84°, respectively for the first data set. For the second data set, the subsidence angle of the hangingwall side remained the same as 50.40°, where the fracture initiation angle was 54.57°. Therefore, in a period of about seven months, the areas of fracture and subsidence regions increased by 4.67 ha and 7.67 ha, respectively.

Due to the activities carried out in the Ekinbaşı underground mine, the subsidence basin occurred on the surface is still in the maturation period. To make future predictions about the subsidence basin, development of this area should be monitored at regular intervals.

References

Barba, T.F.V. (2008) Numerical analyses of the hangingwall at the Kiirunavaara mine, Licentiate Thesis, Luleå University of Technology, Department of Civil and Environmental Engineering, Division of Rock Mechanics, Luleå, Sweden.

Blodgett, S., Kuipers, J.R. (2002) Underground Hard Rock Mining: Subsidence and Hydrologic Environmental Impacts, Technical Report, 50s.

Brown, E.T., Ferguson, G.A. (1979) Progressive hangingwall caving at Gath's mine, Rhodesia, Trans Inst Min. Metall, 88, A92-A105.

Ceylanoğlu, A., Erdem, B, Şengün, B., Karatepe, A. ve Yayla, M.E. (2022). Evaluation of actively applied mining method and ore loss in Divriği A-Kafa and Ekinbaşı underground iron mines, Scientific Mining Journal, 61 (4), 213-220.

Erdem, B., Ceylanoğlu, A., Doğan, T., Şengün, B. (2019). Evaluation of the affected surface area and the environmental effects of the subsidence caused by the applied mining method in Divriği Ekinbaşı Underground Iron Mine. Sivas Cumhuriyet University Mining Engineering Department, Sivas, 34 p. (in Turkish, unpublished).

Hamrin, H., 2001. Underground mining methods and applications. Underground mining methods: Engineering fundamentals and international case histories, eds. W.A. Hustrulid and R.L. Bullock, SME, Littleton, Colorado, pp 3-14.

Herdocia, A. (1991) Hanging wall stability of sublevel caving mines in Sweden, PhD Thesis, Luleå University of Technology, Luleå, Sweden.

Hoek, E. (1974) Rock slope engineering, Institution of Mining and Metallurgy, London, ISBN 10: 0900488212.

Lupo, J.F. (1996) Evaluation of deformations resulting from mass mining of an inclined orebody, PhD Thesis, Colorado School of Mines, Denver, ABD.

Shuai, C., Weidong, S., Dan, D., Yuankun, L., Jianqiang, L. (2016). Numerical simulation of land subsidence and verification of its character for an iron mine using sublevel caving, International Journal of Mining Science and Technology, 26, 327-332.

Sjoberg J. (1996) Large Scale Slope Stability in Open Pit Mining – A Review. Technical Report, Division of Rock Mechanics, Luleå University of Technology, Sweden, 215 s.

Web:https://www.3ds.com/products-services/geovia/products/surpac/, Access date: June, 2019.

Woo, K-S., Eberhardt, E., Elmo, D., Stead, D. (2013). Empirical investigation and characterization of surface subsidence related to block cave mining, International Journal of Rock Mechanics & Mining Sciences, 61, 31-42.

Villegas, T., Nordlund, E., Dahnér-Lindqvist, C. (2011). Hangingwall surface subsidence at the Kiirunavaara Mine, Sweden, Engineering Geology, 121, 18-27.

Research Article

Intelligent Supervision System of Ore Pass Using Improved YOLO v3

Baoshun Liu[a, *], Yanyu Song[b], Yongjing Ye[a], Zijing Zhang[a]

[a] School of Civil and Resource Engineering, University of Science and Technology Beijing, Beijing, 100083, China
[b] China ENFI Engineering Corporation Changsha Branch, China

A B S T R A C T

To prevent safety accidents caused by equipment and personnel entering the ore pass by mistake, it is necessary to arrange ore pass control personnel underground the mine. The control personnel in the ore pass are extremely vulnerable to dust and noise during the unloading process of mining vehicles, and there is an urgent need for an intelligent access control system to reduce safety accidents. This article establishes a training set for object detection of the YOLO v3 model based on images of mining vehicles in underground monitoring videos. Through optimizing the training process and algorithm of the YOLO v3 model, and adopting a dual camera collaborative discrimination method, the influence of brightness on the recognition results when mining vehicles are turned on is overcome. In this way, the mining vehicles entering and exiting the pass operation area are accurately identified from the underground monitoring videos. Then, an intelligent access control system for controlling the orepass door is developed based on the Jetson Nano embedded program. The research results show that the average accuracy of the system in identifying target vehicles is greater than 95%. It can rotate the ore pass door by 90 ° in 3 seconds, achieving intelligent control of the mine orepass and promoting the construction of smart mines.

Keywords: Yolov3, ore pass, smart access control, object detection, recognition of underground mine vehicle.

Introduction

As a key link in the development and production transportation of mineral resources, mine pass transportation and its system cannot only save transportation equipment, but also improve the convenience of mine production management. However, the transportation of mine passes faces problems such as low underground visibility and multiple blind spots, which can lead to accidents caused by collisions between mobile equipment and personnel. Among them, substations, ore passes, and explosive magazines are areas that require risk control (Imam et al., 2023). To reduce safety risks, some mines have designated personnel on duty in the above-mentioned areas. Although this method is simple and feasible, with the extension of underground tunnels and the widespread application of large-scale mechanized equipment in the underground, the areas that need to be monitored are also constantly expanding. If we continue to use this method, it will significantly increase labor costs but also not comply with the concept of green and intelligent mining construction. On the other hand, the narrow underground space, dust, and noise can also harm the health of personnel on duty (Madahana et al., 2020).

Faced with this issue, Guo and Li (2011) used positioning technologies such as RFID, GIS, and ZigBee wireless communication to control the movement of underground personnel in designated areas, which effectively reduced the safety and health risks of underground personnel. Yang et al. (2016) established the Gaussian Mixture Model (GMM) and combined it with surveillance videos to identify underground personnel, providing an early warning mechanism for the safety of underground personnel. They have made beneficial explorations to protect the safety of underground personnel on duty. However, to fundamentally solve the safety problem of mine pass transportation, it is necessary to continue to conduct in-depth research towards unmanned and intelligent directions.

In recent years, the continuous development and maturity of artificial intelligence have injected new vitality into the development of various industries. Object detection is the localization and classification of a variable number of targets in an image, ultimately obtaining the categories and positions of multiple targets in the image. It is one of the important branches in computer image vision. Target detection algorithms can be divided into selec-

tion-based algorithm models such as R-CNN (Girshick et al., 2014), fast R-CNN (Ren et al., 2017), and regression-based algorithm models such as SSD (Liu et al., 2016) and YOLO (Redmon and Farhadi, 2016).The object detection model represented by YOLO (You Only Look Once) has been widely applied in facial recognition, autonomous driving, agricultural production, and medical image analysis. After Yolov1 was first proposed by Redmon and Farhadi (2016), Kumar et al. (2022) proposed ETL-YOLO v4 model, which added Mosaic and CutMix data enhancement functions during training, significantly improving the recognition accuracy of face wearing masks during the COVID-19 period. Kang et al. (2024) developed a YOLO-FA model for vehicle detection in autonomous driving using the A type-1 fuzzy attention (T1FA) mechanism, which effectively improved the accuracy of vehicle detection in rainy and nighttime scenarios with high uncertainty. Tian et al. (2023) proposed an MD-YOLO model for detecting small target pests and successfully deployed it in pest warning software, promoting the improvement of pest warning mechanisms in agricultural production. Baccouche et al. (2022) combined the deep learning model with YOLO algorithm for early mammograms diagnosis, which significantly improved the diagnostic accuracy of early breast cancer. The above researches prove the excellent performance of image detection algorithms represented by YOLO and can effectively solve relevant practical problems, which also provides the possibility for their application in mine pass transportation.

In the current underground location positioning system of mines, intelligent access control systems are used for controlling risk areas. The system can automatically identify the moving targets entering the risk area in real-time. Once unauthorized personnel or equipment enter, the system will automatically control the access control switch to ensure strict control of high-risk areas. This system cannot only meet the basic requirements of entry and exit management, but also integrates functions such as early warning and alarm, which can be used to timely remind operators or management personnel to pay attention to potential risks and take necessary response measures. In addition, the data statistics and analysis function in the system can provide rich and detailed operation data for management personnel, which is helpful for optimizing mining production strategies and decision-making. However, the underground lighting in mines is dim and the dust concentration is high. If the images collected in the mine are directly used for object detection without preprocessing, there is a problem of low image recognition rate. Inefficient image recognition may not only miss out on real risk events, but may also generate false alarms, affecting the normal operation of mining production.

This article proposes a network training method and algorithm for improving the benchmark YOLO v3 model to address the aforementioned issues in the identification of underground mining cars. By using a dual camera collaborative discrimination method, the mining cars in the pass operation area are identified and the pass door is automatically controlled to improve the safety of the pass operation, providing a new tool for the stable, efficient, and safe operation of the mine pass transportation system.

1. Current situation and existing problems in the control of mine pass

The second mining area is the largest under a certain group, and the development method of the mining area is vertical shaft inclined slope level roadway. The diameter of the ore pass in the mining area is generally 4m, with a depth of 100m-150m.There have been many accidents of construction personnel and equipment falling into the ore pass. The mining area adopts methods such as ore pass doors, covers or special personnel to ensure the safety of personnel and equipment in the operation area. The ore pass doors are generally closed (Fig.1), and that used frequently are manned. When the loader unloads ore (waste rock) in and out

of the ore pass, the watchman opens or closes the door. Some less commonly used ore passes require the scraper driver to open or close the door. The cover is opened (Fig.2) or closed (Fig.3) by the hoist using an electric remote control by the watchman or the loader driver.

The shortcomings of the above-mentioned manual control method are: (1) The dust concentration is large during unloading ore or rock, which damages the health of the personnel on duty; (2) It is inconvenient to count personnel and vehicles, and it is easy to have regulatory errors and omissions, and difficult to trace the whole process of the accident once an accident occurs. Considering the underground working environment, the Yolov3 algorithm with fast monitoring speed, low background false detection rate and strong versatility is selected. Computer vision technology is used to automatically identify underground mine vehicle entering and exiting the ore pass. An intelligent ore pass access control system composed of Jetson Nano embedded platform, automatic door opener, and electromagnetic lock is built.

Fig.1 Ore pass door in the mining area

Fig.2 Opened ore pass cover

Fig.3 Closed ore pass cover

2. Technical plan for underground ore pass door

2.1 The principle of YOLO v3

YOLO v3 is the third version of the YOLO model, proposed by Redmon and Farhadi in 2018. It uses Darknet-53 as its backbone network, while using Batch Normalization to accelerate training speed, and increase residual connections to solve gradient vanishing. It also uses cross entropy loss function and dynamic weight decay algorithm to optimize the training effect of the neural network. Compared with YOLO v1 and YOLO v2, YOLO v3 achieves higher detection accuracy while maintaining speed. YOLO v3 uses 9 predefined anchor boxes, divided into 3 groups of 3 in each group. Each group of anchor boxes corresponds to a feature map of a scale to adapt to targets of different sizes, which significantly improves the detection ability for small objects. In previous versions of YOLO, each object could only be assigned to one category, while YOLO v3 allowed an object to have multiple categories simultaneously, achieving multi-label classification. In addition, the loss function of YOLO v3 comprehensively considers the errors of coordinate prediction, target confidence, and category prediction, further improving its detection accuracy.

YOLO v3 not only inherits the real-time and efficient performance of YOLO series models, but also further optimizes accuracy and stability. Through deep network structure, three scale detection, and new technological improvements, YOLO v3 has been widely applied and recognized in object detection.

2.2 Modeling process

2.2.1 Building a dataset for underground mining vehicles

Local features such as license plates and global features such as the outline and color of the vehicle can be used for visual recognition of mining vehicles. The license plates of underground mining vehicles are easily affected by factors such as oil pollution, dust, and sudden changes in light, resulting in the inability to accurately extract license plate information, thereby affecting the recognition effect. Due to the current lack of underground mine vehicle datasets, it is necessary to construct the datasets of four underground mine vehicles, including scraper, 20t tunnel transport vehicle, 25t A-type mine vehicle, and 25t B-type mine vehicle. The video of the underground network surveillance camera in the second mining area is collected. The images of four types of trucks under different lighting environments, different shooting conditions and different driving speeds are obtained by framing after the video is edited. After data enhancement such as rotation, cropping, brightness adjustment, and distortion of these images, 2224 photos of each of the four types of underground mine vehicle are obtained. Then the LabelImg software is used to manually label the underground mine vehicle features on each vehicle's image to generate a underground mine vehicle dataset. To facilitate the model training and the judgment logic of opening and closing doors, each type of underground mine vehicle is subdivided into eight categories according to the method marked in Table 1.The label information includes the vehicle class name and coordinates in the image, and stores it in the format of a standard VOC dataset. Figure 4 is the underground mine vehicle dataset after completing the front label of the vehicle.
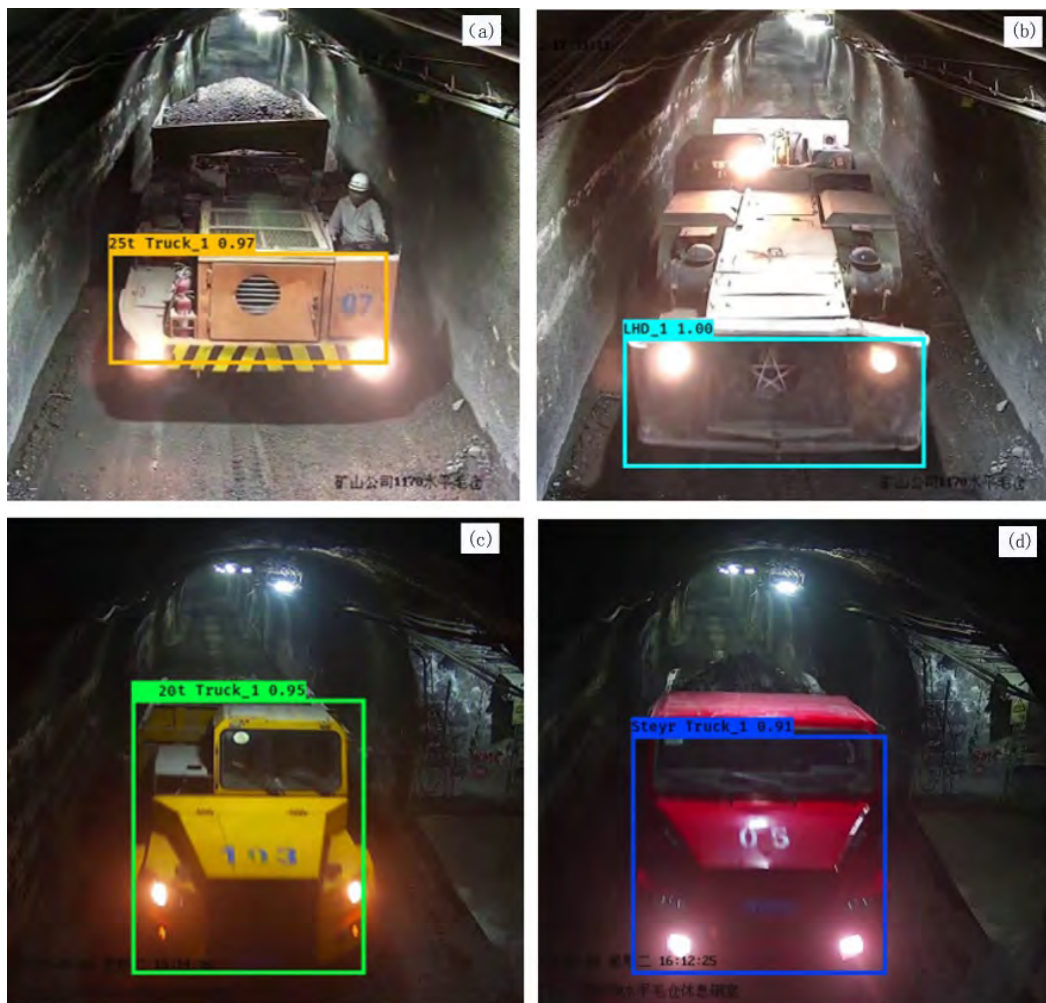

Fig.4 Underground mine vehicles dataset after labeling

Table 1. Underground mine vehicle labeled in the dataset

Vehicle category	Detection classification	Label name
Loader	Head	LHD_1
	Trail	LHD_2
20t tunnel transport vehicles	Head	20t Truck_1
	Trail	20t Truck_2
25t A-type minevehicle	Head	25t Truck_1
	Trail	25t Truck_2
25t B-type minevehicle	Head	Steyr Truck_1
	Trail	Steyr Truck_2

2.2.2 Improved benchmark Yolov3 algorithm and training strategy

The detection effect of using the benchmark Yolov3 algorithm model to construct an intelligent unmanned control system for the ore pass does not meet expectations. Occasionally, underground mining vehicles may not be recognized or classified incorrectly, mainly due to the following reasons:

(1) The image data of the underground vehicle dataset constructed in the second mining area is insufficient. It is relatively cumbersome to screen out vehicle videos in a large number of video data. The images of underground mine vehicle are mainly taken from the webcam video of the 1170 Maocang rest chamber and the Maocang ore pass. The collected underground mine vehicle images are relatively limited, which reduces the generalization of underground mine vehicle features, thereby affecting the effect of target recognition.

(2) The benchmark Yolov3 algorithm is difficult to adapt to the complex underground operating environment. The recognition effect of underground mining vehicles is optimal when driving smoothly and parking. However, when the vehicle is close to a certain range of the underground surveillance camera, due to the weak underground light, the program is easy to fail to obtain the underground mine vehicle or the underground mine vehicle is blurred under the strong light of the headlights, thus affecting the detection accuracy of vehicle identification.

To build an efficient and reliable intelligent unmanned control system for ore pass, it is necessary to improve the training strategy and optimize the algorithm of the model to better adapt to the underground environment according to the above problems.

1) Spatial pyramid pooling structure

Convolutional neural network is mainly composed of convolutional layer and fully connected layer, where the parameters of the fully connected layer are related to the input size. Only using a fixed input size can the fully connected layer parameters in the training be determined. Therefore, the Spatial Pyramid Pool (SPP) structure is proposed. Any scale feature input into the structure, after its pooling kernel processing, can output features of the same scale, thus achieving mutual fusion of features of different scales. This article inserts an SPP module into the Convolutional Set of the Yolov3 algorithm model, and the modified Convolutional Set module is shown in Fig. 5.The SPP module consists of four parallel branches, except for the first branch that outputs the results directly from the convolutional set: the second branch is the maximum pooling of 5×5 pooling kernels; the third branch is the maximum pooling of pooling kernels of 9×9, and the fourth branch is the maximum pooling of pooling kernels of 13×13.That is, after the SPP module processing, the original input channel will be ex-

panded by 4 times. For example, the input of the convolution set in the SPP module is 16×16×512, and after Concatenate fuses the channels, the output is expanded to 16×16×2048.
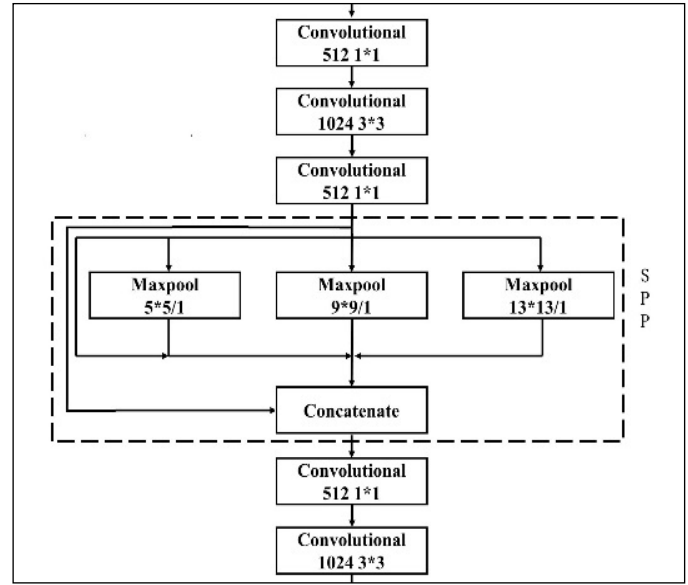

Fig. 5 Insert the SPP module in Yolov3

2) Use K-means++ clustering

Yolov3 uses the K-means clustering algorithm to calculate the anchor box. The anchor box is obtained by cluster regression based on the size data of the detection target during training using the following steps:

① The algorithm model randomly selects several points in the dataset as the cluster center.

② The Euclidean distance formula (1) is used to calculate the distance from all data points to the coordinates of each cluster center separately. Then regression calculations are performed based on the calculated distance, and the data point categories are divided by the number of cluster centers.

$$d(x,y) = \sqrt{\left(x_1 - y_1\right)^2 + \left(x_2 - y_2\right)^2 + ... + \left(x_n - y_n\right)^2} = \sqrt{\sum_{i=1}^{n}\left(x_i - y_i\right)^2} \quad (1)$$

③ The distance from the clustered data point to the center of each cluster is recalculated. The mean of the data is then calculated, and the cluster centers of each class are re-divided according to this mean.

④Repeat steps ②and ③until the resulting central positions of each type of cluster remain constant or the sum of squared errors is minimized.

It can be seen from the K-means clustering algorithm that the core of the algorithm is to select the initial clustering center. When the cluster center selection is not suitable (such as the distribution of each cluster center point is concentrated), the continuously calculated results may cause the algorithm model to fall into the local optimum, so that the expected clustering results cannot be obtained. To avoid this situation, the K-means++ algorithm is used to optimize all cluster centers randomly selected at one time in K-means, and the steps are as follows:

① A random point is selected in the dataset and set as the initial cluster center point.

② The shortest distance of each data point from the coordinates of the above cluster center point is calculated, and the calculation results are stored in an array. That is, the array represents the shortest distance from each data point to the center of all clusters.

③ All the elements in the above array are added to obtain a distance sum. Randomly taking a value within the total distance range to iterate through all elements in the array, a cluster center point is obtained by calculation.

④ The shortest distance between each data point and the coordinates of the two cluster center points is calculated, and the smallest one is selected and stored in the array.

⑤ Repeat steps ② and ③ to calculate the desired cluster center point.

⑥ The cluster center point obtained above is used to replace the initial cluster center randomly selected by the K-means clustering algorithm to perform cluster calculation and reduce the influence of the initial point on the algorithm. At the same time, a new distance formula (2) is defined to replace the original Euclidean distance calculation formula. The distance () calculated using this formula is inversely proportional to the interaction ratio. The larger the image interaction ratio (IOU), and the smaller the distance, which is more likely to be classified into the same category.

$$d(box, centroid) = 1 - IOU(box, centroid) \qquad (2)$$

3) UsingMosaic data augmentation

Mosaic data augmentation is a method to enhance the breadth of deep learning data and improve the stability of models. It allows the model to learn to use an unlimited amount of data without introducing new real data. At the same time, the markup of the dataset and the comprehensibility of semantic information are increased, which can improve the generalization ability of the model. The Mosaic data enhancement method is to merge multiple different types of images, randomly select one of the images as the main reference, and then randomly stitch the remaining images near the main image after image transformation operations such as cropping, rotating, and brightness adjustment to form a larger Mosaic image.

4) Activation function

The activation function used by Yolov3 is Leaky ReLU, as shown in Eq.3.

$$Leaky \, ReLU(x) = \begin{cases} x & x > 0 \\ \alpha x & x \le 0 \end{cases} \qquad (3)$$

To further expand the scope of functions, accelerate the training speed of the algorithm and enhance the robustness of the model, this paper uses the Mish activation function (Equation 4) to replace the Leaky ReLU function.

$$Mish(x) = x \tanh(ln(1+e^x)) \qquad (4)$$

The Mish function maintains better network gradients than the Leaky ReLU function. The Mish curve is smooth, and its training results have optimal generalization, and are easy to update a large number of neurons during training. Although the Mish func-

tion is more complex and will occupy more computing resources, it will obtain better calculation results. The mean Average Precision (mAP) of the ReLU activation function and the Mish activation function are 91.62% and 92.83%, respectively. It can be seen that the Mish activation function has stronger performance, with an improvement of approximately 1.3%.

5) Training and optimization of models

Three sets of models: Yolov3-416, Yolov3-tiny-416, and improved Yolov3-416, are compared. Yolov3-tiny is a streamlined version of Yolov3, which is more lightweight and has lower requirements for graphics and memory, making it easier to apply in embedded systems. Its fast detection speed makes it easier to achieve real-time detection. However, Yolov3-tiny is essentially based on Yolov3, which removes one-third of the non-redundant intermediate layers through pruning compression, which can easily cause missed and false positives. Therefore, Yolov3 has an advantage in accuracy. The value 416 after the three sets of model names represents the image input_shape. The Yolov3 algorithm can uniformly transform the size of the original image into an input_shape that can be set independently, and then send the image to the training network after the unified size. Setting different input sizes can obtain model weight files with different detection effects. Generally, the larger the input size, the higher the accuracy, but the higher the requirements for memory and other aspects. The commonly used input size is 416×416.

During the training process, the dataset is distributed according to train set: test set: validation set (val) = 6:2:2. The weight model is set to be saved every 3 iterations, and the validation set loss value of each iteration val_loss is recorded. When there is a failure of 10 consecutive iterations to be less than the minimum value of the recorded val_loss, stop training, and the val_loss minimal weight model is resumed as the final training output model. The image dataset, model parameter settings, and training environment are the same when the three algorithm models are trained. The loss rates of the three model algorithms are shown in Fig. 6, and the number of network layers and mAP are shown in Table 2.
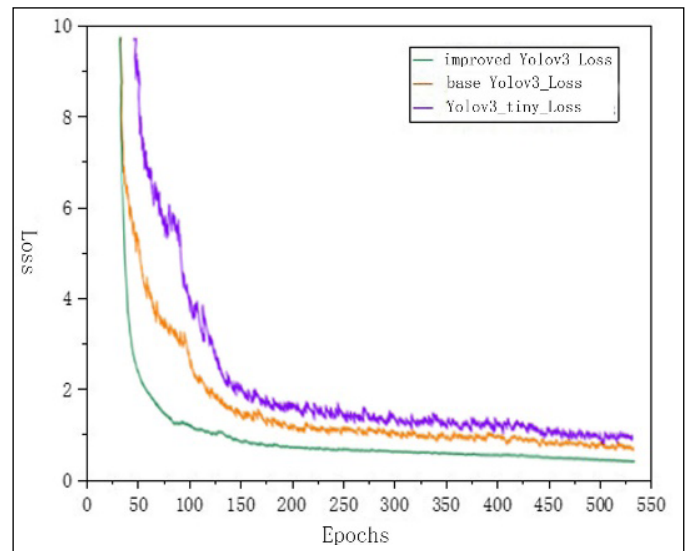

Fig. 6 Loss value change curve of the training process of the three algorithm models

Table 2. Network result parameters and test results of different algorithm models

Algorithmic models	The number of network layers	mAP/%	F1-Score/%	Time/ms
Yolov3-416	106	92.59	93	28.55
Yolov3-tiny-416	23	89.49	90	3.26
Improved Yolov3-416	80	98.88	98	24.27

It can be seen that compared with the benchmark Yolov3, Yolov3-tiny has fewer network layers and the lowest model complexity. It can significantly reduce the detection time, with an average accuracy reduction of 3.1%, and a reduction of 3% in F1 score. According to the training results of benchmark Yolov3, the improved Yolov3 model converges faster and is relatively more stable. After completing 500 iterations, the loss function tends to smooth. The average accuracy and detection time have been improved while the number of network layers has decreased. It can be seen that among the three Yolov3 models, the improved Yolov3 algorithm model can better adapt to the underground operation environment of the second mining area.

3. Design and implementation of intelligent ore pass access control

Considering the practical application conditions in underground mines, an intelligent ore pass access control system based on Jetson Nano embedded development (Fig.7) is designed. The hardware platform of this system mainly consists of three parts: vehicle video capture, Jetson Nano central processing unit, and access control system.
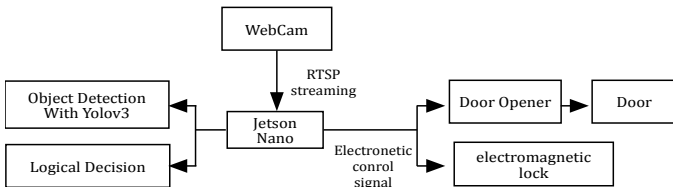

Fig.7 Intelligent ore pass access control system

3.1 Central processing unit

Due to the special underground environment, the use of embedded development platform as the central processing unit of the access control system cannot only meet the integration of software and hardware, achieve the effect of image recognition without networking, but also have the advantages of small size and high stability. It is easy to install near the door, and the system uses Jetson Nano (Fig.8) as the embedded processor.

3.2 Video capture

The Hikvision all-in-one network cable is connected to the corresponding interface of Jetson Nano, and the IP address, subnet mask and gateway where the camera is located are configured. When the vehicle enters the camera's field of view, OpenCV programming is used to read Hikvision's standard RTSP push format to obtain surveillance images.

3. 3 Access control system

Access control systems include automatic door opener, electromagnetic lock and door. The automatic door opener uses the motor to drive the door to rotate, and the opener controls the motor forward or reverse according to the signal sent by the pro-

cessor to realize the automatic opening and closing of the door. The body of the selected brushless floor opener (as shown in Fig. 9) has two 400mm long swing arms that can drive a door up to 150kg. The control logic of the automatic opener is to short-circuit the GND and N1 interfaces in the motherboard to open the door, and short-connect the GND to N2 to close the door. The GPIO pin of the Jetson Nano can output high and low levels according to the Yolov3 image recognition results. This signal is passed to the relay shown in Fig. 10 that can be triggered by high and low levels as a switch controlled by an automatic gate signal. The relay controls the status of the electromagnet through electrical signals, which in turn controls the switching at the output. To correctly judge the opening and closing state of the door, the opener needs to be equipped with an electromagnetic lock to receive the electronic control signal of the opening and closing door transmitted by the opener, so as to control whether the electromagnetic lock is energized. The electromagnetic lock selected is a 12V-180kg tensile magnetic lock shown in Fig.11, which has a normally open and closed signal feedback function and can be connected to the main control board of the access control system. According to the net section of the roadway, the guardrail net with an external dimension of 4.5m ×4.8m is selected as the door.
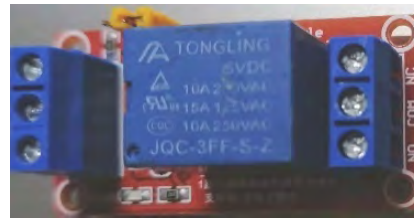

Fig.8 Jetson Nano
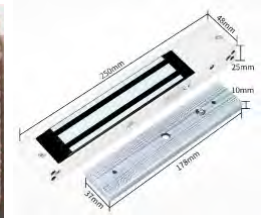

Fig.9 Door opener

Fig.10 Relay

Fig.11 Electromagnetic lock

3.4 The judgment logic of smart ore pass access control

The default state of the door is set to be closed. After the detection code runs, the screenshot of each frame of the surveillance video is continuously detected. If 5 consecutive pictures of the loader head are recognized, the Jetson Nano outputs a opening signal; if five consecutive images of the scraper tail are identified, the Jetson Nano outputs a closing signal. When the light of the underground mine vehicle is too bright and the blurred recognition rate of the front image is low, the rear of the car is used to assist the recognition.

4. Results and discussion

4.1 Underground implementation results of intelligent ore passdoor

After the installation of Jetson Nano embedded development components, door openers, door locks and other hardware devices, network cables are used to connect the Jetson processor with the camera. When the vehicle enters the camera's field of view, OpenCV is used to return the vehicle image. The Yolov3 algorithm

model is called for vehicle recognition classification, and the electronic control signal is output to the access control processor to control the brushless motor and electromagnetic lock. After the system is running, the identification and classification effect of the four types of mining vehicles in the state of constant speed driving and parking is optimal (Fig.12). After installing dual-camera, the recognition accuracy of the four types of underground mine vehicle is 95%-100%. According to the algorithm logic, the target vehicle is identified 5 times in a row, and the program will output the change of the corresponding variable value in the console. It can be seen that the program detects vehicles with rapid response and low latency. Jetson outputs the electronic control signal to the automatic door opener and electromagnetic lock for opening(closing), and the door rotates 90° in about 3s, meeting the needs of the system.
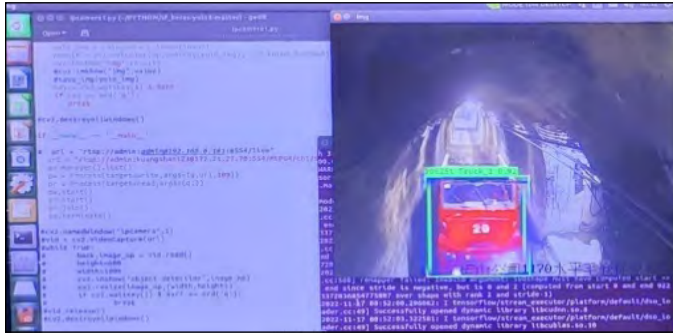

Fig. 12 Target vehicle detection screen

4.2 Problems and solutions encountered during system operation

4.2.1 Error message of memory overflow during Jetson object detection process

When Jetson uses RTSP to receive the live view of the webcam, the console displays an error message of memory overflow. The object detection program is written using OpenCV to call RTSP to pass in video frames, and the core code is as follows:

vid =cv2.VideoCapture(url)

success,img = vid.read()

cv2.imshow("object detection",img)

img is the variable of the incoming image frame by the camera. After analysis, when OpenCV is used to obtain webcam data based on RTSP protocol, the FFMPEG framework is used to process video stream data by default. However, when h264 is selected based on RTSP call to obtain webcam data format, FFMPEG cannot call libx264 encoder based on GPL license because OpenCV is MIT licensed. The program will alarm and replace it with avc1 by default, resulting in increased processing time. At the same time, due to the limited memory of the embedded system, the CPU used by the program to call the video stream is too long, resulting in memory overflow. The VideoCapture function in OpenCV follows the first-in-first-out principle when reading video stream data in H264 format. Since the program needs to obtain real-time monitoring images, it chooses to use the stack to store the latest video stream data read by VideoCapture. Finally, append and pop functions in the Python list are used to simulate a last-in, first-out stack that passes the latest frames between OpenCV and Yolo. In the case of memory overflow, the amount of stack pressure must be greater than the amount of stack output. The accumulation of a large amount of data on the stack will also cause the program to crash, and it is necessary to set a capacity cap value for the stack. When the amount of parameters stored in the stack reaches the threshold, a preset cleanup program is started; the state of the stack is reset, and memory resources are reclaimed. To ensure that the program does not overflow under long-term operation, the adjusted core code is as follows:

```
cap = cv2.VideoCapture(url)
 while success:
success,img = cap.read()
  if success:
stack.append(img)
  if len(stack) >= top:
   del stack[:]
gc.collect()
yolo = YOLO(**config)
if len(stack)!=0:
value = stack.pop()
image    =    Image.fromarray(cv2.cvtColor(value,cv2.COLOR_
BGR2RGB))
   yolo_img = yolo.detect_image(image)
   result = cv2.cvtColor(np.asarray(yolo_img), cv2.COLOR_RGB-
2BGR)
    cv2.imshow("img",result)
```

4.2.2 Too strong vehicle lights will lead to poor recognition

Underground illumination is poor, and the lights are usually turned on for safe drive. When the lights are too bright, the video collected by the surveillance screen will be blurred (as shown in Fig. 13), resulting in the program being unable to accurately identify the target cart or the accuracy of recognition is less than 80%. To this end, a webcam is installed to assist identification in the manner of Fig. 14. When the front camera picture is blurred due to direct headlights, the rear camera can avoid the area with strong lights in front of the vehicle, and provide a clearer video stream data from the rear of the vehicle for final recognition. The camera for auxiliary identification is the same model as the main camera, both are DS-2CD2T25-I5 6mm Hikvision webcams, powered by POE, and pendant. The addition of cameras allows vehicles to be well identified and accurately classified, as shown at the top left of Fig.15.

Fig. 13 Video screen of too bring car lights

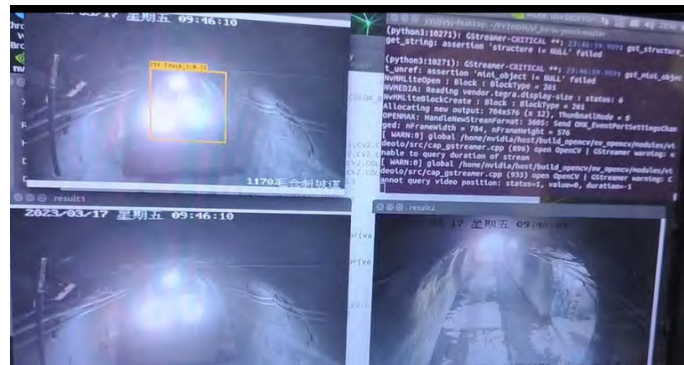*Fig. 14 Schematic diagram of dual-camera installation*

Fig.15 Recognition results of dual-camera with lights on

4.3 Analysis of the implementation effect of intelligent ore pass access control

(1) Enhanced safety protection for underground personnel. Underground miners are unable to pass through the ore pass door, ensuring the separation and control of personnel and vehicles during mining operations, and minimizing the risk of accidents.

(2) Beneficial for integration with mining processes. This intelligent ore pass system serves as a supplement to the mining process, making the control of mining area extraction and sliding systems more integrated. The centralized control room on the surface can obtain the actual situation of mining in different underground mining areas at any time.

(3) System operation and maintenance are relatively easy. The automatic opener, electromagnetic lock, door and camera of the system are located in the tunnel, while the other equipment is located in the rest chamber. Due to the narrow underground space, it is inevitable to cause scratches between the vehicle and the opened door or collision accidents may occur when the system malfunctions and the dooris not opened in a timely manner. Due to the fact that there are usually welders and material reserves in the surface workshop and underground maintenance chambers of mines, the maintenance and replacement of doors are convenient. When the camera malfunctions, the duty personnel can input instructions in the program window to manually control the opening and closing of the access control, without delaying the production of the mine.

(4) The system is easy to expand. This system is developed based on Jetson and has many reserved interfaces. In the future, new execution modules can be added at any time to achieve the intelligent infrastructure construction of the mine from monitoring center-to-switch-to-doorway-to- intelligent unit, better serving the intelligent construction of the mine.

5. Conclusion

This article constructs an intelligent unmanned control system for the underground special environment, achieving automatic identification of mining vehicles and automatic opening and closing of the pass door, achieving unmanned operation of the pass. At present, the system runs smoothly, with an average accuracy of 95% to 100% for identifying the four types of mining vehicles, and the access control response is fast with almost no delay.

In future research, image recognition algorithms can be used to develop a vehicle loading (waste rock) quantity recognition module based on existing programs, which can count the number of fully loaded and empty vehicles entering the ore pass connecting passage. This provides data support for mines to determine the ore pass material level and ore drawing time. At the same time, it can optimize the mine transportation plan based on this, reduce mine safety risks, and improve mine production efficiency.

References

Baccouche, A., Garcia-Zapirain, B., Zheng, Y., Elmaghraby, A.S. 2022. Early detection and classification of abnormality in prior mammograms using image-to-image translation and YOLO techniques. *Computer Methods and Programs in Biomedicine*, 221, 106884.https://doi.org/10.1016/j.cmpb.2022.106884

Girshick, R., Donahue, J., Darrell, T., Malik, J. 2014. Rich feature hierarchies for accurate object detection and semantic segmentation. *Proceedings of the IEEE Conference on Computer Vision and Pattern Recognition*, 580-587.

Guo, X., Li, Y. 2011. Underground Personnel Positioning System Based on ZigBee. *2011 Fourth International Symposium on Computational Intelligence and Design, Hangzhou, China, IEEE*, 1, 298-300. DOI: 10.1109/ISCID.2011.82

Imam, M., Baïna, K., Tabii, Y., Ressami, E.M., Adlaoui, Y., Benzakour, I., Abdelwahed, E.H. 2023. The Future of Mine Safety: A Comprehensive Review of Anti-Collision Systems Based on Computer Vision in Underground Mines. *Sensors (Basel, Switzerland)*, 23(9), 4294. https://doi.org/10.3390/s23094294

Kang, L., Lu, Z., Meng, L., Gao, Z. 2024. YOLO-FA: Type-1 fuzzy attention based YOLO detector for vehicle detection. *Expert Systems with Applications*, 237(Part B), 121209.https://doi.org/10.1016/j.eswa.2023.121209

Kumar, A., Kalia, A., Kalia, A., 2022. ETL-YOLO v4: A face mask detection algorithm in era of COVID-19 pandemic. *OPTIK*, 259, 169051.https://doi.org/10.1016/j.ijleo.2022.169051

Liu, W., Anguelov, D., Erhan, D., Szegedy, C., Reed, S., Fu, C. Y., & Berg, A. C. 2016. Ssd: single shot multi box detector. *In: Leibe, B., Matas, J., Sebe, N., Welling, M. (eds) Computer Vision – ECCV 2016. ECCV 2016. Lecture Notes in Computer Science, Springer, Cham*, 9905, 21-37. https://doi.org/10.1007/978-3-319-46448-0_2

Madahana, M.C.I., Nyandoro, O.T.C., Ekoru, J.E.D. 2020. Intelligent comprehensive Occupational health monitoring system for mine workers. *IFAC-PapersOnLine*, 53(2), 16494-16499. https://doi.org/10.1016/j.ifacol.2020.12.751

Redmon, J., Farhadi, A. 2016. YOLO9000: Better, faster, stronger. *arXiv preprint arXiv:1612.08242*. https://doi.org/10.48550/arXiv.1612.08242

Redmon, J., Farhadi, A. 2018. YOLOv3:an incremental improvement. *arXiv preprint arXiv:1804.02767*. https://doi.org/10.48550/arXiv.1804.02767

Ren, S.Q, He, K., Girshick, R., Sun, J. 2017. Faster R-CNN: Towards Real-Time Object Detection with Region Proposal Networks. *IEEE Translations on Pattern Analysis and Machine Intelligence*, 39(6), 1137-1149. DOI: 10.1109/TPAMI.2016.2577031

Tian,Y., Wang, S., Li, E., Yang, G., Liang, Z., Tan, M. 2023. MD-YOLO: Multiscale Dense YOLO for small target pest detection. *Computers and Electronics in Agriculture*, 213, 108233.https://doi.org/10.1016/j.compag.2023.108233

Yang,C.Y., Li, C., Su, J.C., Wang, X.Q., He, Y.R. 2016. Research on video-based system of activity recognition for coal mine safety surveillance. *Coal Engineering*, 48(4), 111-113+117.

BİLİMSEL MADENCİLİK DERGİSİ
SCIENTIFIC MINING JOURNAL

Review Article

An Overview of Halloysite Mineral

Emrah Durgut[a,*], Mustafa Çınar[b,**], Orhan Özdemir[c,***]

[a] Çanakkale Onsekiz Mart University, Can Vocational School, Çanakkale, TÜRKİYE
[b] Çanakkale Onsekiz Mart University, Department of Mining Engineering, Faculty of Engineering, Çanakkale, TÜRKİYE
[c] İstanbul Technical University, Department of Mineral Processing Engineering, Faculty of Mines, İstanbul, TÜRKİYE

A B S T R A C T

Halloysite is a type of clay mineral found in the kaolin group together with kaolinite, dickite, and nacrite minerals. Kaolinite is the most common mineral in this group, while dickite, nacrite, and halloysite are rarer. Although halloysite is primarily used in ceramic production, application in other industries is increasing and gaining economic value due to its unique properties. The use of halloysite is determined by the degree of purity and the properties of the nano-sized tubular structure. Naturally obtained halloysite mineral has a key position in the field of nanotechnology due to its unique physicochemical properties originating from its tubular structure. Also, due to its low reserves in many parts of the world, halloysite is a more economical material for the sectors compared to artificially produced nanomaterials. Halloysite reserves known in Türkiye are located in the Çanakkale and Balıkesir regions. Although there are many useful studies on halloysite in different areas, additional studies are needed to understand the nano-sized properties of halloysite ore and to ensure its use that will provide maximum benefit. This study aimed to contribute to the studies on halloysite in terms of literature by compiling studies on the characterization of halloysite minerals, reserve information, physicochemical properties, enrichment methods, and usage areas.

Keywords: Clay, Halloysite, Nanotechnology, Nanotube, Beneficiation.

1. Introduction

Halloysite ($Al_2Si_2O_5(OH)_4$) is a clay mineral composed of aluminum, silicon, oxygen, and hydrogen elements as basic components. Halloysite is typically formed by hydrothermal weathering of aluminosilicate minerals and can be found together with dickite, kaolinite, montmorillonite, and other clay minerals (Murray, 2007). Halloysite was first studied as a tubular mineral by the Belgian geologist Omalius d'Halloy, and was given this name by Berthier (1826) in honor of the mineral's discoverer. Literature studies with the term halloysite in the title, abstract, or keyword started in the 1940s and the number of studies on the subject has increased considerably with the addition of the term halloysite nanotube (HNT) since the 2000s. This clearly shows the importance of the halloysite issue (Figure 1).
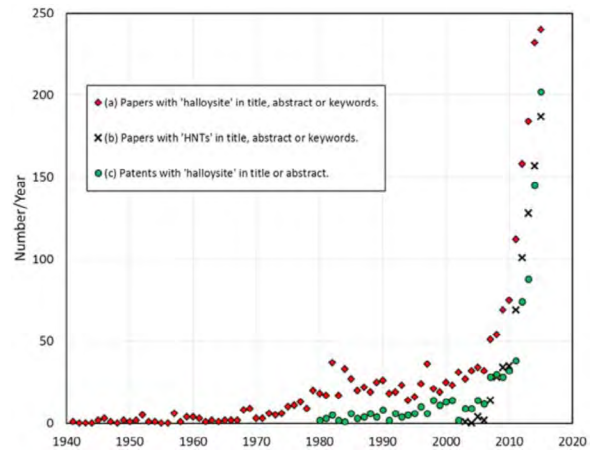

Figure 1: Number of publications on halloysite/halloysite nanotube by years (Churchman et al., 2016).

* emrahdurgut@comu.edu.tr • https://orcid.org/0000-0002-4637-7087
**Corresponding author: mcinar@comu.edu.tr • https://orcid.org/0000-0001-9553-423X
***orhanozdemir@itu.edu.tr • https://orcid.org/0000-0002-4408-546X

Halloysite mineral has been named halloysite, metahalloysite, hydrated halloysite, and endellite by different researchers due to its different morphological, structural and chemical properties (Ross and Kerr, 1934; Alexander et al., 1943; MacEwan, 1947; Churchman and Carr, 1975). Currently, halloysite mineral is classified as hydrated halloysite (basal spacing 10 Å) with chemical formula $Al_2Si_2O_5(OH)_4 \cdot 2H_2O$ and dehydrated halloysite (basal spacing 7 Å) with chemical formula $Al_2Si_2O_5(OH)_4$ according to basal XRD peaks (Brindley, 1961; Santos et al., 1965; Grim, 1968). Figure 2 shows the molecular and morphological representation of halloysite-7 Å mineral.
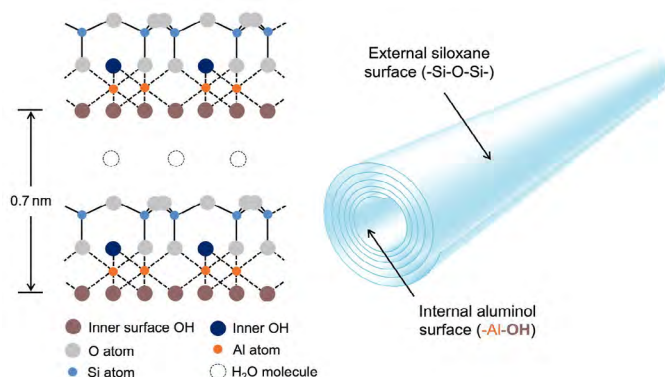

Figure 2: Molecular and morphological representation of halloysite-7 Å.

2. Characterization of halloysite mineral

Because dehydrated halloysite (7 Å) have the same chemical composition as kaolinite and give the same XRD peaks in mineralogical analysis, they must be characterized by intercalation method and/or SEM images to be separated from each other (Churchman et al., 1984; Robertson and Eggleton, 1991). In the intercalation method, dehydrated halloysite (7 Å) is brought to a hydrated (10 Å) state by various processes, and thus, it can be distinguished from kaolinite mineral due to the different basal XRD peaks (Figure 3).
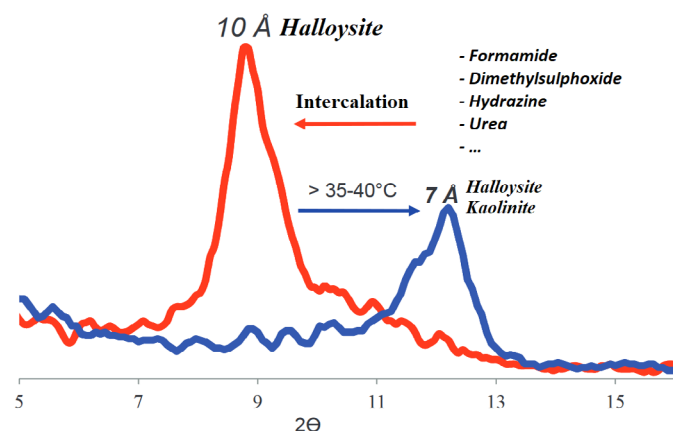

Figure 3: XRD patterns of kaolinite, halloysite-7Å and halloysite-10Å (Saklar et al., 2012a).

Intercalation of halloysite with organic compounds and salts has been studied extensively in the literature (Churchman and Theng, 1984; Frost and Kristof, 1997; Hillier and Ryan, 2002; Franco and Ruiz Cruz, 2004). After grinding halloysite-7Å with potassium acetate, the basal spacing value can be increased to 10 Å by intercalation of water and ethylene glycol. This situation does not change the basal spacing in kaolinite and dickite (Miller and Keller, 1963). Similar results obtained when hydrazine, water, and glycerol were used (Range et al., 1969). In intercalation studies with $K_3C_6H_5O_7$ (citrate), KCOOH (formate), KOCN (cyanate), KSCN (thiocyanate), and KNO_2 (nitrite) with mono, divalent, and trivalent cations, it was observed that these salts tend to intercalate between the halloysite layers. It has also been determined that halloysite intercalates with salts of monovalent (K^+, NH_4^+, Rb^+, and Cs^+) cations (Carr et al., 1978). Even if concentrated solutions are required, low solubility of silver and thallium salts in water do not allow forming compounds for efficient intercalation. In an aqueous clay suspension, halloysite interlayer regions are relatively water-repellent in contrast to the outer surface-water interface and therefore do not tend to form strong ionic species associated with water. Therefore, it can be said that the intercalation phenomenon will only be possible by cations, which have low bonding energy with water (Carr et al., 1978). It is known that the viscosity of aqueous salt solution is related to the ability of the ions to combine with water. The tendency of ions to disrupt structure is related to their electrical field strengths. Low field strength means high disrupting ability. This refers to the size and valence properties of the ions. The smaller the size, the lower the force, thus meaning lower electrical field strength. The intercalation behavior of cations is closely related to the fluidity of saline solutions. Relatively hydrophobic cations (disrupting the water structure) intercalate the water-repellent zones in halloysite-water systems. Experimental studies have shown that the tendency of very large ($Cr_2O_7^{-2}$ and $Ce(NO_3)_6^{-2}$) and highly charged (AsO_4^{-3}, $S_2O_5^{-2}$, $S_2O_3^{-2}$) anions to intercalate the interlayer spaces is quite limited. Data in studies on halloysite support that salt molecules do not completely replace water molecules in the formation of interlayer compounds and this is related to the type of salt used (Wada, 1961; Carr et al., 1978).

Because halloysite has a tubular structure, electron microscopy is a fundamental method to distinguish it from other kaolin group minerals and to investigate such materials. The development of Scanning Electron Microscopy (SEM) method has enabled new findings about halloysite, while the use of Transmission Electron Microscopy (TEM) method has made it possible to obtain information about the structure of halloysite that has never been obtained. With SEM analysis, the information on the halloysite tubular structure, and the length and width of the tubes can be obtained, while more detailed information such as individual lumen lengths and diameters of the tubes can be obtained with TEM analysis. Halloysite minerals can be observed circular or cylindrical in TEM analysis (Figure 4).
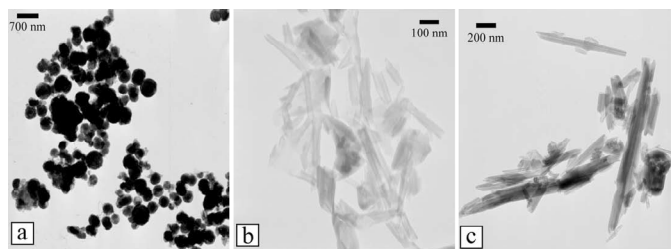
Figure 4: TEM images of three basic morphologies of New Zealand halloysite: (a)circular (Opotiki); (b)short tubes (Te Puke); (c)long tubes (Matauri Bay) (Joussein et al., 2005).

Considering the tubular structure, halloysite shows two types of structures "cylindrical" and "prismatic or polygonal" (Dixon and Mckee, 1974; Kogure et al., 2013). Ultra-high-resolution SEM imaging demonstrated the polygonization of halloysite tubes with multiple crystal surfaces (Figure 5).

Figure 5: Ultra high-resolution images a)Cylindrical tubes b)Prismatic tube images with thin sections on tube surfaces (Kogure, 2016).

Physicochemical properties such as cation exchange capacity, specific surface area, and pore volume vary according to the environmental conditions in which the halloysite is formed. Morphological differences between the halloysite and the impurities are the factors that have the most obvious effects on the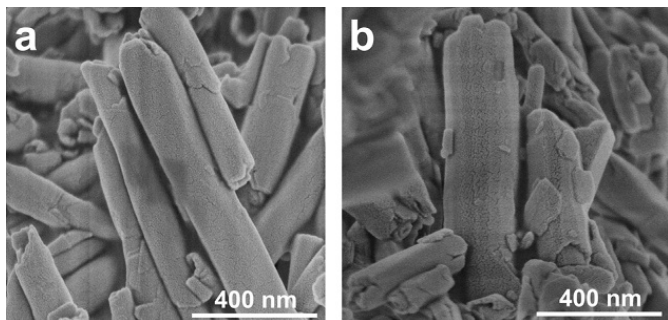 formation of specific surface area and internal pore diameter. The fact is that inner and outer surfaces have different chemical compositions that affect the surface charge at different pHs (Durgut et al., 2022a). The presence of water in the interlayer space reduces the bonding with neighboring layers. All these factors determine the use of halloysite in new areas such as nanocarriers, nano molds, and nanofillers.

Cation exchange capacity varies according to the types of clay minerals in the halloysite ores. The cation exchange is seen in the defective crystal corners, in the form of displacement in the lattice, and as the replacement of hydroxyl ions on the surface with hydrogen. According to studies in the literature, the cation exchange capacity of halloysite reaches up to 60 cmol/kg (Kunze and Bradley, 1963; Norrish, 1995; Takahashi et al., 2001; Hart et al., 2002; Joussein et al., 2007). The cation exchange capacity of halloysite decreases due to natural or artificial drying processes (Grim, 1968). Therefore, cation exchange capacities of hydrated halloysites are higher than dehydrated halloysites. In addition, halloysite has a higher cation exchange capacity than kaolinite minerals due to the structural arrangement in hydrogen bonds, the presence of negative charges, and different hydration statuses (Wilson, 2004). In addition, the cation exchange capacity of halloysite is affected by purity, particle size, and morphology. As the Al^{3+} in the octahedral layer is replaced by Fe^{2+}, the Al content decreases and the Fe content increases, and thus the cation exchange capacity of halloysite increases (Singh and Gilkes, 1992). As the particle size decreases, the cation exchange capacity of halloysite increases due to the increased edge-surface interaction (Delvaux et al., 1992; Chorover and Sposito, 1995; Wu et al., 2013). The presence of soluble salts in the pores of tubular halloysites causes a higher cation exchange capacity than halloysites in other structures (Ma and Eggleton, 1999).

The specific surface area value of halloysite also depends on purity, particle size, and acid-base treatment. Pasbakhsh et al. (2013) measured the specific surface area and porosity values of halloysites from different regions. It was observed that the highest pore volume was in nanotubes with cylindrical lumen, low impurity, and smooth thin walls. In addition, studies have shown that halloysite mineral has higher specific surface area values than kaolinite (Joussein et al., 2005).

3. Halloysite reserves, market and prices

Halloysite is found in various regions around the world. Halloysite sources are generally found near kaolinite deposits, but they can also be seen in altered rocks in the form of veins (Ece and Schroeder, 2007; Garcia de Oliveira et al., 2007).

The Matauri Bay halloysite source in the Northland of New Zealand is located next to the rhyolite rock. This source consists of approximately 50% halloysite and 50% quartz, cristobalite, and a small amount of feldspar. The Matauri Bay halloysite has a heterogeneously distributed tubular structure up to 3 mm in length and plated kaolinite. These resources have been produced at an annual rate of approximately 80000 tons since 1969. The mineral processing plant capacity produces 25000 tons/year and the lifetime of the quarry is planned to be more than 50 years. Since ore with high whiteness is obtained from this facility, it is exported to more than 20 countries, especially for use in the production of high-quality ceramic products (porcelain, fine porcelain, technical ceramics, etc.). Although Matauri Bay is the most well-known source of halloysite in New Zealand, there are also small reserves in Te Puke and Opotiki regions (Keeling, 2015; Joussein, 2016).

Halloysite deposits in the United States of America (USA) are located in the state of Utah. Approximately 1.2 million tons of halloysite have been produced in the past from the Eureka Dragon ore deposit in the Tintic mining area in Juab County. Halloysite particles have a morphology consisting of small tubes with inner diameters ranging from 5 nm to 30 nm and lengths between 50-1500 nm. The mineral contents in the samples taken from the region consist of 84% halloysite, 8% kaolinite, and other minerals (quartz, gypsum, sulfate/phosphate minerals). 501200 tons of reserve containing 64% halloysite has been calculated by means of the newly received drilling data at the Dragon mine site. Pure halloysite and a by-product with high iron content that can be used in the pigment industry are obtained from the mineral processing plant (Boden et al., 2012; Joussein, 2016).

Halloysite ore found at the Dunino mine in Lower Silesia, Poland, was formed from the weathering of basalt. Halloysite is produced by Intermark/Kopalnia Haloizytu Dunino, founded in 1998, by open pit mining near Krotoszyce in the Legnica region. The mineral deposit consists of over 10 million tons of various raw materials with homogeneous distribution. The bed thickness of the halloysite reserve, which is around 500000 tons, reaches up to 20 m in height. Dunino ore bed consists of a mixture of nanotubes and nanosheets containing 80% halloysite mineral. There are also small and homogeneously distributed iron and titanium oxides as impurities (Clarke, 2008; Keeling, 2015).

The two halloysite deposits in Türkiye were located along the contact between metamorphic rocks of the Triassic Karakaya Complex and lower Miocene volcanics (Genç, 1998). The Karakaya Complex basically consisted of Permian aged limestone masses and also contained phyllite and schist. There was a lower Miocene aged volcanogenic pile consisting of andesitic pyroclastic/lava on the basement rocks. It also contained tertiary aged granitic intrusions cutting the Karakaya Complex and andesitic pyroclastics. There was an occurrence of halloysite in the volcanogenic pile, formed in relation to limestone, with a width of approximately 45-50 m, a length of 125-130 m and a depth of approximately 12-15 m in the north-south direction. There were also limestone blocks of different sizes in the occurrence. In addition to halloysite minerals in the region, there were also minerals such as kaolinite, smectite, illite, alunite, jacobsite, pyrochroite, hematite, goethite and birnessite. It was thought that halloysitization occurred as a result of hydrothermal solutions of magmatic origin rising along faults and affecting andesitic pyroclastic. It was thought that one of the most important factors in the formation of halloysite was the limestone that regulated the pH of the environment (Laçin and Yeniyol, 2006). Kaolinite and halloysite quarries belonging to Esan Eczacıbaşı are located in Balıkesir and Çanakkale regions in Türkiye. Halloysite resources found here are considered important because they are quite pure. It is known that there are 50000 tons of halloysite reserves in the region (Ece et al., 2008). While the diameters of halloysite tubes in Tabanköy vary between 40-50 nm, their lengths can reach up to 1500 nm (Demir and Altaş, 2017).

In China, there are kaolin deposits consisting of a mixture of plated kaolinite and tubular halloysite. Longyan reserves in the Fujian Region are halloysite deposits with low iron and titanium content formed by the kaolinitization of granites. On the other hand, there are also important resources in Dafang, Qingxi, Zunyi, and Shijin in the Guizhou District. Dafang halloysite consists of tubular fine particles with very low iron and titanium contents. However, the ore beds in this region were formed in the form of small veins. While the annual production amount of Longyan District is 50000 tons, this value is 2000 tons in Gouzhiu District (Wilson, 2004).

In the Eucla Basin region of South Australia, near Playa Lake, there are halloysite reserves with a purity of 95% and a very regular morphology up to a tube length of 1500 nm. There are halloysite deposits with thin and long veins in Jarrahdale in the north and Patch Clay in the west of Australia (Joussein, 2016).

In the Thung Yai region of South Thailand, there are deposits containing approximately 70% halloysite, consisting of micro-tubes with pores and sheets 80-200 nm in diameter and 450-500 nm in length. Quartz and anatase can be seen as impurities in these deposits. In addition, in the Ranong and Narathiwat regions of Southern Thailand, there are ore beds containing 70% tubular halloysite and kaolinite as co-minerals, quartz, mica, and potassium feldspar as trace minerals (Bordeepong et al., 2012).

Large sources of halloysite are known to exist in Japan (Sudo and Takahashi, 1955; Saigusa et al., 1978) and South Korea (Jeong, 1998; Khan and Kim, 1991). There are tubular halloysite sources with low iron and titanium contents in Brazil (Wilson et al., 2006). Halloysite deposits are found in the southwest of the Rio Negro region in Argentina (Cravero et al., 2012). Table 1 shows the chemical, mineralogical, morphological, and physical properties of halloysites from some important countries around the world.

Table 1: Chemical, mineralogical, and physical properties of halloysites in the world (Joussein, 2016).

Country	New Zealand	USA	New Zealand	Australia	China	Poland	Türkiye
Name	Matauri Bay	Dragon Mine	Te Puke	Camel Lake	Longyan	Dunino processed	Turkish
SiO_2	50.40	43.50	44.82	44.96	48.00	43.30	46.00
Al_2O_3	35.50	38.80	36.70	37.57	38.00	34.50	37.01
Fe_2O_3	0.25	0.33	3.40	1.21	0.29	2.60	0.70
MgO	trace	0.12	0.01	0.19	0.30	0.08	0.45
Na_2O	trace	0.07	0.01	0.09	0.10	0.19	0.10
K_2O	trace	0.07	0.05	0.31	1.71	0.05	0.30
CaO	trace	0.26	0.01	0.28	0.16	0.26	0.15
TiO_2	0.05	0.02	0.37	0.15	0.02	1.18	0.30
MnO	0.01	0.01	0.01	0.01	trace	trace	trace
P_2O_5	0.06	0.83	0.02	0.01	unknown	0.05	unknown
SO_3	0.06	0.26	0.02	0.63	unknown	unknown	unknown
LOI	13.80	15.70	14.66	14.53	12.40	15.39	15.00
Halloysite (%)	96	84	98	95	79 (Hal/Kaol)	70-80	95
Accessory minerals	quartz cristobalite anatase	kaolinite quartz gibbsite alunite	quartz cristobalite anatase	quartz alunite anatase Fe oxides	mica minerals quartz anatase	quartz anatase	quartz alunite anatase feldspar
Morphology	Tube/platy	Tube	Blocky and short tubes	Tube	Tube/platy	Tube/ platy	Tube
CEC ($cmol_c$/ kg)	2.5	2.1	5.2	18.8	unknown	9.1	4.2
BET (m^2/g)	22.1	57.3	33.31	74.6	unknown	unknown	72.2

The quarry sales prices were 27.5 TL/ton for kaolin and 808.5 TL/ton for halloysite in 2019 (General Directorate of Mining and Petroleum Affairs, 2019). Here, the price difference for the mineral with the same chemical structure explains the importance of halloysite. On the other hand, the price of halloysite ore of purity to be used in plastics, polymers, and medicine reaches up to AU\$5000/ton (Andromeda Metals, 2019). Thus, it is seen that the price of beneficiated halloysite ore, has increased significantly. When halloysite nanotubes are considered as an alternative material to carbon nanotubes, they appear to be biologically harmless. It is also known that the price of halloysite nanotubes (US\$4/kg) is quite economical compared to carbon nanotubes (US\$500/kg) (Bordeepong et al., 2011).

The worldwide halloysite market was 29.1 million US\$ in 2017. It is estimated that this figure will reach 50.21 million US\$ in 2025. Figure 6 shows the distribution of the halloysite market in the USA by the area of use.

Figure 6: Halloysite market in the USA by the area of use between 2014-2025 (https://www.grandviewresearch.com/industry-analysis/halloysite-market).

4. Uses and beneficiation methods of halloysite

There are some decisive criteria for the use of halloysite, and these criteria vary according to the area of use. Uygun (1999) stated that the chemical and mineralogical properties sought in halloysites exported to England should have a minimum of 35% Al_2O_3, a maximum of 0.7% Fe_2O_3, a maximum of 1.2% SO_3 and a minimum of 92% halloysite, a maximum of 5% quartz, and a maximum of 3% alunite contents.

The beneficiation methods of halloysite is similar to kaolinite beneficiation methods. However, grinding of halloysite causes changes in the nano-sized tubular structure and negatively affects the product properties (Takahashi, 1957). When the halloysite is ground, it gradually turns into an irregular structure and XRD peak intensities weaken, that is, the peak intensity that determines halloysite-10 Å decreases with grinding. As the grinding duration progresses, mullite crystals grow. On the other hand, the density decreases and reaches a constant value. This constant value is close to the density of silica-alumina gel or allophane. While the milled halloysite sample from the electron microscope images has a tubular structure at the beginning of the grinding process, fine crystals with sharp corners are obtained as the grinding progresses, the fine crystals later come together and the particle size increases, and finally irregular spherical particles are formed. As a result, the particle size increases irregularly with agglomeration, resulting in a silica gel-like structure (Takahashi, 1959a). In wet grinding of halloysite, unit layers are rolled over each other due to the tubular structure compared to dry grinding, and therefore it becomes difficult to form cleavage in wet grinding. While the density of halloysite increases gradually at first, it tends to decrease after reaching a certain value. In wet grinding, the corners of the layered kaolinite crystals begin to curl and turn into a tubular structure similar to halloysite. In the halloysite, different structures with broken tubular, layered, and rectangular shapes were

observed. This shows that wet milling causes crushing rather than cutting force (Takahashi, 1959b). As a result, cracking and crushing effects were observed more in dry grinding, while weak cleavage effects were observed for kaolinite and weak crushing effects for halloysite in wet grinding.

After the industrially quarried halloysite ore is brought to the mineral processing facility, it is mixed in large pools and dispersed, and size separation is made with hydrocyclones to separate the coarse-sized minerals. Important impurity source minerals in halloysite and kaolinite deposits are goethite and muscovite. They may also contain quartz, feldspar, gibbsite, smectite group clay minerals, and anatase. Very fine-sized impurities in the structure are defined chemically by EDX analysis, and exact mineral types cannot be determined. Iron oxide/hydroxide minerals, which are in the form of extremely fine-sized submicron particles, may be trapped between clay minerals or adhered on halloysite tubes-kaolinite plates. Because the grinding process disrupts the structure of halloysite nanotubes, dispersing it into a fine size by mechanical dispersion in the aqueous medium ensures that the nano-tubes are less damaged than grinding and that the hard impurities remain large without grinding and are separated from the halloysite by particle size separation methods (Durgut et al., 2022b).

Magnetic minerals such as hematite, magnetite, and biotite are removed by magnetic separators with proper field strengths. In order to further purify the halloysite ore, the iron content is reduced to a very low level by leaching methods using organic and inorganic acids. Saklar et al. (2012b) reported that as a result of high-field intensity wet magnetic separation experiments of halloysite ores in Çanakkale and Balıkesir regions, the magnetic separation is not efficient because the hydraulic drag force is more effective on fine-sized particles and higher magnetic field strength is needed. Solvent type and temperature are very important in removing impurities by leaching from the halloysite. There is no effective separation at low temperatures (25°C), hence leaching can be performed efficiently at higher temperatures (80°C). It is known from the literature that oxalic acid is a good solvent for removing ferrous impurities in the structure of clays (Ambikadevi and Lalithambika, 2000; Baba et al., 2015). Because some alumina may also dissolve from the clay surface at high acid concentrations, the structure of halloysite should be carefully examined (Belkassa et al., 2013; Saklar and Yörükoğlu, 2015). Leaching and wet magnetic separation can be used together to efficiently purify halloysite in the fine-sized fractions (Sakiewicz and Lutynski, 2016; Sakiewicz et al., 2016).

Fine quartz particles in clay ores are removed by flotation (Bidwell, 1970). Fatty acids and cationic collectors can be used in halloysite flotation. In halloysite flotation with sodium oleate, a low basic pH (8.2) is more efficient than a high basic pH (12.5). In this case, the pH of the environment increases the interaction of collector and the mineral surfaces by converting the aluminum hydroxides into aluminates, thus increasing the flotation performance. Sodium ions from collectors are firmly adsorbed on the surfaces in flotation studies. In order to remove these ions from the surfaces, the samples must be thoroughly washed (Uvarov and Vovk, 1971). While sodium fluosilicate, aluminum sulfate, and dextrin have a depressant effect on halloysite minerals, there is no such effect for sodium silicate (Yapa, 1993).

Halloysite is more conductive under a voltage of 10000 volts for electrostatic separation operations. However, the liberation size of the mineral should be above 0.1 mm (Yapa, 1993).

Alkaline treatment, ultrasonication, and centrifugation methods can be used to improve the dispersion properties of halloysite nanotubes in suspensions, to remove impurities by preventing agglomeration, and to separate nanotubes into separate size fractions. Surface modification with organosilane compounds and amine salts has positive effects on the dispersion of halloysite

tubes (Abbasi, 2018). Kaolin group clay minerals are generally enriched efficiently in aqueous media. The flowchart of a typical process applied in the enrichment of such minerals in aqueous media is given in Figure 7.
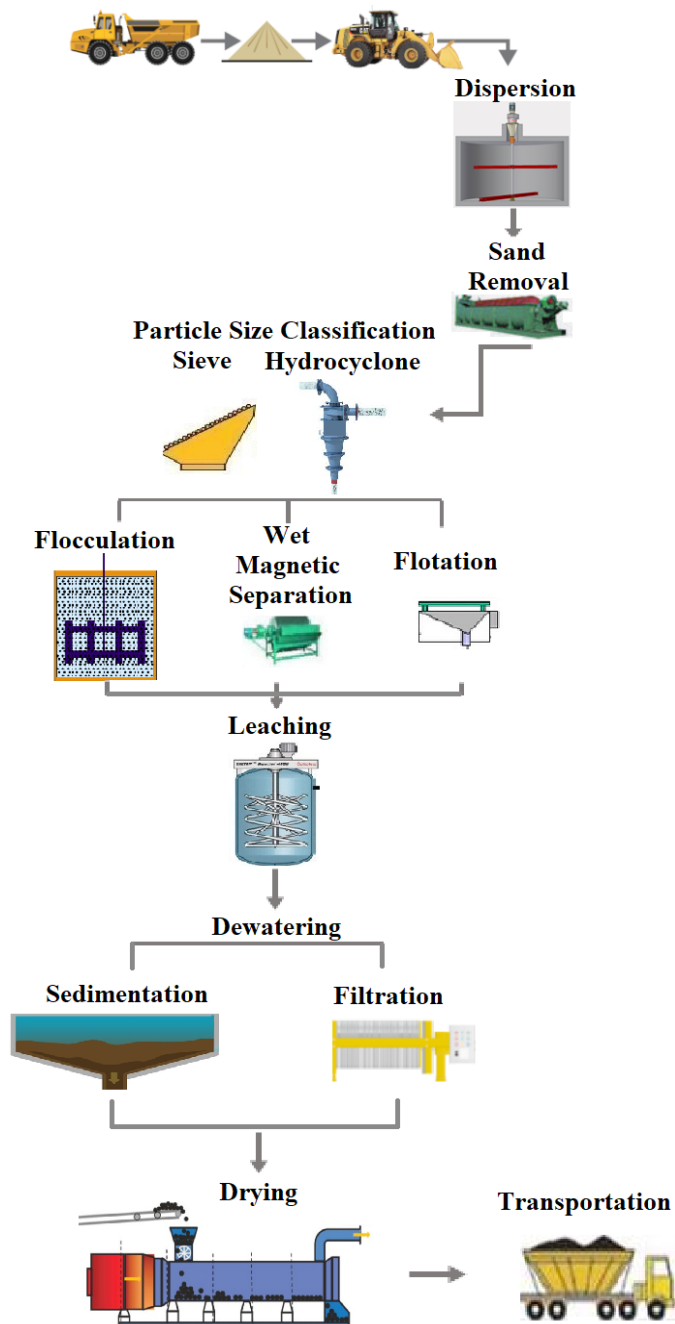

Figure 7: Flowchart of a typical wet kaolin clay mineral processing and enrichment.

If additional particle size separation is required after enrichment, hydrocyclone is used again, and then filter press or rotary filters are used to remove moisture (Murray, 2006). In this way, the halloysite can remain in a hydrated (10 Å) form. If spray dryers are used during drying, halloysite turns into a dehydrated (7 Å) form due to the appeared high temperature. It has been reported in the literature that the hydrated (10 Å) structure turns into a dehydrated (7 Å) structure by losing the water between the layers within 50-150°C (Joussein et al., 2006; Saklar et al., 2012a; Başara and Saklar, 2015). The process of removing the water depending on the desired structure is important at this point.

Halloysite is classified as a harmless and biocompatible nano-material in nature according to the Environmental Protection Agency (EPA 4A). Halloysite is a fine-sized ore with a large surface area and excellent dispersion in the matrix. It also has a high cation exchange capacity. There is a growing interest in using halloysite in various applications such as clay-polymer nanocomposites, catalysis, and adsorption. This unique nano-clay mineral is preferred in such applications due to its one-dimensional tubular structure and properties that can be changed by modification of the inner/outer surfaces. Therefore, tubular clay minerals are used as advanced functional materials. Drug-active substances are also adsorbed on halloysite surfaces. As such, it provides homogeneity, gives consistent release rates, and prevents overdose. Compared to organic carriers, halloysite-based drug delivery systems are long-lasting and non-toxic even at high drug dosages. This gives a powerful healing effect. Halloysite reduces the cost of surface-active materials due to its adsorption feature on the surface. Thanks to this feature, it can be used in cream, powder, gel, spray, and lotion forms. On the other hand, reusability is another important feature of halloysite.

5. Conclusions and recommendations

Natural halloysite is a low-cost industrial mineral that can be used in the production of functional materials such as nano-sized carriers. Halloysite has long been used in the production of porcelain, kitchen, and bathroom ceramics due to the properties such as whiteness and translucency that it brings to the product after sintering due to its low iron and titanium contents. In addition, due to fine particle size, it is also used in areas such as suspension-supporting agents in glaze applications. Purified halloysite nanotubes are coated with metallic and other additives and gain various electrical, chemical, and physical properties. Halloysite is used as a filling material in rubber production, and when used in polymers and cement, it improves the mechanical properties of the material. The choice of halloysite in these areas is determined by the lumen volume, shape, and size. As the tube length-to-diameter ratio of halloysite increases, technical characteristics such as strength, durability, active ingredient loading/release capacity of cement, polymer, and drug improves. Halloysite nanotubes add more strength to this structure when compared to other clay minerals that are frequently used in polymer nanocomposites. Halloysite is used in cosmetics, home and personal care materials, pesticides, medical products, and similar fields based on the principle of adsorption of active ingredients on the surfaces of nanotubes and the controlled release of these components. Understanding of the physicochemical properties of halloysite is important in terms of adding more value to the areas where it is used. How the surface and structural modification of halloysite affects the cation exchange capacity and dispersion behavior, and the details of the chemical processes on the transformations in the tubular structure of halloysite need to be studied in detail. As a result, the value of halloysite deposits in Türkiye is increasing day by day in terms of both direct raw material export and production of high-quality products. For this reason, studies on the development of processes for more efficient production of high-quality materials obtained from halloysite deposits with beneficiation operations within the scope of zero waste in proper areas gain importance for the future. The rapid increase in the number of scientific studies and publications on this material from the past to the present confirms this situation.

References

Abbasi, S. 2018. Purification, size separation and ionic functionalization of halloysite nanotubes. Master's Thesis, Graduate School of Engineering and Natural Sciences.

Alexander, L.T., Faust, G.T., Hendricks, S.B., Insley, H., McMurdie, H.F. 1943. Relationship of the clay minerals halloysite and endellite. American Mineralogist 28, 1-18.

Ambikadevi, V.R., Lalithambika, M. 2000. Effect of organic acids on ferric iron removal from iron-stained kaolinite. Applied Clay Science 16, 133-145. https://doi.org/10.1016/S0169-1317(99)00038-1

Andromeda Metals. 2019. An emerging force in industrial minerals. https://announcements.asx.com.au/asxpdf/20191009/pdf/449b-cwl4mzfpck.pdf [Accessed October 12, 2023].

Baba A.A, Mosobalaje M.A., Ibrahim A.S., Girigisu S., Eletta O.A.A, Aluko F.I., Adekola F.A. 2015. Bleaching of a Nigerian kaolin by oxalic acid leaching. Journal of Chemical Technology and Metallurgy 50(5), 623-630.

Başara, B., Saklar, S. 2015. Halloysite intercalation of northwest Anatolia. Bulletin of the Mineral Research and Exploration 150, 121-130. https://doi.org/10.19111/bmre.44287

Belkassa K., Bessaha F., Marouf K., Batonneau I., Comparot J., Khelifa A. 2013. Physicochemical and adsorptive properties of a heat-treated and acid-leached Algerian halloysite. Colloids and Surfaces A: Physicochemical and Engineering Aspects 421, 26-33. https://doi.org/10.1016/j.colsurfa.2012.12.048

Berthier, P. 1826. Analyse de l'halloysite. Annales de Chimie et de Physique 32, 332-335.

Bidwell, J.I. 1970. Separation of minerals. United States Patent No:3539003.

Boden, T., Vanden Berg, M., Krahulec, K., Tabet, D. 2012. Utah's extractive resource industries 2012: Utah Geological Survey. Natural Resources Map and Bookstore, Salt Lake City, ISBN: 978-1-55791-884-0.

Bordeepong, S., Bhongsuwan, D., Pungrassami, T., Bhongsuwan, T. 2011. Characterization of halloysite from Thung Yai District, Nakhon Si Thammarat Province, in Southern Thailand. Songklanakarin Journal of Science and Technology 33(5), 599-607.

Bordeepong, S., Bhongsuwan, D., Pungrassami, T., Bhongsuwan, T. 2012. Mineralogy, chemical composition and ceramic properties of clay deposits in southern Thailand. Kasetsart Journal - Natural Science 46(3), 485-500.

Brindley G.W. 1961. Kaolin, serpentine and kindred minerals. pp. 51-131 in: The X-ray identification and crystal structures of clay minerals (G. Brown, Editor). Mineralogical Society, London.

Carr, R.M., Chaikum, N., Patterson, N. 1978. Intercalation of Salts in Halloysite. Clays and Clay Minerals 26(2), 144-152. https://doi.org/10.1346/CCMN.1978.0260210

Churchman, G.J., Carr, R.M. 1975. The definition and nomenclature of halloysites. Clays and Clay Minerals 23(5), 382-388. https://doi.org/10.1346/CCMN.1975.0230510

Churchman, G.J., Theng, B.K.G. 1984. Interactions of halloysites with amides: mineralogical factors affecting complex formation. Clay Minerals 19(2), 161-175. https://doi.org/10.1180/claymin.1984.019.2.04

Churchman G.J., Whitton J.S., Claridge G.G.C., Theng B.K.G. 1984. Intercalation method using formamide for differentiating halloysite from kaolinite. Clays and Clay Minerals 32(4), 241-248. https://doi.org/10.1346/CCMN.1984.0320401

Churchman, G.J., Pasbakhsh, P., Lowe, D.J., Theng, B.K.G. 2016. Unique but diverse: some observations on the formation, structure and morphology of halloysite. Clay Minerals 51, 395-416. https://doi.org/10.1180/claymin.2016.051.3.14

Chorover, J., Sposito, G., 1995. Surface charge characteristics of kaolinitic tropical soils. Geochimica et Cosmochimica Acta 59, 875-884. https://doi.org/10.1016/0016-7037(94)00357-2

Clarke, G. 2008. Tubular clays. Industrial Minerals. March, 58-59.

Cravero, F., Maiza, P.J., Marfil, S.A. 2012. Halloysite in Argentinian deposits: origin and textural constraints. Clay Minerals 47(3), 329-340. https://doi.org/10.1180/claymin.2012.047.3.04

Delvaux, B., Tessier, D., Herbillon, A., Burtin, G., Jaunet, A.-M., Vielvoye, L. 1992. Morphology, texture, and microstructure of halloysitic soil clays as related to weathering and exchangeable cation. Clays and Clay Minerals 40(4), 446-456. https://doi.org/10.1346/CCMN.1992.0400409

Demir, T.U., Altaş A. 2017. Determination of Tabanköy halloysite's characteristics. 17.National Clay Symposium, 4-7 October 2017 Muğla, Muğla Sıtkı Koçman University, e-ISBN: 978-605-4397-62-4.

Dixon, J.B., McKee, T.R. 1974. Internal and external morphology of tubular and spheroidal halloysite particles. Clays and Clay Minerals 22, 127-137. https://doi.org/10.1346/CCMN.1974.0220118

Durgut, E., Çınar, M., Terzi, M., Ünver, I.K., Yıldırım, Y., Özdemir, O. 2022a. Evaluation of different dispersants on the dispersion/sedimentation behavior of halloysite, kaolinite, and quartz suspensions in the enrichment of halloysite ore by mechanical dispersion. Minerals 20(11), 1426. https://doi.org/10.3390/min12111426

Durgut, E., Çınar, M., Terzi, M., Ünver, I.K., Yıldırım, Y., Boylu. F., Özdemir, O. 2022b. Effect of blunging/dispersion parameters on separation of halloysite nanotubes from gangue minerals. Minerals 12(6), 683. https://doi.org/10.3390/min12060683

Ece, O.I., Schroeder, P.A. 2007. Clay mineralogy and chemistry of halloysite and alunite deposits in the Turplu area, Balikesir, Turkey. Clays and Clay Minerals 55(1), 18-35. https://doi.org/10.1346/CCMN.2007.0550102

Ece, O.I., Schroeder, P.A., Smilley, M.J., Wampler, J.M. 2008. Acid-sulphate hydrothermal alteration of andesitic tuffs and genesis of halloysite and alunite deposits in the Biga Peninsula, Turkey. Clay Minerals 43(2), 281-315. https://doi.org/10.1180/claymin.2008.043.2.10

Franco, F., Ruiz Cruz, M.D. 2004. Factors influencing the intercalation degree ('reactivity') of kaolin minerals with potassium acetate, formamide, dimethylsulphoxide and hydrazine. Clay Minerals 39(2), 193-205. https://doi.org/10.1180/0009855043920130

Frost, R.L., Kristof, J. 1997. Intercalation of halloysite: A Raman spectroscopic study. Clays and Clay Minerals 45(4), 551-563. https://doi.org/10.1346/CCMN.1997.0450407

Garcia de Oliveira, M. T., Furtado, S. M., Formoso, M.L.L., Eggleton, R.A., Dani, N. 2007. Coexistence of halloysite and kaolinite - a study on the genesis of kaolin clays of Campo Alegre Basin, Santa Catarina State, Brazil. Anais da Academia Brasileira de Ciências 79(4),665-681. https://doi.org/10.1590/S0001-37652007000400008

General Directorate of Mining and Petroleum Affairs. 2019. http://www.mapeg.gov.tr/Duyurular/duyuru_dukuman/obsf/2018-IV-A%20Grubu%20OBSF.pdf (Accessed February 17, 2021).

Genç, C.Ş. 1998. Evolution of the Bayramic, magmatic complex, northwestern Anatolia. Journal of Volcanology and Geothermal Research 85, 233-249. https://doi.org/10.1016/S0377-0273(98)00057-2

Grim, R.E. 1968. Clay Mineralogy. McGraw-Hill, New York.

Hart, R.D., Gilkes, R.J., Siradz, S., Singh, B. 2002. The nature of soil kaolins from Indonesia and Western Australia. Clay and Clay Minerals 50(2), 198-207. https://doi.org/10.1346/000986002760832793

Hillier, S., Ryan, P.C. 2002. Identification of halloysite (7 Å) by ethylene glycol solvation: the 'MacEwan effect'. Clay Minerals 37(3), 487-496. https://doi.org/10.1180/0009855023730047

https://www.grandviewresearch.com/industry-analysis/halloysite-market (Accessed February 18, 2021).

Jeong, G.J. 1998. Vermicular kaolinite epitactic on primary phyllosilicates in the weathering profiles of anorthosite. Clays and Clay Minerals 46, 509-520. https://doi.org/10.1346/CCMN.1998.0460504

Joussein, E. 2016. Geology and mineralogy of nanosized tubular halloysite, Nanosized Tubular Clay Minerals Halloysite and Imogolite. In: Yuan P., Thill A., Bergaya F. (ed.), Chapter 2, Elsevier, Amsterdam, ISBN: 978-0-08-100293-3, 12-49.

Joussein, E., Petit, S., Churchman, J., Theng, B., Righi, D., Delvaux, B. 2005. Halloysite clay minerals-A review. Clay Minerals 40(4), 383-426. https://doi.org/10.1180/0009855054040180

Joussein, E., Petit, S., Fialips C., Vieillard P., Righi D. 2006. Differences in the dehydration-rehydration behavior of halloysites: New evidence and interpretations. Clays and Clay Minerals 54(4), 473-484. https://doi.org/10.1346/CCMN.2006.0540408

Joussein, E., Petit, S., Delvaux, B. 2007. Behaviour of halloysite clay under formamide treatment. Applied Clay Science 35(1), 17-24. https://doi.org/10.1016/j.clay.2006.07.002

Keeling, J.L. 2015. The mineralogy, geology and occurrences of halloysite, Natural Mineral Nanotubes: Properties and Applications, In: Pasbakhsh P., Churchman G.J. (ed.), Chapter 5, Apple Academic Press, New York, eBook ISBN: 9780429172359, 95-117.

Khan, A.M. Kim, S.J. 1991. Mineralogy of halloysite from Suryun, Korea. Geological Bulletin-University of Peshawar. 24, 63-70.

Kogure, T., Mori, K., Drits, V.A., Takai, Y. 2013. Structure of prismatic halloysite. American Mineralogist 98, 1008-1016. https://doi.org/10.2138/am.2013.4385

Kogure, T. 2016. Characterisation of halloysite by electron microscopy. Yuan, P., Thill, Antoine., Bergaya, F. (Ed.). Nanosized Tubular Clay Minerals, Elsevier Publications. Netherlands, 92-114.

Kunze, G., Bradley, W. 1963. Occurrence of a tabular halloysite in a Texas soil. Clay and Clay Minerals 12, 523-527. https://doi.org/10.1346/CCMN.1963.0120145

Laçin, D., Yeniyol, M. 2006. An example to the halloysite deposits formed associated with the andesitic pyroclastics: Soğucak halloysite deposit (Yenice-Çanakkale). Istanbul Earth Sciences Review 19(1), 27-41.

Ma, C., Eggleton, R.A. 1999. Cation exchange capacity of kaolinite. Clays and Clay Minerals 47(2), 174-180. https://doi.org/10.1346/CCMN.1999.0470207

MacEwan, D.M.C. 1947. The nomenclature of the halloysite minerals. Mineralogical Magazine and Journal of the Mineralogical Society 28(196), 36-44. https://doi.org/10.1180/minmag.1947.028.196.08

Miller, W.D., Keller, W.D. 1963. Differentiation between endellite halloysite and kaolinite by treatment with potassium acetate and ethylene glycol. Clays and Clay Minerals 10(1), 244-253. https://doi.org/10.1346/CCMN.1961.0100120

Murray, H.H. 2006. Applied Clay Mineralogy. Occurrences, Processing and Application of Kaolins, Bentonites, Palygorskite-Sepiolite, and Common Clays, Edited by Haydn H. Murray, Volume 2, Pages 1-180 (2006).

Murray, H.H. 2007. Applied Clay Mineralogy: Developments in Clay Science 2, Elsevier, Amsterdam.

Norrish, K. 1993. An unusual fibrous halloysite. Clays-Controlling the environment. pp. 275-284. In G.J. Churchman et al. (ed.) 10. Int. Clay Conf., Adelaide, Australia, CSIRO Publ.

Pasbakhsh, P., Churchman, G.J., Keeling, J.L. 2013. Characterisation of properties of various halloysites relevant to their use as nanotubes and microfibre fillers. Applied Clay Science 74, 47-57. https://doi.org/10.1016/j.clay.2012.06.014

Range, K.J., Range, A., Weiss, A. 1969. Fire-clay kaolinite or fire-clay mineral? Experimental classification of kaolinite-halloysite minerals. pp. 3-13 in: Proceedings of the International Clay Conference 1969, Tokyo (L. Heller, editor). Israel University Press, Jerusalem.

Robertson, I.D.M., Eggleton, R.A. 1991. Weathering of granitic muscovite to kaolinite and halloysite and plagioclase-derived kaolinite to halloysite. Clays and Clay Minerals 39, 113-126. https://doi.org/10.1346/CCMN.1991.0390201

Ross, T.J., Kerr, P.F. 1934. Halloysite and allophane. US Geological Survey, Department of the Interior. 185-G, 135-148.

Saigusa, M., Shoji, S., Kato, T. 1978. Origin and nature of halloysite in Ando soils from Towada tephra, Japan. Geoderma 20, 115-129. https://doi.org/10.1016/0016-7061(78)90039-3

Sakiewicz, P., Lutynski, M. A. 2016. Purification of Dunino halloysite by H_2SO_4 leaching and magnetic separation, E3S Web of Conferences 8, 25-28 September 2016 Swieradow-Zdroj, Poland, EDP Sciences, eISSN: 2267-1242, 1-6.

Sakiewicz, P., Lutynski, M., Soltys, J., Pytlinski, A. 2016. Purification of halloysite by magnetic separation. Physicochemical Problems of Mineral Processing 52(2), 991-1001. http://dx.doi.org/10.5277/ppmp160236

Saklar, S., Ağrılı, H., Zimitoğlu, O., Başara, B., Kaan, U. 2012a. The characterization studies of the Northwest Anatolian halloysites/kaolinites. Bulletin of the Mineral Research and Exploration 145, 48-61.

Saklar, S., Ergün, Ş.L., Gülsoy, Ö.Y. 2012b. Beneficiation studies of halloysite and halloysite/kaolinite ores from Northwestern Anatolia. Bilimsel Madencilik Dergisi 51(1), 23-33.

Saklar, S.,Yorukoglu, A. 2015. Effects of acid leaching on halloysite. Physicochemical Problems of Mineral Processing 51(1), 83-94. https://doi.org/10.5277/ppmp150108

Santos, P.S., Brindley, G.W., Santos, H.D. 1965. Mineralogical Studies of Kaolinite-Halloysite Clays Part III. A Fibrous Kaolin Mineral from Piedade, São Paulo, Brazil. American Mineralogist 50(5-6), 619-628.

Singh, B., Gilkes, R. 1992. An electron optical investigation of the alteration of kaolinite to halloysite. Clays and Clay Minerals 40(2), 212-229. https://doi.org/10.1346/CCMN.1992.0400211

Sudo, T., Takahashi, H. 1955. Shapes of halloysite particles in Japanese clays. Clays Clay Minerals 4, 67-79. https://doi.org/10.1346/CCMN.1955.0040110

Takahashi, H. 1957. Effect of dry grinding on kaolin minerals. Clays and Clay Minerals 6(1), 279-291. https://doi.org/10.1346/CCMN.1957.0060121

Takahashi, H. 1959a. Effect of dry grinding on kaolin minerals. III. Halloysite. Bulletin of the Chemical Society of Japan 32(10), 252-263. https://doi.org/10.1246/bcsj.32.252

Takahashi, H., 1959b. Wet grinding on kaolin minerals. Bulletin of the Chemical Society of Japan 32(4), 381-387. https://doi.org/10.1246/bcsj.32.381

Takahashi, T., Dahlgren, R.A., Theng, B.K.G., Whitton, J.S., Soma, M. 2001. Potassium-selective, halloysite-rich soils formed in volcanic materials from northern California. Soil Science Society of America Journal 65(2), 516-.526. https://doi.org/10.2136/sssaj2001.652516x

Uvarov, V.S., Vovk, N.E. 1971. Flotation of alunite and clay minerals. Soviet Mining Science 7, 436-437. https://doi.org/10.1007/BF02501579

Uygun, A. 1999. Geology and origin of same carbonate-hosted halloysite deposits in Nw - Anatolia. Bulletin of the Mineral Research and Exploration 121, 141-151.

Wada, K. 1961. Lattice expansion of kaolin minerals by treatment with potassium acetate. American Mineralogist 46(1-2), 78-91.

Wilson, I.R., 2004. Kaolin and halloysite deposits of China. Clay Minerals 39(1), 1-15. https://doi.org/10.1180/000985543910116

Wilson, I.R., de Souza Santos, H., de Souza Santos, P. 2006. Kaolin and halloysite deposits of Brazil. Clay Minerals 41(3), 697-716. https://doi.org/10.1180/0009855064130213

Wu, H., Watanabe, H., Ma, W., Fujimoto, A., Higuchi, T., Uesugi, K., Takeuchi, A., Suzuki, Y., Jinnai, H., Takahara, A. 2013. Robust liquid marbles stabilized with surface-modified halloysite nanotubes. Langmuir 29(48), 14971-14975. https://doi.org/10.1021/la4041858

Yapa, N. 1993. Beneficiation of alunite bearing kaolinite, Ph.D. Thesis, Institute of Science and Technology, Istanbul Technical University.

BİLİMSEL MADENCİLİK DERGİSİ
SCIENTIFIC MINING JOURNAL

Review Article

Applications of DEM Particle Breakage Models in Mineral Industrial

Sevgi Karaca[a,*], Ali Uçar[a**]

[a] Kutahya Dumlupınar University, Department of Mining Engineering, Kutahya, TURKEY

A B S T R A C T

Modeling processes are carried out in the mineral industry as well as in many areas depending on the development of computer technologies and software. Discrete Element Method (DEM) is used in modeling studies to explain the interaction of particles with other particles and communication equipment. The DEM provides the capability to simulate the movement of the granular media in a series of computational processes of each individual particle that consists of the granular media. It is becoming increasingly widely used to predict energy consumption, wear, particle breakage and particle size distribution in crushing and grinding processes that can be described in terms of granular materials using DEM. The selection of particle breakage models used by commercial software for modeling DEM particle breakage is important. In this study, it is summarized the studies have been carried out to understand the performance of particle breakage methods, which are Bonded Particle Model (BPM), Fast Breakage Model (FBM) and Particle Replacement Model (PRM), in the modeling of comminution equipment. In addition, the relationship between particle and breakage energies and theory of applied forces are described in detail for three breakage models existing in commercial DEM simulators

Keywords: Bonded Particle Model, DEM, , Fast Breakage Model, Particle Breakage, Particle Replacement Method.

Introduction

In industrial scale processing operations, size reduction is carried out by crusher and tumbling mills with rod/ball-autogenous/semi-autogenous grinding technologies. In plants, energy consumption during the grinding stage can be up to 80-90% of total energy consumption (Jeswiet and Szekeres, 2016). Modeling studies are carried out to reduce energy consumption in grinding. It has been proven that modeling size reduction processes with Discrete Element Method (DEM) are a useful technique for predicting wear, particle breakage and particle size distribution in addition to energy consumption.

The DEM was first proposed by Cundall and Strack (1979) as a numerical model to define the mechanical behavior of spheres or discs. The use of this method has become increasingly widespread in processes such as rock mechanics, crushing and grinding, which can be expressed in terms of granular materials, with the idea that particle motions explain the motion of the whole mass. In granular media, particles that move independently from each other and interact only at their contact points affect the behavior of the media. In granular media, DEM utilizes Newton's laws of motion for the motion of individual particles and contact laws for the contact between particles (Weerasekara et al., 2013).

In DEM, the motion of the particles is found by a series of calculations that follow the contact forces and the displacement of the particles during the collision. First, it is verified whether the particles are in contact with each other for particles i and j with radius R_i and R_j, respectively;

$$R_i + R_j > D \tag{1}$$

Where, D is the distance between the centers of the two particles. A spring and dashpot pair mechanism is assumed at each contact point. These pairs form the normal and tangential force components. In the tangential direction, there is also a sliding mechanism (Figure 1) (Cundall and Strack, 1979). Of these components, the Hertz model (Hertz, 1982) represents for the normal force component and the Mindlin model (Mindlin, 1949) for the tangential force component. Normal force;

*Corresponding author: sevgi.karaca@dpu.edu.tr • https://orcid.org/0000-0001-7478-2437
** ali.ucar@dpu.edu.tr • https://orcid.org/0000-0002-5220-8829

$$F_n = -k_n \Delta x + C_n v_n \tag{2}$$

where Δx is amount of overlap, k_n is the stiffness in the normal direction and C_n is the normal damping coefficient. $k_n \Delta x$ is the spring mechanism and $C_n v_n$ is the dashpot mechanism. The C_n value is derived from the coefficient restitution (ε), which is the ratio of the particle velocities before and after the collision (Cleary, 1998).
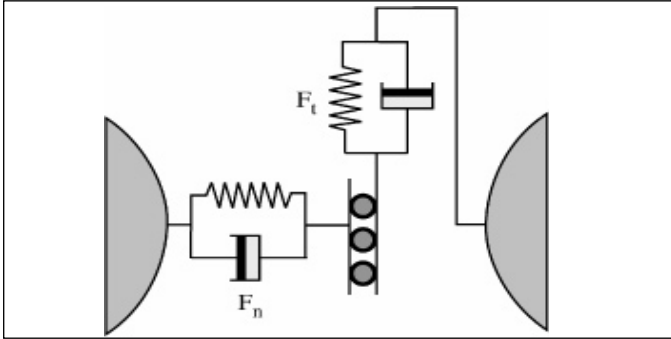

Figure 1. Contact forces between two particles in contact (Cleary, 2001a)

The tangential force is given by;

$$F_t = min(\mu F_n, k_t \int v_t dt + C_t v_t) \tag{3}$$

where μ is the friction coefficient, k_t is the stiffness in the tangential direction and C_t is the tangential damping coefficient. The total tangential force is restricted by the Coulomb frictional limit, above which the surface contact shears and the particles begin to slide over each other. (Cleary, 1998).

The simulation step in DEM consists of particle creation, contact of the particles with each other and with the geometry, and a series of time steps that depend on their position. After each time step, the position and contacts of the particles and geometry are updated. This process continues until all time steps are completed (Figure 2) (EDEM, 2023).
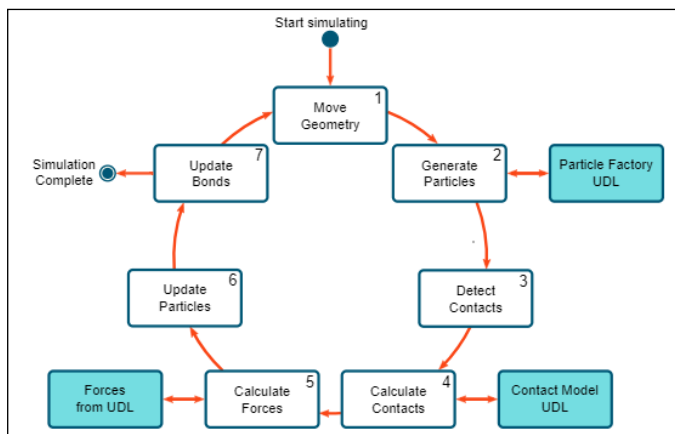

Figure 2. EDEM's simulation sequence

DEM was first used in mineral processing to model various mills with the assumption that particle motions explain the motion of the whole mass. Firstly, Mishra and Rajamani (1992) and Mishra and Rajamani (1994) used DEM to predict the media motion in ball mills in 2D. After that, Rajamani and Mishra (1996) also used DEM to describe particle motion in 2D semi-autogenous mills. As the application of DEM in 3D increases the accuracy of predictions, the use of DEM in different types of mills has increased significantly (Bian et al., 2017; Cleary, 1998; Cleary, 2001a; Cleary, 2001b; Cleary et al., 2003; Cleary, 2015; Datta and Rajamani, 2002; Djordjevic, 2005; Herbst and Nordell, 2001; Jayasundara et al., 2012; Morrison et al., 2009; Powell et al., 2011; Wang et al., 2012).

In modeling crushers with DEM; many researchers have studied it to define cone crushers (Delaney et al., 2015; Lichter et al., 2009; Quist and Evertsson, 2016), pressure crushers (Cleary and Sinnott, 2015; Refahi et al., 2010) and HPGR (Barrios and Tavares, 2016). The particle breakage mechanism of different types of crushers is also different. For the use of DEM in crushers, particle breakage is required to be included in the model. There are main three methods used by commercial software to simulate particle breakage in DEM: Bonded-Particle Model (BPM), Fast Breakage Model (FBM) and Particle Replacement Model (PRM). In the present work, the theory of these three models describing particle breakage were investigated in detail. According to the results of the investigation, the applicability of these models in comminution processes was determined.

1. Particle breakage models

1.1. Bonded Particle Model (BPM)

The BPM developed by Potyondy and Cundall (2004) aimed to simulate the mechanical behavior of rock by representing it as a cemented granular material. A system is developed with non-uniformly sized spherical particles connected to each other at the contact points. The mechanical behavior of this system is described by the motion of each particle and the force and moment acting at each contact. The interconnected particles are called fraction particles and the resulting cluster is called meta particles. In this study, they proposed a numerical model represented by a packing of dense spherical or circular particles that are tightly bonded together at the contact points and whose mechanical behavior is simulated by DEM using the two- and three-dimensional discontinuous programs PFC2D and PFC3D. Breakage was presented by broken bonds. It was found that particle size has a significant effect on the breaking strength of a material. In addition, similar results were obtained for their mechanical behavior.

A critical part of BPM is the determination of the size of the spheres that form the meta particle, also referred to as the parent particle. These include normal distributions (Antonyuk et al., 2006), mono size (Metzger and Glasser, 2012) and bi-modal (Quist and Evertsson, 2016) distributions (Figure 3).
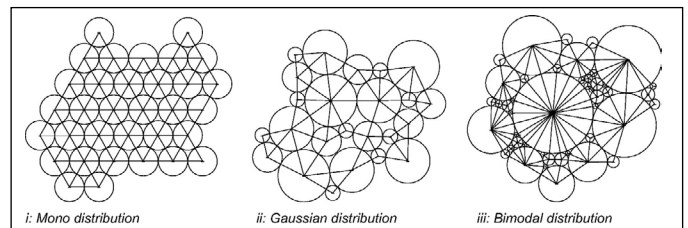

i: Mono distribution   *ii: Gaussian distribution*   *iii: Bimodal distribution*

Figure 3. Schematic presentation of three types of packaging structures (Quist and Evertsson, 2016)
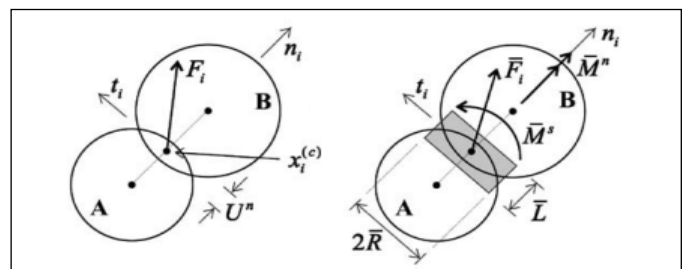

Figure 4. Illustration of BPM forces and moments (Potondy and Cundall, 2004)

Figure 4 shows, $F_{n,b}$, $F_{t,b}$ and M_{bn}, M_{bt} are the axial (normal) force and shear force and moments, respectively;

$$\delta F_{t,b} = -k_b^t A \Delta U_t$$
$$\delta M_b^n = -k_b^t J \Delta \theta_n \qquad (4)$$
$$\delta M_b^t = -k_b^n I \Delta \theta_t$$

where;

$$\Delta U_n = v_n \delta_t$$
$$\Delta U_t = v_t \delta_t$$
$$\Delta \theta_n = w_n \delta_t \qquad (5)$$
$$\Delta \theta_t = w_t \delta_t$$

where; k_{bn} and k_{bt} normal and shear bond stiffness. v_n, v_t, w_n and w_t are normal and tangential velocities and normal and tangential angular velocities, respectively. A, I and J are an area of the parallel bond cross section, moment of inertia and polar moment of inertia.

$$A = \pi R_b^2$$
$$I = \frac{1}{4}\pi R_b^4 \qquad (6)$$
$$J = \frac{1}{2}\pi R_b^4$$

Maximum tensile (σ_{max}) and shear stresses (τ_{max});

$$\sigma_{max} = \frac{F_{n,b,toplam}}{A} + \frac{2M_b^n}{J} R_b$$
$$\tau_{max} = \frac{F_{t,b,toplam}}{A} + \frac{2M_b^t}{J} R_b \qquad (7)$$

The maximum tensile stress exceeds the tensile strength (σ_c) or the maximum shear stress exceeds the shear strength (τ_c), the parallel bond is broken and the associated forces, moments and stiffeners are removed from the model (Potyondy and Cundall, 2004).

BPM has been used to model vertical roller mill (Liu et al., 2022), ball mill (Metzger and Glasser, 2013), cone crusher (Quist and Evertsson, 2016), gyratory crusher (Quist et al., 2011) in mineral processing by using DEM.

Quist and Evertsson (2016) simulated an industrial size cone crusher with a BPM with a bimodal particle distribution. They verified the simulation results with single particle breakage experiments. They determined that throughput, power, pressure and particle size distribution can be predicted using the BPM. Unfortunately, this process increases the computational workload considerably. The results are obtained in accordance with the results of the analytical models developed by Evertsson (2000).

1.2. Fast Breakage Model (FBM)

Potapov and Campbell (1996) proposed a model including polyhedral particles, called FBM. The paper described the extension of the existing two-dimensional technique to three dimensions in order to simulate the breakage of brittle solids. In this way, a fault can spread uniformly through the simulated material. The breakage occurred on a simulated particle formed by gluing polyhedral particles together with bonds between fitting parts. FBM is an instantaneous breakage model that utilizes Laguerre-Voronoi tesselation to break the particle into 2D polygonal or 3D polyhedral at the initial moment when the total energy of the collision is greater than the energy required for breakage (Jiménez-Herrera et al., 2018) (Figure 5).

The FBM has been used to describe breakage in the particle bed (Paluszny et al., 2016; Potapov and Campbell, 2000) and to simulate comminution equipment (Herbst and Potapov, 2004; Lichter et al., 2009). In comparing this model with two other breakage models, Jiménez-Herrera et al. (2018) reported that the FBM describes the interaction between the particle bed and the dropping ball very well, but is limited in describing the particle size distribution as well as the measured force deformation caused by single particle breakage. Moreover, mass conservation and the possibility of generating irregularly shaped particles have made the FBM a potentially powerful model for simulating large-scale communication systems (Jiménez-Herrera et al., 2018).

Lichter et al. (2009) simulated different cone crushers utilizing DEM's FBM breakage model to determine the flow rate, energy consumption and particle size distribution of the product. The approach, referred to currently as FBM, combines DEM components with Population Balance Modeling (PBM) components. The PBM method used 3D polyhedral particles. The contact energy of the particle is sufficient to break the particle and the particle is instantly broken into smaller sizes, the size distribution of which is calculated by PBM. According to the results of the study, the outputs were obtained in agreement with the experimental data (Figure 6).
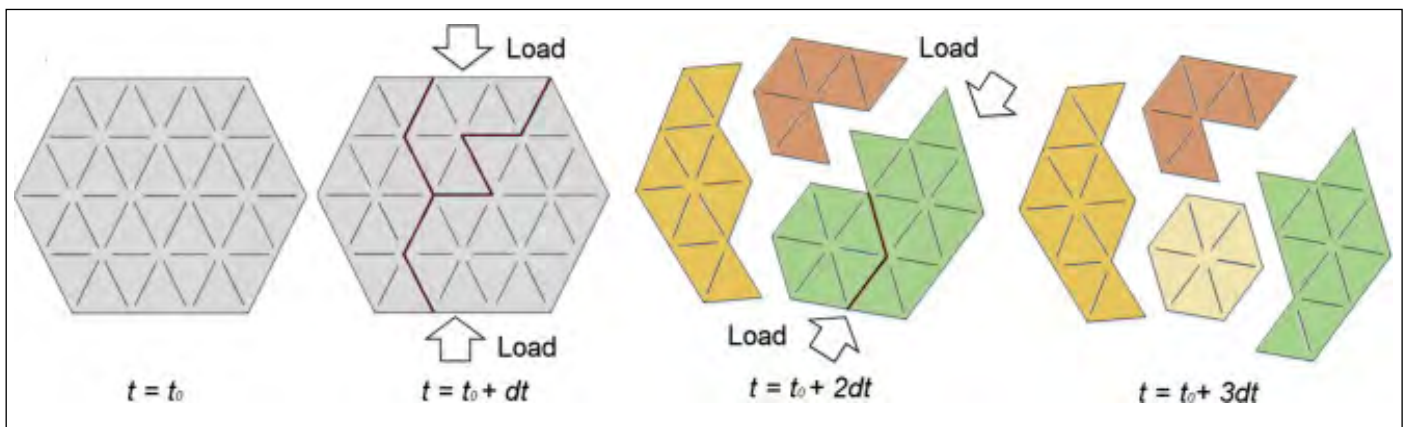

Figure 5. 2D illustration of particle breakage in FBM (shows multiple breakage phenomena) (Jiménez-Herrera et al., 2018)
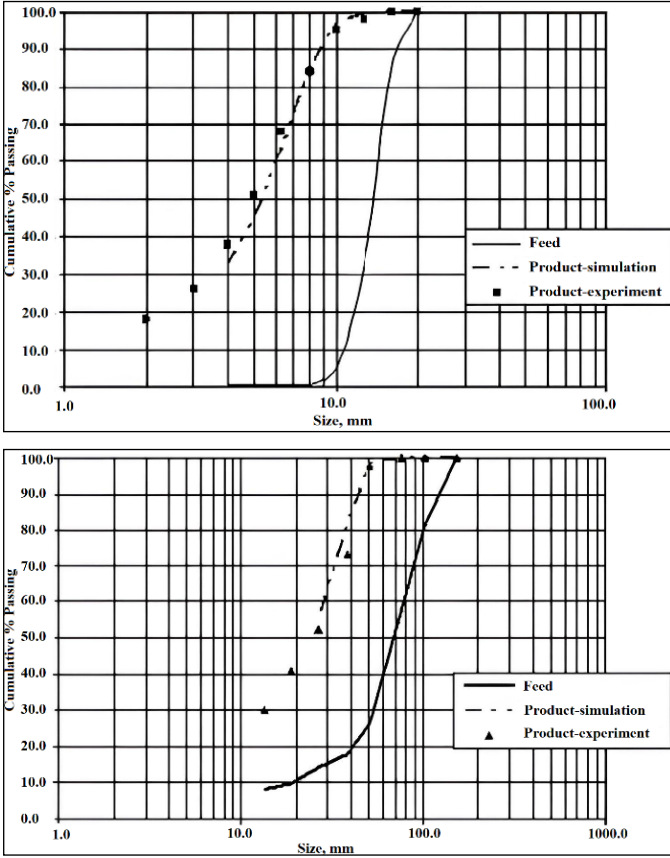
Figure 6. Simulated and experimental particle size distributions - HP100 Model (Right), B90 Model (Left) (Lichter et al., 2009)

The Vogel and Peukert model is based on a generalized dimensional analysis approach proposed by Rumpf (1973) and a detailed breakage mechanics model based on Weibull statistics (1951). The breakage probability P(E) is expressed in Equation 8 by combining these two different approaches in the Vogel and Peukert model (Vogel and Peukert, 2005).

$$P(E) = 1 - \exp\left[-S\left(\frac{d_i}{d_{i,ref}}\right)E_{cum}\right] \tag{8}$$

$$E_{cum} = E'_{cum} + E - E_{min}$$
$$E_{min} = e_{min,ref}\left(\frac{d_{i,ref}}{d_i}\right) \tag{9}$$

where E'_{cum} is the energy deposited in the grain just before the moment of stress, E is the total specific energy of the collision in an impact event. S, $d_{i,ref}$, $e_{min,ref}$ and d_i are the model parameters that define the breaking strength of the material, the reference size, the minimum energy required to break this reference size and the particle size, respectively.

1.3. Particle Replacement Model (PRM)

First proposed by Cleary (2001a and 2001b) to describe particle breakage in DEM, PRM is an instantaneous (over a period of time) replacement of particles with smaller sized progeny when the particles achieve the breakage requirement. Using PRM, the product size can be defined and a target size distribution can be obtained. Several studies have been conducted in which the particle can be a sphere or cluster sphere (Åström and Herrman, 1998; Barrios et al., 2020; Cleary, 2001b; Cleary and Sinnott, 2015; Tava-

res et al., 2021), superquadric (Delaney et al., 2015) or polyhedral cell (Arruda Tino and Tavares, 2022; Chen et al., 2024; Tavares et al., 2020) and is replaced by smaller particles of the same or different shape by breakage.

PRM is implemented in the Tavares UFRJ Fracture Model, which is available as a breakage model in Altair EDEM. In the model, the main condition for a particle to break and be replaced by its fragments is that the specific impact energy must be higher than the specific breaking energy of the particle. In Figure7, each parent particle is removed from the simulation when breakage occurs and replaced by a group of smaller sized particles. The majority of PRM utilizes spheres as the replacement particles for computational efficiency. The main drawback, however, is the mass loss that occurs when a large sphere is replaced by several smaller spheres. To obtain a breakage result close to a real breakage result, the spheres inside the parent particle are organized so that the largest spheres overlap in the direction perpendicular to the stress that caused the breakage. The remaining smaller spheres are then arranged in the remaining spaces, usually overlapping with the larger spheres. During replacement, the spheres are initially allowed to overlap in order to fill the volume of the original parent particle. But this overlap can be significant sufficient to lead to large artificial repulsive forces between them. A further reason for the unrealistic results of the simulation is mass loss (Jiménez-Herrera et al., 2018; Tavares and Chagas, 2021; Tavares et al., 2021).
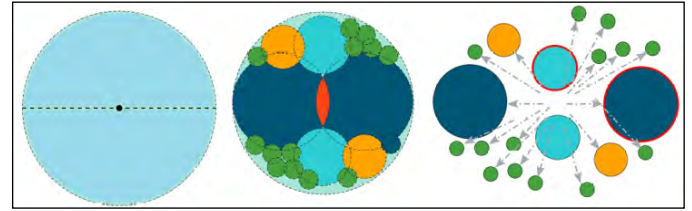

Figure 7. Schematic presentation of PRM; (a) main particle (b) particle replacement by size distribution (c) image after applying force (EDEM, 2023)

The potential explosions between the spheres are controlled by applying a dumping approach to limit the total contact force applied to each sphere (global damping strength) and also the time for which the reduced force is applied (global dumping time). Thus, part of the overlap can be defined in such a way that part of the breakage energy is released back into the particles (local damping strength). This method provides the possibility to control the kinematics of the particles and prevents the appearance of excessively high velocities of the particles, which would make the simulations unrealistic. In addition, in order to eliminate mass loss and provide accurate size distributions when generating realistic simulations, a size class called dummy particles is created, which defines particles up to 1/5 of the main size. Particles in this dummy size class are not allowed to break (EDEM, 2023).

The size, average value and standard deviation of each particle are assigned a specific breakage energy. This energy is determined according to the distribution given by Tavares and King (2002).

$$P(E) = \frac{1}{2}\left[1 + erf\frac{lnE^* - lnE_{50}}{\sqrt{2}\sigma}\right] \tag{10}$$

$$E^* = \frac{E_{max}E}{E_{max} - E} \tag{11}$$

where P(E) is the probability of breakage or cumulative distribution, E is the particle breakage energy distribution corresponding to the maximum stress energy it can endure in a collision, E_{max} is the upper cut-off value of the distribution, and E_{50} and σ are the median and standard deviation of the distribution, respectively.

The upper cut-off value is usually represented by the ratio E_{max}/E_{50}. When this ratio is equal to infinity, $E^* = E$ and Equation 10 becomes the lognormal distribution. Another parameter that affects the breakage probability is the particle size. The relationship between particle size and average breakage energy (Tavares and King, 1998; Tavares, 2022);

$$E_{50,i} = \frac{E_\infty}{1+k_p/k_s}\left[1 + \left(\frac{d_o}{d_i}\right)^\varphi\right]$$ (12)

where E_∞, d_0 and ϕ are model parameters to be determined by experimental data and d_i is the representative size of particles in size class i. k_p is the particle stiffness, k_s is the Hertzian stiffness of the surface in contact with the particle. The stiffness of a particle is significantly smaller than the stiffness of the surface of the testing machine or equipment in contact with the particle. In some cases, however, this is not the case, so a correction must be used. The strain energy, e, involved in an event used to deform the particle is given by (Tavares, 2022).

$$e = \frac{1}{1+k_p/k_s}$$ (13)

e is expressed as the ratio of the energy involved in a collision and distributed to the particles according to their stiffness. In the case of two particles of the same material in collision, Equation 13 gives e=0.5, since the energy is shared equally between them.

In a collision, when the specific strain energy is smaller than the breakage energy of the particle, the particle would not break, but would maintain internal fault-like damage that would make it more fracture prone in a future tensile phenomenon. This damage is described on the basis of a model based on continuous damage mechanics in which the specific breakage energy of the particle is reduced (Figure 8) (Tavares and King, 2002; Tavares, 2009);

$$E' = E(1 - D)$$ (14)

$$D = \left[\frac{2\gamma}{(2\gamma-5D+5)}\frac{eE_k}{E}\right]^{\frac{2\gamma}{5}}$$ (15)

where E′ is the breakage energy of the particle after the collision phenomena, D is the damage exposed to the particle after a contact that does not lead to breakage. e′ is the specific energy involved in the additional collision (or effective impact energy) and γ is the damage accumulation coefficient, which characterizes the damage tolerance of a material before breakage. Equation 15 can be calculated iteratively, starting with D = 0.
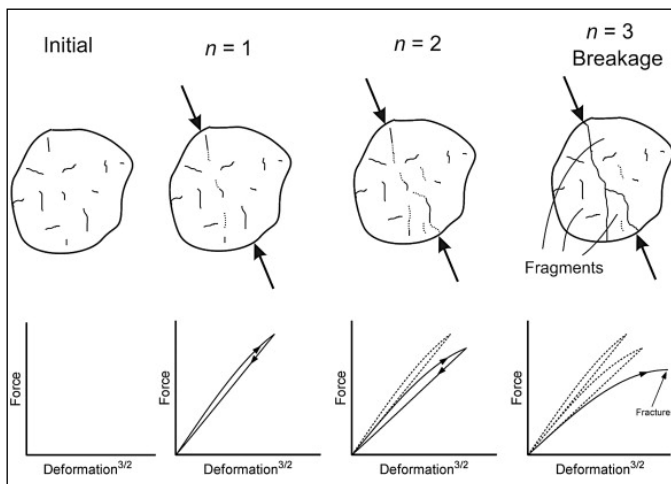

*Figure 8. Illustration of the failure effect of particles caused by damage accumulation during repeated loading phenomena (*Tavares, 2009)

The breakage level of particles can be expressed by a single parameter, t_{10}, which represents the ratio of particles finer than 1/10 of the parent particle size (Napier-Munn et al., 1996). Tavares (2009) stated the relationship between the specific tensile energy and the average breakage energy of particles in Equation 16.

$$t_{10} = A\left[1 - \exp\left(-b'\frac{eE_k}{E_{50b}}\right)\right]$$ (16)

where A and b′ are the model parameters obtained from the single particle breakage data and E_{50b} is the median breakage energy of the broken particles. In the case of the primary breakage function, where the ratio eE_k/E_{50b} can be assumed to be equal to one, Eq. 16;

$$t_{10} = A[1 - \exp(-b')]$$ (17)

The total particle size distribution is;

$$t_n(t_{10}) = \frac{100}{\int_0^1 x^{\alpha_n-1}(1-x)^{\beta_n-1}dx}\int_0^{t_{10}/100} x^{\alpha_n-1}(1-x)^{\beta_n-1}dx$$ (18)

where x is the cumulative mass (t_n) of the particles passing through the sieve of the corresponding size, calculated from the given distribution value t_{10}, α_n and β_n are the parameters of the model for the chosen values of t_n.

PRM has been studied to simulate particle bed breakage and single particle breakage processes (Arruda Tino and Tavares, 2022; Barrios et al., 2015; Barrios et al., 2020; Jiménez-Herrera et al., 2018; Tavares et al., 2020; Tavares et al., 2021; Tavares and Chagas, 2021).

Tavares and Chagas (2021) described the simulation of particle breakage using DEM and proposed a stochastic-randomized approach to produce realistic size distributions. In the study, a family of spherical particles for various values of t_{10} was created to represent the breakage of spherical particles simulated using DEM, based on data obtained from weight reduction tests. It is emphasized that the proposed model is successful in simulating the breakage of particles and is successful to generate real size distributions. A similar study was performed by Tavares et al. (2021) in the updated version of EDEM and again showed a strong performance in predicting particle breakage. In addition to these studies using EDEM, Tavares et al. (2020) and Arruda Tino and Tavares (2022) simulated particle breakage using polyhedral particles instead of spherical particles using Rocky DEM commercial software.

Arruda Tino and Tavares (2022) showed in their study that the results of the JK drop weight test, Los Angeles abrasion test and Bond breakage tests can be predicted by simulating them with DEM using polyhedral particles and Voronoi tessellation in the PRM. Comparison of experimental JK drop weight test results with its simulations revealed that the simulation is sensitive to the variables. It was found that there was good agreement for copper ore and granulite, but deviation for limestone. Considering the predictions of the breakage amenability parameter A*b, it overestimated the experimentally obtained values.

Tavares et al. (2020) reported that their model was able to accurately predict the breakage probability and particle size distribution for single and multiple impact cases. The simulation results were also analyzed for sensitivity to the coefficient restitution and it was observed that the contact parameter had a limited effect on the simulation results. It was also shown that as the number of layers increases, the amount of broken material is reduced in hard copper ore and the amount of broken material is increased in soft limestone.

Barrios et al. (2020) simulated particle breakage with a replacement model implemented in the EDEM commercial software. The model predicted some parameters based on single particle breakage tests on iron ore pellets. The predictions of the model were compared with results of experiments and showed agreement both in terms of the breakage probability and the particle size distribution obtained as a result of compression and impact. Figure 9 shows the results of experiments and simulations for the collision of a 3-layer particle bed with an 88 mm steel ball having an impact energy of 10 J. Figure 9 illustrates the generation of new particles as well as the expulsion of particles. The color in the images of simulations indicates the velocity at which the particles are thrown. The times are displayed in terms of t = 0, corresponding to the moment of contact of the dropped ball with the top of the particle bed.
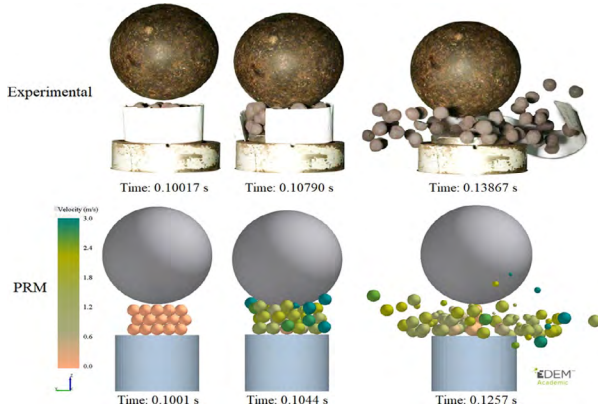

Figure 9. Comparison of snapshots of the experiment and DEM simulation of unconfined particle bed impact tests using Impact load cell (Barrios et al., 2020)

Jiménez-Herrera et al. (2018) compared three different particle breakage models in the commercial DEM simulators for modeling the particle bed. It was found that BPM is ideal because it can describe the force-deformation profile and the interaction with the ball dropped on the bed particles, but it cannot represent the material breakage distribution. FBM and PRM, on the other hand, could not adequately describe the force-deformation profile. The model patterns of BPM, PRM and FBM before, during and after single particle breakage simulation were analyzed and the results of the particle breakage simulation are shown in Figure 10. At BPM, the progression of breakage is apparent, following the breaks of the bonds. In the FBM plot, both the first breakage of the main particle and the following breakage of the progeny particles are shown, revealing the irregular shape of the particles. Figure 10 also shows two different moments after a particle reached the critical load for breakage in the PRM plot, revealing the very strong overlap that should be allowed in this model instantly after breakage.
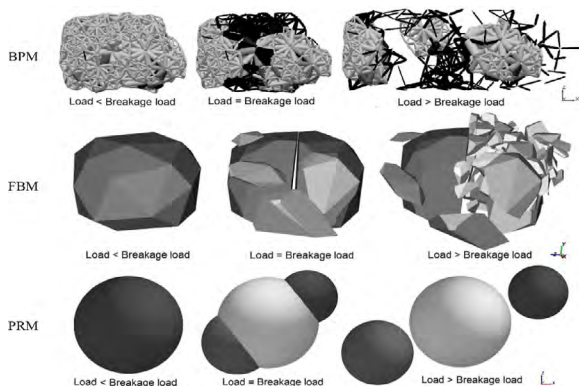

Figure 10. Schematic comparison of breakage models (Jiménez-Herrera et al., 2018)

There are some studies using PRM to model different comminution equipment such as HPGR (Barrios and Tavares, 2016; Rodriguez et al., 2021), cone crushers (Delaney et al., 2015), compression crushers (Cleary and Sinnott, 2015).

Cleary and Sinnott (2015) simulated the flow and breakage of material as it passes through the breakage chamber using the PRM breakage model of the DEM proposed by Cleary (2001a and 2001b) to study jaw, cone, gyratory, impact and double roll crushers. Using PFC3D software, energy, particle size, throughput and wear were estimated for the crushers. Figure 11 shows the breakage model of the collision of two high-velocity particles in 3D. The main particles in Figure 11a collide and distribute enough energy in the normal direction to break and then are replaced by the small particles in Figure 11b. These particles can then move independently (Figure 11c) and interact with other particles and the boundaries of the crusher, possibly breaking again if conditions are favorable.
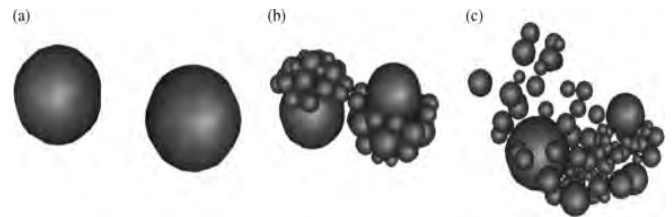

Figure 11. Schematic comparison of breakage models (Cleary and Sinnott, 2015)

Delaney et al. (2015) determined the flow and breakage process in an industrial cone crusher with the PRM breakage model using non-spherical particles. In the simulations, the model was developed using non-spherical particles known as superquadrics instead of spheres to improve reality, but this resulted in computational limitations. The study simulated the performance of the cone crusher and predicted particle size distribution, throughput, energy consumption and liner wear. The wear distribution is affected by the stress distribution and flow pattern and is different in the mantle and concave section. The wear is highest at the location of the plug point of the crusher.

3. Conclusion

This work is summarized the studies have been carried out to understand the performance of particle breakage methods in the modeling of comminution equipment. In addition, the relationship between particle and breakage energies and theory of applied forces are described in detail for three breakage models existing in commercial DEM simulators. Each model has advantages and disadvantages and a general summary is presented below.

In the Bonded Particle Model (BPM), non-uniform particle, called meta-particles, are formed by connecting each other at the contact points and the problem of mass conservation is eliminated by high packing density. This method, is based on particle flow dynamics. Realistic results are obtained in simulation processes, but it requires high computational effort and is not suitable for a large number of particles. However, it describes the force-deformation profile well.

Fast Breakage Model (FBM) is an instantaneous breakage model that uses Laguerre-Voronoi tessellation to breakage polyhedral particles. This model produces irregular shapes particles and provides mass conservation. It is not suitable for particle size distribution estimation and requires high computation effort. Unlike BPM, it does not describe the force-deformation profile well.

Simulating breakage with Particle Replacement Model (PRM) is based on the replacement of the parent particle by progeny particles when a load is applied. In order to obtain close to realistic results, the particles are placed on top of each other to ensure mass conservation while placing the particles that will result from the breakage processes in the main particle volume. However, this high overlap causes artificial repulsion forces. This is controlled by a damping approach. It also uses dummy particles to ensure mass conservation. It is suitable for simulations with a large number of particles. It does not describe the breakage probability and force-deformation profile well.

In summary, three methods provide mass conservation by applying different methods. PRM offers faster results than other methods when using a large number of particles. However, the model that best describes the force-deformation profile is BPM.

Acknowledgement

References

Antonyuk, S., Khanal, M., Tomas, J., Heinrich, S., Mörl, L. 2006. Impact breakage of spherical granules: experimental study and DEM simulation. Chemical Engineering and Processing: Process Intensification. 45(10), 838-856.

Åström, J.A., Herrmann, H.J. 1998. Fragmentation of grains in a two-dimensional packing. The European Physical Journal B-Condensed Matter and Complex Systems. 5(3), 551-554.

Barrios, G.K.P., Pérez-Prim, J., Tavares, L.M. 2015. DEM simulation of bed particle compression using the particle replacement model. In Proceedings 14th European Symposium on Comminution and Classification.

Barrios, G.K., Tavares, L. M. 2016. A preliminary model of high pressure roll grinding using the discrete element method and multi-body dynamics coupling. International Journal of Mineral Processing. 156, 32-42.

Barrios, G.K., Jiménez-Herrera, N., Tavares, L.M. 2020. Simulation of particle bed breakage by slow compression and impact using a DEM particle replacement model. Advanced Powder Technology. 31(7), 2749-2758.

Bian, X., Wang, G., Wang, H., Wang, S., Lv, W. 2017. Effect of lifters and mill speed on particle behaviour, torque, and power consumption of a tumbling ball mill: Experimental study and DEM simulation. Minerals Engineering. 105, 22-35.

Chen, F., Ma, H., Liu, Z., Zhou, L., Zhao, Y. (2024). An improved breakage model with a fast-cutting method for simulating the breakage of polyhedral particles. Powder Technology, 432, 119125.

Cleary, P.W. 1998. Predicting charge motion, power draw, segregation and wear in ball mills using discrete element methods. Minerals Engineering. 11(11), 1061-1080.

Cleary, P.W 2001a. Modelling comminution devices using DEM. International Journal for Numerical and Analytical Methods in Geomechanics. 25(1), 83-105.

Cleary, P.W. 2001b. Recent advances in DEM modelling of tumbling mills. Minerals Engineering. 14(10), 1295-1319.

Cleary, P.W., Morrisson, R., Morrell, S. 2003. Comparison of DEM and experiment for a scale model SAG mill. International Journal of Mineral Processing. 68(1-4), 129-165.

Cleary, P.W. 2015. Prediction of coupled particle and fluid flows using DEM and SPH. Minerals Engineering. 73, 85-99.

Cleary, P.W., Sinnott, M.D. 2015. Simulation of particle flows and breakage in crushers using DEM: Part 1–Compression crushers. Minerals Engineering. 74, 178-197.

Cundall, P.A., O.D.L. Strack, 1979. A discrete numerical model for granular assemblies. Geotechnique. 29(1), 47-65.

Datta, A., Rajamani, R.K. 2002. A direct approach of modeling batch grinding in ball mills using population balance principles and impact energy distribution. International Journal of Mineral Processing. 64(4), 181-200.

de Arruda Tino, A.A., Tavares, L.M. 2022. Simulating breakage tests using the discrete element method with polyhedral particles. Computational Particle Mechanics. 1-13.

Delaney, G.W., Morrison, R.D., Sinnott, M.D., Cummins, S., Cleary, P.W. 2015. DEM modelling of non-spherical particle breakage and flow in an industrial scale cone crusher. Minerals Engineering. 74, 112-122.

EDEM DEM Solutions. 2023. EDEM Programming Guide.

Djordjevic, N. 2005. Influence of charge size distribution on net-power draw of tumbling mill based on DEM modelling. Minerals Engineering. 18(3), 375-378.

Herbst, J.A., Nordell, L. 2001. Optimization of the design of sag mill internals using high fidelity simulation. In Proceedings of the SAG Conference 4, 50-164. University of British Columbia: British Columbia.

Herbst, J.A., Potapov, A.V. 2004. Making a discrete grain breakage model practical for comminution equipment performance simulation. Powder Technology. 143, 144-150.

Hertz, H. 1882. On the contact of elastic solids. Journal fur die Reine und Angewandte Mathematik. 92, 156-171.

Jayasundara, C.T., Yang, R.Y., Yu, A.B. 2012. Effect of the size of media on grinding performance in stirred mills. Minerals Engineering. 33, 66-71.

Jeswiet, J., Szekeres, A. 2016. Energy Consumption in Mining Comminution. Procedia CIRP. 48, 140-145.

Jiménez-Herrera, N., Barrios, G.K., Tavares, L.M. 2018. Comparison of breakage models in DEM in simulating impact on particle beds. Advanced Powder Technology. 29(3), 692-706.

Lichter, J., Lim, K., Potapov, A., Kaja, D. 2009. New developments in cone crusher performance optimization. Minerals Engineering. 22(7-8), 613-617.

Liu, C., Chen, Z., Zhang, W., Mao, Y., Xu, P., Xie, Q. 2022. Analysis of vertical roller mill performance with changes in material properties and operating conditions using DEM. Minerals Engineering. 182, 107573.

Metzger, M.J., Glasser, B.J. 2012. Numerical investigation of the breakage of bonded agglomerates during impact. Powder Technology. 217, 304-314.

Metzger, M.J., Glasser, B.J. 2013. Simulation of the breakage of bonded agglomerates in a ball mill. Powder Technology. 237, 286-302.

Mindlin, R.D. 1949. Compliance Of Elastic Bodies In Contact. Journal of Applied Mechanics. 16, 259-268.

Mishra, B.K., Rajamani, R.K. 1992. The discrete element method for the simulation of ball mills. Applied Mathematical Modelling. 16(11), 598-604.

Mishra, B.K., Rajamani, R.K. 1994. Simulation of charge motion in ball mills. Part 1: experimental verifications. International Journal of Mineral Processing. 40(3-4), 171-186.

Morrison, R.D., Cleary, P.W., Sinnott, M.D. 2009. Using DEM to compare the energy efficiency of pilot scale ball and tower mills. Minerals Engineering. 22(7-8), 665-672.

Napier-Munn, T.J., Morrell, S., Morrison, R.D., Kojovic, T. 1996. Mineral comminution circuits: their operation and optimisation. Julius Kruttschnitt Mineral Research Centre, University of Queensland, Brisbane.

Paluszny, A., Tang, X., Nejati, M., Zimmerman, R.W. 2016. A direct fragmentation method with Weibull function distribution of sizes based on fi-

nite-and discrete element simulations. International Journal of Solids and Structures. 80, 38-51.

Potapov, A.V., Campbell, C.S. 1996. A three-dimensional simulation of brittle solid fracture. International Journal of Modern Physics C. 7(05), 717-729.

Potapov, A.V., Campbell, C.S. 2000. The breakage induced by a single grinding ball dropped onto a randomly packed particle bed. Powder Technology. 107(1-2), 108-117.

Potyondy, D.O., Cundall, P.A. 2004. A bonded-particle model for rock. International Journal of Rock Mechanics and Mining Sciences. 41(8), 1329-1364.

Powell, M.S., Weerasekara, N.S., Cole, S., LaRoche, R.D., Favier, J. 2011. DEM modelling of liner evolution and its influence on grinding rate in ball mills. Minerals Engineering. 24(3-4), 341-351.

Quist, J., Evertsson, C. M., Franke, J. 2011. The effect of liner wear on gyratory crushing–a DEM case study. Computational Modeling, 11.

Quist, J., Evertsson, C.M. 2016. Cone crusher modelling and simulation using DEM. Minerals Engineering. 85, 92-105.

Rajamani, R. K., Mishra, B. K. (1996). Dynamics of ball and rock charge in sag mills. In Proc. SAG (Vol. 19).

Refahi, A., Mohandesi, J. A., Rezai, B. (2010). Discrete element modeling for predicting breakage behavior and fracture energy of a single particle in a jaw crusher. International Journal of Mineral Processing, 94(1-2), 83-91.

Rumpf, H. 1973. Physical aspects of comminution and new formulation of a law of comminution. Powder Technology. 7(3), 145-159.

Rodriguez, V.A., Barrios, G.K., Bueno, G., Tavares, L.M. 2021. Investigation of lateral confinement, roller aspect ratio and wear condition on HPGR performance using DEM-MBD-PRM simulations. Minerals. 11(8), 801.

Tavares, L.M., King, R.P. 1998. Single-particle fracture under impact loading. International Journal of Mineral Processing. 54(1), 1-28.

Tavares, L.M., King, R.P. 2002. Modeling of particle fracture by repeated impacts using continuum damage mechanics. Powder Technology. 123(2-3), 138-146.

Tavares, L.M. 2009. Analysis of particle fracture by repeated stressing as damage accumulation. Powder Technology. 190(3), 327-339.

Tavares, L.M., André, F.P., Potapov, A., Maliska Jr,C. 2020. Adapting a breakage model to discrete elements using polyhedral particles. Powder Technology. 362, 208-220.

Tavares, L.M., das Chagas, A.S. 2021. A stochastic particle replacement strategy for simulating breakage in DEM. Powder Technology. 377, 222-232.

Tavares, L.M., Rodriguez, V.A., Sousani, M., Padros, C.B., Ooi, J.Y. 2021. An effective sphere-based model for breakage simulation in DEM. Powder Technology. 392, 473-488.

Tavares, L.M. 2022. Review and further validation of a practical single-particle breakage model. KONA Powder and Particle Journal. 39, 62-83.

Vogel, L., Peukert, W. 2005. From single particle impact behaviour to modelling of impact mills. Chemical Engineering Science. 60(18), 5164-5176.

Wang, M.H., Yang, R.Y., Yu, A.B. 2012. DEM investigation of energy distribution and particle breakage in tumbling ball mills. Powder Technology. 223, 83-91.

Weerasekara, N.S., Powell, M.S., Cleary, P.W., Tavares, L.M., Evertsson, M., Morrison, R.D., Ouist, J., Carvalho, R.M. 2013. The contribution of DEM to the science of comminution. Powder technology. 248, 3-24.

Weibull, W. 1951. A statistical distribution function of wide applicability. Journal of Applied Mechanics.

BİLİMSEL MADENCİLİK DERGİSİ
SCIENTIFIC MINING JOURNAL

Original Research

Cyanidation of Tailings of an Artisanal Small-Scale Gold Mining at Arbaat Region in Red Sea State, Sudan

Babiker Ali Alkloos[a,*] Salih Aydoğan[b,**]

[a] Department of Mining and Economic Geology, Faculty of Earth Sciences, Red Sea University, Port Sudan, Sudan.
[b] Department of Mining Engineering, Faculty of Engineering and Natural Sciences, Konya Technical University, 42250, Konya, Türkiye.

A B S T R A C T

In this study, the leaching of gold from an artisanal small-scale gold mining (ASGM) tailings in the Arbaat region of Sudan was investigated by agitated cyanide leaching, considering the parameters stirring speed, NaCN concentration, solid-liquid ratio, temperature and pH. The characterization studies showed that the tailings sample mainly formed from silicate minerals and the sample contained 77.10% SiO2, 8.08% Al2O3, 5.76% Fe2O3, 1.67% CaO, 1.10% Na2O, 0.97% K2O and 4.366% loss on ignition. The results of leaching studies indicated that gold dissolution decreases with increasing solid ratio. Furthermore, the gold leaching positively influenced by the NaCN concentration in the range of 0.05-0.50 g/L and by the pH in the range of 10.00-10.30. However, at pH values greater than 10.30, the gold leaching decreased. The temperature and stirring speed also affected gold leaching in different ways. The leaching studies revealed that it is very simple to apply the cyanide leaching to the tailings and a gold recovery value of 87.5% could easily be reached. Commercially, this study reported an economically feasible process for gold recovery from an artisanal small-scale gold mining tailings in Arbaat.

Keywords: Agitation leaching. Artisanal small-scale gold mining. Cyanidation. Gold tailings.

Introduction

Artisanal small-scale mining of gold (Au) is conducted by using traditional or random methods, such as gravity. One of these traditional methods is amalgamation (Hilson, 2009). Amalgamation is a physicochemical process obtained by contacting the gold particles with mercury, because mercury has an excellent affinity for gold particles (Donkor et al., 2006). Artisanal small-scale mining accounts for 15-20% of global gold production each year (Velásquez-López et al., 2011). It directly contributes more than 20 billion U.S. dollars to the global economy, while indirectly contributing around 20 billion U.S. dollars (Persaud and Telmer, 2015). As it is known, the performance of this method does not achieve acceptable industrial recovery, which means that a residual amount of gold still exists in the tailings of this process (Esdaile and Chalker, 2018). Sudan is one of the countries located in Sub-Saharan Africa (Ahmed, 1998). Geologically, in Sudan, gold can be found in oxide minerals such as quartz, carbonates and silicate minerals. On the other hand, the sulfide minerals in the region are pyrite, arsenopyrite, chalcocite and chalcopyrite (Fadlallah et al., 2020).

In general, artisanal small-scale mining of gold mining in Sudan does not have extensive scientific literature (West et al., 2015). Artisanal mining of small-scale gold mining has been practiced in Sudan since the third century BC in the Merowe and Nubian kingdoms. The Bijah and some Arab immigrants have engaged in gold mining operations in the eastern Sudanese Red Sea Mountains (Ahmed et al., 2019). Northern Sudan, the Red Sea Hills, and the upper Blue Nile regions have a long mining history dating back to Pharaonic times (Hussien and Mohamed, 2020).

Historically, mercury was used in the amalgamation process to separate the coarse-librated gold particles (Moreno-Brush et al., 2020). Port Sudan has a huge reserve of gold ores, categorized as oxide, sulfide, and carbonate minerals (Bakr, 2018). Amalgamation is a physicochemical process that can be obtained in the desired medium of gold ore, as seen in Equation-1.

$$Au + 2Hg \rightarrow AuHg_2 \tag{1}$$

Finally, an Au_3Hg solid will develop when the resultant solid substance, mercury, volatilizes into an elemental form when

* Corresponding author: saydogan@ktun.edu.tr https://orcid.org/0000-0001-6382-1488
** e178127001003@ktun.edu.tr https://orcid.org/0009-0006-2909-3054

heated, while the gold exists as sponge gold (Callister, 2007). Gold mining production depends on the price of gold, but deposits containing 1 g/ton of gold are considered economically viable (Kiriş, 1994). According to the data for March 2019, there were approximately 900000 tons of pulp accumulation in the Arbaat region. As a result of the chemical analyses made in the pulp, it was determined that there was an average of 3 g/ton of Au.

These enterprises carry out processes, including the process of extracting gold from the mine, transportation, size reduction operations, etc. Considering the expensive processes and the importance of these residues, which contain an average of 3 g/ton Au and are ready for cyanidation processes, small enterprises in the aforementioned region operate continuously throughout the day (24 hours) (Ibrahim, 2015). The amount of amalgamation residue accumulated in the tailing area is increasing day by day. Thus, 900000 tons are equivalent to 2.7 tons of gold, and the current (in 2023) economic value is calculated as approximately 165000000 U.S. dollars.
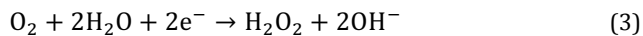
Since its advent at the end of the nineteenth century, cyanide processing has facilitated the intensification and global expansion of industrial gold mining (Marsden and House, 2006). There are significant signs that the artisanal and small-scale gold mining industries are about to experience a similar cyanide revolution. While mercury-based processing is primarily connected to artisanal small-scale gold mining, the cyanidation process is rapidly replacing mercury amalgamation (Verbrugge et al., 2021).

The cyanidation process, which chemically dissolves in cyanide, is defined by the 'Elsner Equation', as shown in Equation 7 (Ferdana et al., 2018). The metallic gold does not oxidize in the air, but the dissolved oxygen is more important in the process of cyanidation in an alkaline solution (Marsden and House, 2006). The dissolution of gold is an oxidation-reduction process that forms strong complexes in the presence of CN^- ions and dissolved oxygen. On the gold surface, gold is oxidized while dissolved oxygen is reduced, and then oxidized gold complexes with CN^- ions.
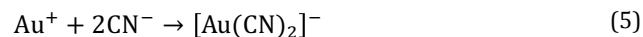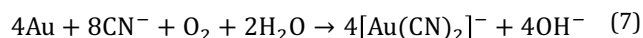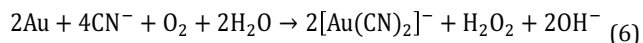
oxidation of gold:

$$Au \rightarrow Au^+ + e^- \tag{2}$$

reduction of oxygen:

$$O_2 + 2H_2O + 2e^- \rightarrow H_2O_2 + 2OH^- \tag{3}$$

$$O_2 + 2H_2O + 4e^- \rightarrow 4OH^- \tag{4}$$

complex formation:

$$Au^+ + 2CN^- \rightarrow [Au(CN)_2]^- \tag{5}$$

overall reactions:

$$2Au + 4CN^- + O_2 + 2H_2O \rightarrow 2[Au(CN)_2]^- + H_2O_2 + 2OH^- \tag{6}$$

$$4Au + 8CN^- + O_2 + 2H_2O \rightarrow 4[Au(CN)_2]^- + 4OH^- \tag{7}$$
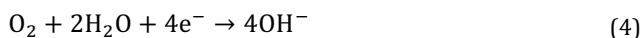
Extensive work on gold extraction from ores has been carried out, but there is a limited literature review on artisanal small-scale mining. For this reason, we used tailings.

A study was conducted on tailings from an artisanal gold mine located in northern Brazil. According to leaching experiments, the tailings are resilient to mild organic acids but soluble in alkaline and aqueous cyanide solutions. These solutions recovered 89%

of the gold and removed 100% of the mercury in 24 hours. Electro-leaching tests using sodium chloride as an electrolyte showed that mercury was removed and a gold recovery rate of up to 70% in 4 hours (de Andrade Lima et al., 2008).

A study was conducted on the stated perspectives on tailings trade between large-scale and small-scale gold mining in Ghana. During this study, field visits were made to 13 ASGM sites where improper handling of gold tailings was carried out. Interviews were conducted with the stakeholders, and the results indicated that the waste was reprocessed using cyanide (Bansah et al., 2017).

Investigated socio-technical innovation and changing production relations in artisanal small-scale mining of gold in Burkina Faso, specifically focusing on gold processing, and switched from mercury amalgamation to cyanidation for processing. The outcome was an increase in output in Burkina Faso's artisanal small-scale gold mining industry (Lanzano and di Balme, 2021). Industrially, the demand for gold is increasing day by day, in contrast to the source of gold, which is decreasing. Thus, this paper focuses on the recovery conditions for extracting gold from the Au tailings of artisanal small-scale mining using the cyanidation method.

1. Materials and methods

1.1. Materials

Approximately 50 kg of tailing sample was collected from the residual stocks of the enterprises located about 60 km north of the city of Port Sudan, where private artisanal and small-scale mining is very widespread in that region. The provided sample was reduced according to the sampling rules at the Mining Engineering Mineral Processing Laboratory of the Faculty of Engineering and Natural Sciences of Konya Technical University and reserved for the experiments planned to produce approximately 25 kg of sample. A representative sample of about 5 kg was analyzed by X-ray fluorescence spectroscopy (XRF) and X-ray diffraction (XRD, X-ray wavelength: 1.54056 Å – Cu Kα1) to determine the chemical and mineralogical compositions of the samples.

1.2. Methods

The experimental works were carried out in a one-liter beaker which placed in a temperature-controlled water bath placed on a speed-controlled mechanical stirrer having a Teflon-coated mixer as seen in Figure 1. The effects of temperature (25-85 °C), stirring speed (0-600 rpm), pH (10.0-12.30), percent solids (20-50%) and NaCN concentration (0.05-1.0 g/L) were investigated. The pulp was prepared by setting the desired test conditions and then leached for 120 minutes. The atomic absorption spectrometer (AAS-GBC Sens AA model) was used for gold analysis.
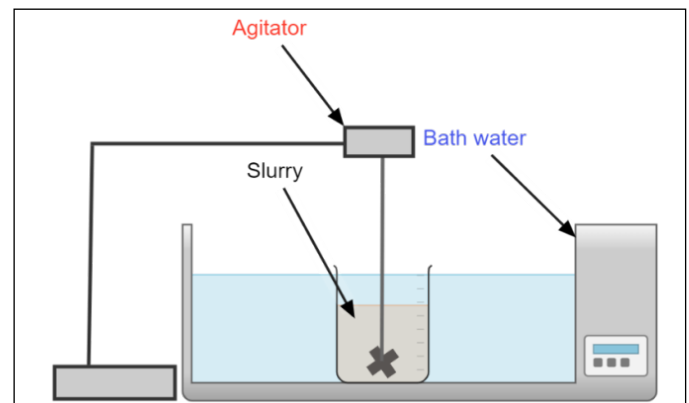

Figure 1. Experimental set-up

2. Results and Discussion

2.1. Sample characterization

Table 1 showed that the contents of the sample are mostly silicate minerals, with a mass percentage of 77.10%. Furthermore, XRD analysis also confirmed the same results with the mineral phase of SiO_2, as shown in Figure 2.

Table 1. Chemical composition of the tailings sample

Component	Amount (%)
SiO_2	77.10
Al_2O_3	8.08
Fe_2O_3	5.76
CaO	1.67
Na_2O	1.10
K_2O	0.97
SO_3	0.392
TiO_2	0.345
As_2O_3	0.054
MnO	0.049
ZrO_2	0.005
Loss on ignition	4.366
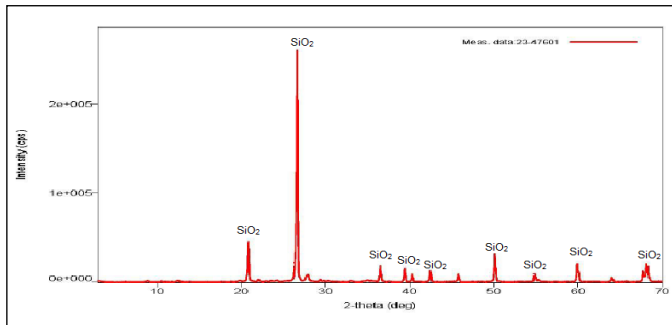
Figure 2. XRD pattern of the tailings sample

In microscopic studies, as seen in Figure 3, the results demonstrate that the sample contains free gold, silicates, copper oxides, and magnetite minerals. The magnetite mineral was detected by a low-intensity magnetic pole. However, due to the low concentration of copper and the limited detection of XRF, copper oxides were not determined in XRF analysis.

The sieve analyses (Figure 4) were performed to determine the gold concentration in each particle size fraction (Table 2). The calculated gold concentration is about 16.86 g/ton.

Table 2. The gold concentration in particle size fractions of the tailings sample

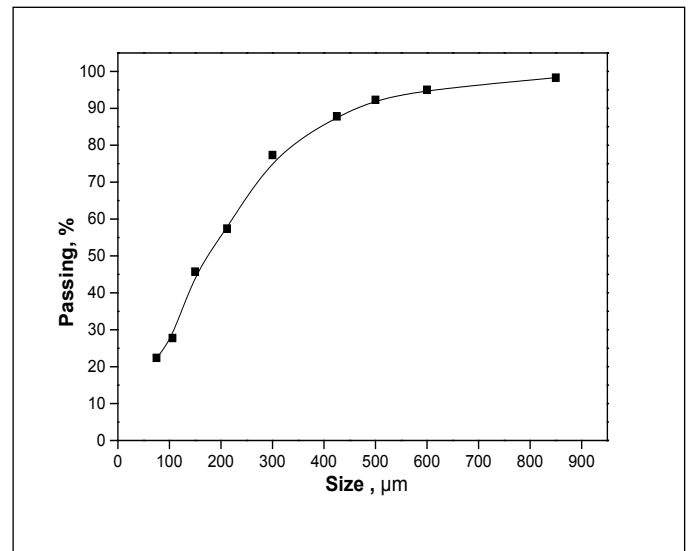| Size fraction (µm)	Au content (g/ton)
-1 mm +850	19.4
-850 +600	15.68
-600 +500	15.08
-500 +425	16.16
-425 +300	14.4
-300 + 212	11.32
-212 + 150	12.08
-150 + 106	13.56
-106 + 75	9.64
-75	30.16

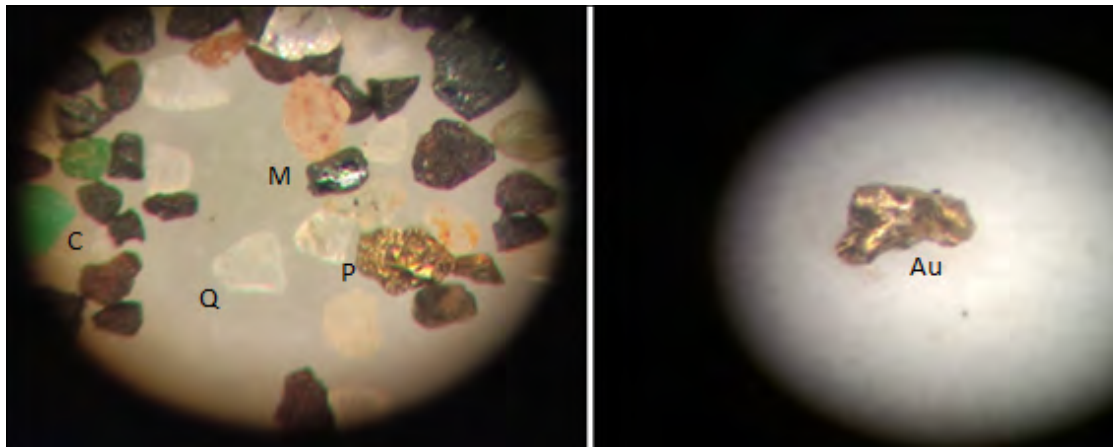*Figure 4. Sieve analysis of the tailings sample*

Figure 3. Mineral microscope view (60x) (C:copper oxide, Q:quartz, M:magnetite, P:pyrite, Au:gold)

2.2. Effect of stirring speed on Au dissolution

The effect of stirring speed at 0, 100, 200, 400 and 600 rpm were studied on solutions containing 0.5 g/L NaCN. The solid/liquid ratio was 40%, the temperature was 25 °C and the pH, adjusted by Ca(OH)$_2$, was 10.30. The results of the experiments investigating the effects of stirring speed were given in Figure 5. As seen in Figure 5, when the stirring speed increases, the Au dissolution rate also increases. For example, as a result of a 15-minute leaching process, the Au dissolution efficiency values obtained at 0-600 rpm stirring speeds are 52.2%, 61.7%, 62.3%, 63.6% and 64.0%, respectively. Very similar values were obtained in gold dissolution efficiencies at 400 rpm and 600 rpm stirring speeds. In other words, no significant gold dissolution efficiency was observed at values above 400 rpm stirring speed.

Dissolution of gold in cyanidation processes is normally a lengthy process. However, approximately 84% of the gold can be dissolved after 120 minutes at a stirring speed of 100 rpm. It is known that mercury greatly enhances the rate of gold dissolution. However, the XRF analysis performed on the sample revealed no presence of mercury. Due to the small grain size of gold, there is a large surface area in contact with the solution, which explains the high dissolution rate (Marsden and House, 2006). The stirring speed was adjusted to 400 rpm to investigate other parameters, as there was no noticeable difference in the extraction of gold between 400 and 600 rpm.
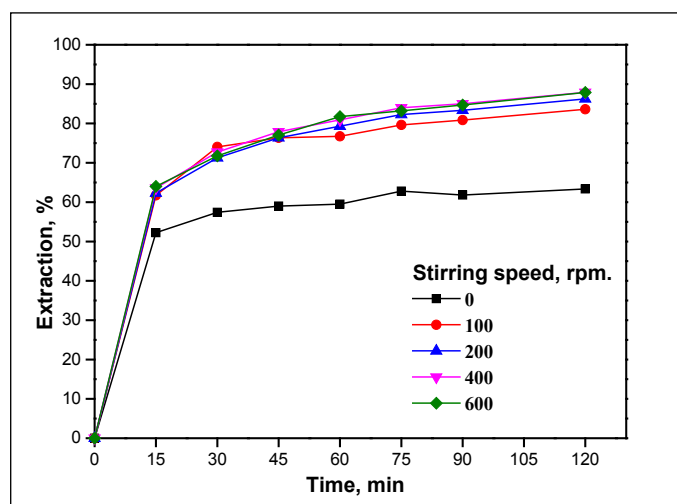

Figure 5. Effect of stirring speed on gold recovery

2.3. Effect of pH on Au dissolution

Experiments investigated the pH in the range of 10 to 12.30 in a solution containing 0.5 g/L NaCN, 400 rpm, 25 °C, and a solid/liquid ratio of 40%. Gold ore cyanidation is known to be affected by pH (Brittan, 2008). The results are given in Figure 6. As shown in Figure 6, as the pH increases in the pH range of 10-10.10, the Au dissolution rate also increases. In the results of the leaching process at pH 10.10 and pH 10.30, the Au dissolution rate is almost the same, but after pH 10.30, the Au dissolution rate decreases. The reason why the dissolution rate decreases rapidly at pH values greater than 10.30 is because Ca(OH)$_2$ is used as a pH adjuster. The H$_2$O$_2$ formed as a reaction product (Equation 6) reacts with Ca^{2+} ions on the gold surface and forms CaO$_2$ (calcium superoxide) (Habashi, 1999). To investigate other parameters, the pH value was chosen as 10.30.
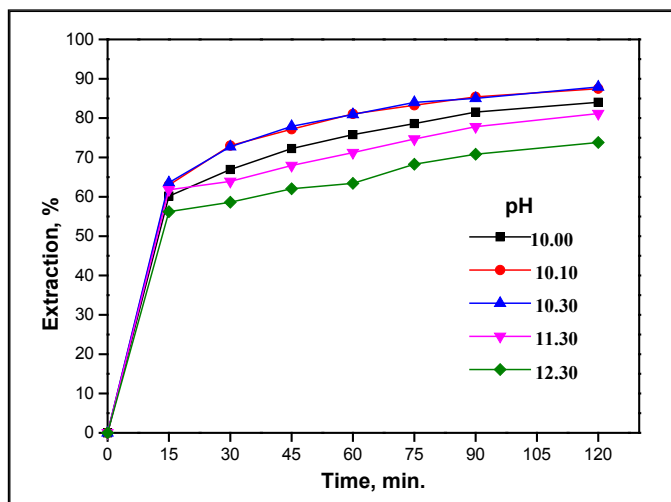

Figure 6. Effect of pH on gold recovery

1.4. Effect of NaCN concentration on Au dissolution

The effect of sodium cyanide concentrations on the dissolution of Au in the cyanidation process depends on cyanide and oxygen concentrations, leading to the opinion that solubility will increase with an increase in both (Equation 6 and Equation 7) (Lorenzen and Tumilty,1992). The effect of NaCN concentration on Au dissolution was investigated. The sodium cyanide concentration was between 0.05 and 1.0 g/L NaCN, the solid/liquid ratio was 40% at a temperature of 25 °C, the pH was 10.30, and the stirring speed was 400 rpm. The results are given in Figure 7. As shown in Figure 7, the gold extraction increased with increasing NaCN concentration. For example, as a result of a 15-minute leaching process, the Au dissolution efficiency values obtained in the 0.05-1.0 g/L NaCN concentration range are 14.5%, 53.4%, 54.5%, 63.6%, 65.8% and 71.9%, respectively. As a result of the 120-minute leaching process, the Au dissolution efficiency remained around 88% in the 0.25-1.0 g/L NaCN concentration range. It has been concluded that the dissolution rate of coarse-grained gold remains slow due to the nature of cyanidation processes, while fine-grained gold in the studied sample dissolves rapidly (Corrans and Angove, 1991).

Detailed studies have shown that the rate of gold dissolution increases linearly with increasing sodium cyanide concentration until a maximum is reached, beyond which further increase in sodium cyanide has no effect. At the end of 120 minutes, there was no significant change between the concentrations in the range of 0.5-1.0 g/L NaCN, so a concentration of 0.5 g/L NaCN was chosen for other experiments.
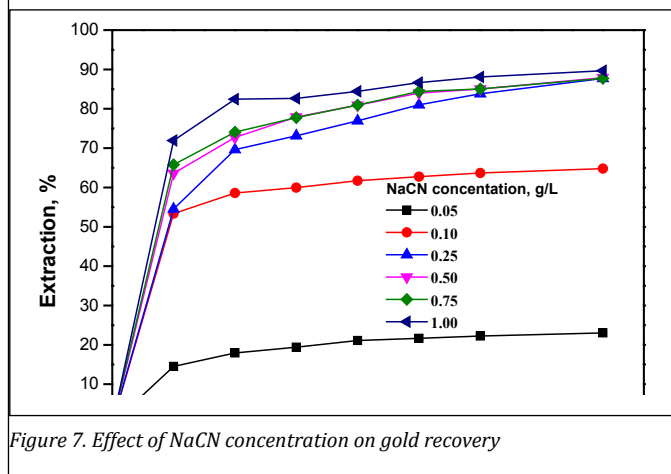

Figure 7. Effect of NaCN concentration on gold recovery

1.5. Effect of solid/liquid ratio on Au dissolution

The effect of solid/liquid (S/L) ratio experiments was conducted between 20 and 50%, stirring speed of 400 rpm, NaCN concentration of 0.5 g/L, temperature of 25 °C and pH of 10.30. The results are presented in Figure 8. As shown in Figure 8, the gold extraction decreased with an increasing solid/liquid ratio. When the S/L ratio percentage was 20%, the value of Au dissolution efficiency was 98%. As the S/L ratio increases, the amount of CN^- ions required per unit weight decreases. Similarly, the amount of oxygen dissolved in the solution reduces the oxygen required per unit weight. Normally, leaching processes experience a decrease in the S/L ratio, leading to an increase in dissolution efficiency, but this does not hold in industrial conditions. A higher S/L ratio increases the amount of ore processed per unit of time, thereby increasing the capacity. In other words, doubling the S/L ratio under suitable conditions leads to an increase in facility capacity at the same rate, increasing the amount of ore processed per unit of time. This, in turn, reduces initial investment expenses and other expenses (employee expenses, energy expenses, etc.) (Ahtiainen and Lundström, 2019). So, the S/L ratio of 40% was selected for the study of other parameters.
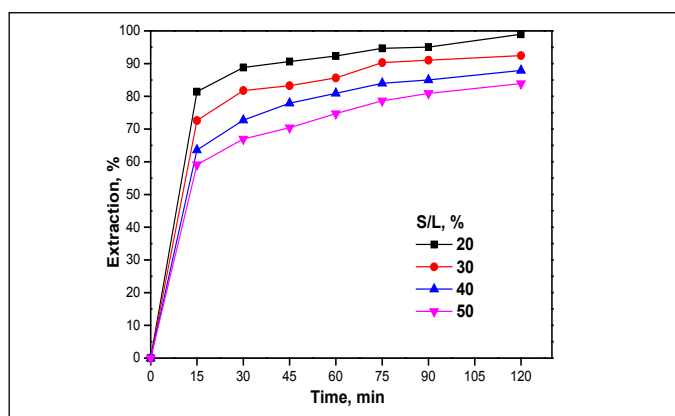

Figure 8. Effect of solid/liquid ratio on gold recovery

1.6. Effect of temperature on Au dissolution

The effect of temperature was investigated in the range of 25-85 °C in a solution containing 0.5 g/L NaCN, 400 rpm, pH 10.30 and an S/L ratio of 40%. The results are given in Figure 9. As seen in Figure 9, as the temperature increases, the Au dissolution rate also increases. For example, as a result of a 45-minute leaching process, the Au dissolution efficiency was 77.9% at 25 °C and 98.7% at 85 °C. At the end of 60 minutes at a temperature of 85 °C, the gold extraction was 100%. In the literature, when the temperature increases, the extraction rate of gold increases until 85 °C; after that, the extraction rate of gold decreases because dissolved oxygen decreases in the solution (Habashi, 1999; Ahtiainen and Lundström, 2019).
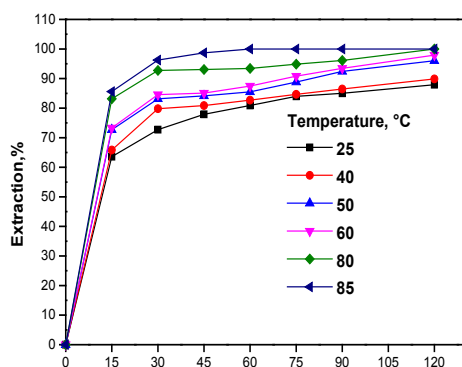

Figure 9. Effect of temperature on gold recovery

3. Conclusions

The XRF and XRD analyses revealed that the tailings sample used in the leaching studies had an oxide composition and formed from mainly silicate minerals. The tailings sample had average gold grade of 16.86 g/ton, which is good for agitation cyanide tank leaching. The maximum recovery of gold (87.5%) was obtained at a stirring speed of 400 rpm, a temperature of 25 °C, a solid percentage of 40%, a pH value of 10.30 and a sodium cyanide concentration of 0.5 g/L. The metallurgical tests showed that artisanal small-scale gold mining tailings from Arbaat region are amenable to cyanide leaching in an agitated tank.

References

Ahmed, A., Purwanto R. and Sunoko, H.R. 2019. Consequences of mercury used by artisanal small-scale gold mining processes A case of River Nile State Sudan. Journal of Ecological Engineering, 20(2): 106-115. https://doi.org/10.12911/22998993/96275.

Ahmed, A.A.M. 1998. Sudan industrial minerals & rocks: Centre for Strategic Studies.

Ahtiainen, R. and Lundström, M. 2019. Cyanide-free gold leaching in exceptionally mild chloride solutions. Journal of Cleaner Production, 234: 9-17. https://doi.org/10.1016/j.jclepro.2019.06.197

Bakr, A. 2018. Smart artisanal gold mining from a Sudanese perspective. Biomedical Journal of Scientific & Technical Research 8(5): 8-14. https://doi.org/10.26717/BJSTR.2018.08.001704

Bansah, K., Dumakor-Dupey, N. and Sakyi-Addo, G. 2017. Digging for survival: female participation in artisanal and small-scale mining in the Tarkwa mining district of Ghana. Paper presented at the SME Annual Meeting - Feb.

Brittan, M.I. 2008. Kinetic and equilibrium effects in gold ore cyanidation. Mining, Metallurgy & Exploration, 25(3): 117-122. https://doi.org/10.1007/BF03403396

Callister Jr, W.D. 2007. Materials science and engineering An introduction.

Corrans, I.J. and Angove, J.E. 1991. Ultra fine milling for the recovery of refractory gold. Minerals Engineering, 4(7): 763-776. https://doi.org/10.1016/0892-6875(91)90064-3

de Andrade Lima, L.R.P., Bernardez, L.A. and Barbosa, L.A.D. 2008. Characterization and treatment of artisanal gold min tailings. Journal of Hazardous Materials, 150(3): 747-753. https://doi.org/10.1016/j.jhazmat.2007.05.028

Donkor, A.K., Nartey, V., Bonzongo, J. and Adotey, D. 2006. Artisanal mining of gold with mercury in Ghana. West African Journal of Applied Ecology, 9(1):1-8. https://doi.org/10.4314/wajae.v9i1.45666

Esdaile, L.J. and Chalker, J.M. 2018. The mercury problem in artisanal and small-scale gold mining. Chemistry–A European Journal, 24(27): 6905-6916. https://doi.org/10.1002/chem.201704840

Fadlallah, M.A., Pal, I. and Hoe, V. C. 2020. Determinants of perceived risk among artisanal gold miners: A case studyof Berber locality, Sudan. The Extractive Industries and Society, 7(2): 748-757. https://doi.org/10.1016/j.exis.2020.03.006

Ferdana, A. D., Petrus, H.T.B.M., Bendiyasa, I., Prijambada, I.D., Hamada, F. and Sachiko, T. 2018. Optimization of gold ore Sumbawa separation using gravity method: Shaking table. AIP Conf. Proc., 1945: 020070. https://doi.org/10.1063/1.5030292

Habashi, F. 1999. A Textbook of Hydrometallurgy. 2nd ed. p. 210.

Hilson, G. 2009. Small-scale mining, poverty and economic development in sub-Saharan Africa: An overview. Resources Policy, 34(1-2): 1-5. https://doi.org/10.1016/j.resourpol.2008.12.001

Hussien, H.H. and Mohamed, E.E. 2020. Impacts of artisanal gold mining in River Nile State, Sudan. International Journal of Advanced and Applied Sciences, 7(9): 8-14. https://doi.org/10.21833/ijaas.2020.09.002

Ibrahim, M.S. 2015. Artisanal mining in Sudan: Opportunities, challenges, and impacts. UNCTAD, 17th Africa OILGASMINE: Extractive Industries and Sustainable Job Creation.

Kiriş, K. 1994 Gold; Economic deposit types, exploration phases and cost. Chamber of Geological Engineers Publications, pp. 44-45.

Lanzano, C. and Arnaldi di Balme, L. 2021. Who owns the mud? Valuable leftovers, sociotechnical innovation and changing relations of production in artisanal gold mining (Burkina Faso). Journal of Agrarian Change, 21(3): 433-458. https://doi.org/10.1111/joac.12412

Lorenzen, L. and Tumilty, J.A. 1992. Diagnostic leaching as an analytical tool for evaluating the effect of reagents on the performance of a gold plant. Minerals Engineering, 5(3): 503-512. https://doi.org/10.1016/0892-6875(92)90229-3

Marsden, J. and House, I. 2006. The Chemistry of Gold Extraction. 2nd Ed. Society for Mining, Metallurgy, and Exploration, Inc. (SME).

Moreno-Brush, M., McLagan, D.S. and Biester, H. 2020. Fate of mercury from artisanal and small-scale gold mining in tropical rivers: Hydrological and biogeochemical controls. A critical review. Critical Reviews in Environmental Science and Technology, 50(5): 437-475. https://doi.org/10.1080/10643389.2019.1629793

Persaud, A. and Telmer, K. 2015. Developing Baseline Estimates of Mercury Use in Artisanal and Small-Scale Gold Mining Communities: A Practical Guide (Version 1.0). Victoria, BC.

Velásquez-López, P.C., Veiga, M.M., Klein, B., Shandro, J.A. and Hall, K. 2011. Cyanidation of mercury-rich tailings in artisanal and small-scale gold mining: identifying strategies to manage environmental risks in Southern Ecuador. Journal of Cleaner Production, 19(9): 1125-1133. https://doi.org/10.1016/j.jclepro.2010.09.008

Verbrugge, B., Lanzano, C. and Libassi, M. 2021. The cyanide revolution: Efficiency gains and exclusion in artisanal- and small-scale gold mining. Geoforum, 126: 267-276. https://doi.org/10.2138/am.2008.502

West, D.C., Ford, J.B. and Ibrahim, E. 2015. Strategic marketing: Creating competitive advantage, Oxford University Press, USA.